2012

Electronic And Optoelectronic Transport Properties Of Carbon Nanotube/organic Semiconductor Devices

Biddut Sarker
University of Central Florida

ELECTRONIC AND OPTOELECTRONIC TRANSPORT PROPERTIES OF CARBON NANOTUBE/ORGANIC SEMICONDUCTOR DEVICES

by

BIDDUT K. SARKER
M.S. University of Central Florida, 2010
M.S. University of Dhaka, 2005
B.S. University of Dhaka, 2003

A dissertation submitted in partial fulfillment of the requirements
for the degree of Doctor of Philosophy
in the Department of Physics
in the College of Sciences
at the University of Central Florida
Orlando, Florida

Fall Term
2012

Major Professor: Saiful I. Khondaker

ABSTRACT

Organic field effect transistors (OFETs) are of significant research interest due to their promising applications in large area, low-cost electronic devices such as flexible displays, sensor arrays, and radio-frequency identification tags. A major bottleneck in fabricating high-performance OFET is the large interfacial barrier between the metal electrodes and organic semiconductors (OSC) which results in an inefficient charge injection. Carbon nanotubes (CNTs) are considered to be a promising electrode material which can address this challenge.

In this dissertation, we demonstrate fabrication of high-performance OFETs using aligned array CNT electrodes and investigate the detailed electronic transport properties of the fabricated devices. The OFETs with CNT electrodes show a remarkable enhancement in the device performance such as high mobility, high current on-off ratio, higher cutoff frequency, absence of short channel effect and better charge carrier injection than those OFETs with metal electrodes. From the low temperature transport measurements, we show that the charge injection barrier at CNT/OSC interface is smaller than that of the metal/OSC interface. A transition from direct tunneling to Fowler-Nordheim tunneling observed in CNT/OSC system shows further evidence of low injection barrier. A lower activation energy measured for the OFETs with CNT electrodes gives evidence of lower interfacial trap states. Finally, OFETs are demonstrated by directly growing crystalline organic nanowires on aligned array CNT electrodes.

In addition to investigating the interfacial barrier at CNT/OSC interface, we also studied photoconduction mechanism of the CNT and CNT/OSC nanocomposite thin film devices. We found that the photoconduction is due to the exciton dissociations and charge carrier separation caused by a Schottky barrier at the metallic electrode/CNT interface and diffusion of the charge

carrier through percolating CNT networks. In addition, it is found that photoresponse of the CNT/organic semiconductor can be tuned by changing the weight percentage of CNT into the organic semiconductors.

To my parents

ACKNOWLEDGMENTS

First and foremost I would like to express my sincere appreciation to my research advisor Professor Saiful Khondaker for guidance, infinite patience and understanding throughout on the journey of this dissertation. Saiful guided me not only academically through various research struggles but also emotionally through the rough road to finish this thesis with his supporting spirit and vast knowledge.

I would also like to thank Professor Alfons Schulte, Professor Sergey Stolbov, and Professor Andre J. Gesquiere for serving on my qualifying exam and dissertation committee. I appreciate the insightful questions, comments and suggestions they made during the exam, and also during their edition of my PhD thesis. I am also thankful Professor Lei Zhai for numerous discussions on organic semiconductor materials and being a second mentor to me.

I am thankful to all of my previous and current members of Khondaker group for making me PhD research productive and enjoyable. I would like to thank Arif and Paul who helped me very much to ramp up in my early days in this group. It was a pleasure advising Edwards, undergraduate student; Robert, REU student; Munehisa, visiting student, and Narae, graduate student in this group. I thank Daeha, Feras, Rakib, Narae, Udai, Shashank, Surajit, Tanusri, Jianhua, Kristy, Eliot, and Edwards for their support, help and fruitful scientific discussion. I am also thankful to the U.S. National Science Foundation (Grant Number ECCS 1102228) for partial financial support.

Finally, my special thanks to my family and friends for all their love and encouragement. My lovely wife, Shweta, was always encouraging me during this dissertation work. Her unconditional love as well as care was vital in keeping me active every day. I also thank my parents for their support and love.

TABLE OF CONTENTS

LIST OF FIGURES

LIST OF TABLES

LIST OF ACRONYMS/ABBREVIATIONS

AFM	Atomic Force Microscopy
CNT	Carbon Nanotube
CVD	Chemical Vapor Deposition
DEP	Dielectrophoretic
EBL	Electron-Beam Lithography
FET	Field Effect Transistor
FN	Fowler-Nordheim
HOMO	Highest Occupied Molecular Orbital
LUMO	Lowest Unoccupied Molecular Orbital
MWNT	Multi Walled Carbon Nanotube
NIR	Near Infrared
P3HT	Poly(3-hexylthiophene)
OSC	Organic Semiconductor
OFET	Organic Field Fffect Transistor
PMMA	Poly(methylmethacrylate)
SEM	Scanning Electron Microscope
SWNT	Single Walled Carbon Nanotube
RS	Richardson Schottky
TEM	Transmission Electron Microscopy

CHAPTER 1: INTRODUCTION

1.1 General Background and Motivation

Organic electronic devices, also known as plastic electronic devices, have attracted tremendous attention in the recent years due to their advantages, including transparency, flexibility, light-weight, low cost and solution processability (Figure 1.1) [1-8]. Research interest in the organic electronics has steadily increased in the last two decades. It is clearly seen in the Figure 1.2 that the number of publication in the area of organic electronics is increased exponentially with time. Organic field effect transistors (OFETs) are considered as one of the promising active elements in the organic electronic devices such as flexible displays, sensor arrays, and radiofrequency identification tags [1-5]. In order to fabricate high-performance organic electronics devices, OFETs should have high mobility, high current on-off ratio, high on-current and high switching speed.

Figure 1.1: Application of organic electronic devices. Adapted from reference [1, 9-11]

In the recent years, remarkable attempts have been made in fabricating high-performance OFETs using various organic semiconductors (OSCs) and optimizing the processing parameters. The performance of the OFETs not only depends on the molecular properties of the organic semiconductors but also it strongly depends on the nature of the interfaces that forms between metal electrodes and organic semiconductors [12-18]. The electrode/OSC interface limits the carrier charge injection from the metal electrode to the organic semiconductors, which is one of the major bottlenecks in fabricating high-performance OFET [12-14].

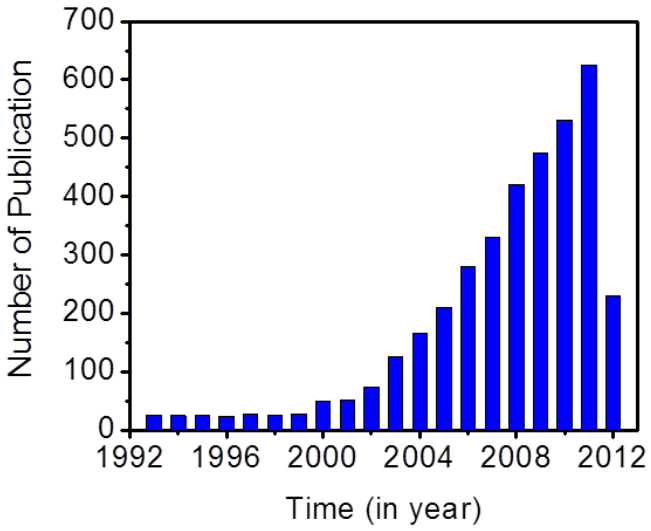

Figure 1.2: Number of publications on organic electronics in last ~ 20 years. Source: ISI Web of Science.

Currently, metals like gold, palladium are widely used as source and drain electrodes in the OFETs. When a layer of organic semiconductors is contacted by the metal electrodes, various charge injection barriers such as Schottky barrier, dipole barrier are formed at the metal/OSC interface [12-16]. Due to these barriers, the contact resistances at metal/OSC interface become very large which limits the charge injection from the metal electrode to organic semiconductors and limits the performance of the OFETs [12-20]. Therefore, fabrication of high-performance

FET using metal electrodes still remains a major challenge [18-20]. In addition, since metal electrodes are not flexible, it is another hurdle to utilize the metal electrodes in flexible electronic devices. To realize the overall goal of organic electronics, recently researchers are looking for alternative electrode materials for the OFETs with high charge carrier injection capability, excellent interfacial compatibility with the organic semiconductors and suitability for use in flexible organic electronics.

One of the most promising materials to replace the metal electrodes in high-performance OFETs is carbon nanotube (CNT). The carbon nanotubes are the sheets of the carbon atom rolled into one or more concentric hollow cylinders. The diameter of individual single-walled carbon nanotube is in the range of 1-3 nm and length up to few cm [21, 22]. The work function of carbon nanotube is in the range of 4.7-5.2 eV [21], which is well-aligned with the highest occupied molecular orbital (HOMO) level of many organic semiconductors such as pentacene, poly (3-hexylthiophene) (P3HT). Since both the carbon nanotubes and the organic semiconductors mainly consist of carbon, a better interfacial contact at the CNT/OSC interface is expected due to a strong π-π interaction between them [23]. In addition, the current carrying capacity of the carbon nanotubes (10 $\mu A/nm^2$) is significantly higher than the current carrying capacities of the noble metal (10 nA/nm^2) [24]. The CNT thin films are also flexible, transparent in the visible range and solution processible [21, 22, 25].

Due to their high conductivity, high work-function and π-π interaction with organic semiconductors, the CNTs are considered as potential electrode material in many optoelectronic devices including solar cells, flexible light emitting diode, and OFETs [25-33]. Fabrication of OFETs has been demonstrated using individual CNT electrodes [27, 28], CNT random network electrode [29-31], and CNT/polymer composite electrodes [32, 33]. The OFET devices with

CNT electrodes have shown improved performance than that of the devices with metal electrodes. It is speculated that improved device performance with CNT electrodes may due to the improved injection of charge carriers from CNT to organic semiconductors owing to strong π-π bonding between the CNTs and organic semiconductors.

Although previous studies have showed the improved performance for the devices with CNT electrodes than that of their control devices fabricated with metal electrodes, fabrication of high-performance OFETs with CNT electrodes is still remained a significant challenge. In addition, the nature of the CNT/OSC interface in not well understood. In particular, charge injection and transport mechanisms in the device with CNT electrode are still unexplored. Therefore, fabricating the high-performance OFETs with CNT electrodes, understanding the charge injection and transport mechanism, and determining the charge in injection barriers at the CNT/OSC interface are of great importance for achieving the overreaching goal of the CNT electrodes in organic electronics.

1.2 Thesis Statement and Organization

In this dissertation, we demonstrate fabrication of high-performance OFETs using aligned array CNT electrodes and investigate the detailed electronic transport properties of the fabricated devices. The OFETs with CNT electrodes show a remarkable enhancement in the device performance such as high mobility, high current on-off ratio, higher cutoff frequency, absence of short channel effect and better charge carrier injection than those OFETs with metal electrodes. From the low temperature transport measurements, we show that the charge injection barrier at CNT/OSC interface is smaller than that of the metal/OSC interface. A transition from direct tunneling to Fowler-Nordheim tunneling measured in CNT/OSC system shows further

evidence of low injection barrier. In addition, a lower activation energy observed in the OFETs with CNT electrodes gives evidence of lower interfacial trap states. Finally, OFETs are demonstrated by directly growing crystalline organic nanowires on aligned array CNT electrodes.

In addition to investigating the interfacial barrier at CNT/OSC interface, we also studied photoconduction mechanism of the CNT and CNT/OSC nanocomposite thin film devices. We found that the photoconduction is due to the exciton dissociations and charge carrier separation caused by a Schottky barrier at the metallic electrode/CNT interface and diffusion of the charge carrier through percolating CNT networks. In addition, it is found that photoresponse of the CNT/organic semiconductor can be tuned by changing the weight percentage of CNT into the organic semiconductors.

The organization of this thesis as follows: A background review on organic semiconductors, organic field effect transistors, physics of charge injection in the OFETs, and summary of the previous work CNT electrodes for OFETs are presented in chapter 2.

Chapter 3 describes details of the design, fabrication and characterization of the organic electronic devices using various micro and nanofabrication tools. This chapter includes a description of assembly for aligned array CNTs via dielectrophoretic, fabrication of aligned array CNTs electrodes using electron beam lithography (EBL) and plasma etch; fabrication of metal electrodes using photolithography followed by EBL and thermal deposition; fabrication of the OFETs based on various organic semiconductors, and measurement setups of the devices at room and low temperatures.

In chapter 4, we investigate room temperature electronic transport properties of the OFETs with CNT aligned array electrodes. A series of OFETs based various organic

semiconductors (such as pentacene, P3HT) with aligned array CNT electrodes as well as metal electrodes are fabricated. All the OFETs with CNT electrodes show improved device performance, such as higher mobility, higher current on-off ratio, and higher cut-off frequency, than that of the OFETs with metal electrodes.

After discussing the room temperature device properties, in chapter 5 we investigate the physics of charge injection and transport in the OFETs with aligned array CNT electrodes using temperature dependent electronic transport measurement. We show that in the high temperature range (300-200 K), the charge injection mechanism is dominated by thermal emission which is well explained by Richardson Schottky model. The charge injection barrier at CNT/OSC interface is lower than that of at metal/ OSC interface. In addition, the barrier height at the CNT/OSC interfaces can be tuned by the gate-voltage. At low temperature the current-voltage characteristics show a transition from direct tunneling to Fowler-Nordheim tunneling, which shows a further evidence of a lower injection barrier at CNT/OSC interface. From the study of the transport mechanism, we show that that the charge transport is improved in the devices with CNT electrode, and interfacial traps state at the CNT/organic interface is lower than that of the metal/OSC.

The chapter 6 demonstrates a bottom up approach to fabricate OFETs by growing organic crystalline nanowires on aligned array CNT interdigitated electrodes which exploit strong π-π interaction for both efficient charge injection and transport. The organic nanowire OFETs with CNT electrodes show a remarkable enhancement of the device performance such as high mobility, high current on-off ratio, absence of short channel effect and better charge carrier injection than that OFETs with gold electrodes. This is attributed to the improved contact via

strong π-π interaction CNT electrodes with the crystalline organic nanowires as well as the improved morphology of organic semiconductor due to one dimensional crystalline structure.

In Chapter 7, the thesis shifted its focus on photoconduction mechanism of the CNT and CNT/OSC nanocomposite thin film devices. We show that that the photoconduction is due to the exciton dissociations and charge carrier separation caused by a Schottky barrier at the metallic electrode/CNT interface and diffusion of the charge carrier through percolating CNT networks. In addition, we also show that that photoresponse of the CNT/organic semiconductor can be tuned by changing the weight percentage of CNT into the organic semiconductors.

Finally in chapter 8, we summarize the finding of this dissertation and propose the possible future directions related to this work.

1.3 References

1. S.R. Forrest, The Path To Ubiquitous And Low-Cost Organic Electronic Appliances On Plastic. Nature, **428** 911 (2004).

2. B. Crone, A. Dodabalapur, Y. Y. Lin, R. W. Filas, Z. Bao, A. LaDuca, R. Sarpeshkar, H. E. Katz and W. Li, Large-scale complementary integrated circuits based on organic transistors. *Nature* **403**, 521 (2000).

3. Y. Chen, J. Au, P. Kazlas, A. Ritenour, H. Gates and M. McCreary,Electronic paper: Flexible active-matrix electronic ink display. *Nature* **423**, 136 (2003).

4. J. Zaumseil, H. Sirringhaus, Electron and Ambipolar Transport in Organic Field-Effect Transistors. *Chem. Rev.* **107**, 1296 (2007).

5. C. D. Dimitrakopoulos, P. R. L. Malenfant, Organic Thin Film Transistors for Large Area Electronics. *Adv.Mater*. **14**, 99 (2002).

6. H. Klauk, Organic Thin-Film Transistors. *Chem. Soc. Rev*. **39**, 2643 (2010).

7. G. Horowitz, Organic Field-Effect Transistors. *Adv.Mater* **10**, 365 (1998).

8. D. Braga, G. Horowitz, High-Performance Organic Field-Effect Transistors. *Adv.Mater* **21**, 1473 (2009).

9. A. Virkar, Investigating the Nucleation, Growth and Energy Levels of Organic Semiconductors for High Performance Plastic Electronics, *PhD Dissertation*, (2010).

10. http://www.frontiernet.net/~print.elect/files/Organic%20Electronics%20Technology.pdf

11. A Dodabalapur, Organic and polymer transistors for electronics, Mater Today, **9**, 24, (2006)

12. H. Ishii, K. Sugiyama, E. Ito, K. Seki, Energy Level Alignment and Interfacial Electronic Structures at Organic/Metal and Organic/Organic Interfaces. *Adv.Mater* **11**, 605 (1999).

13. S. Braun, W. R. Salaneck, M. Fahlman, Energy-Level Alignment at Organic/Metal and Organic/Organic Interfaces. *Adv.Mater* **21**, 1450 (2009).

14. D. Natali, M. Caironi, Charge Injection in Solution-Processed Organic Field-Effect Transistors: Physics, Models and Characterization Methods. *Adv.Mater* **24**, 1357 (2012).

15. J. C. Scott, Metal-Organic Interface And Charge Injection In Organic Electronic Devices. J. Vac.Sci.& Tech.A: **21**, 521 (2003).

16. G. Hill, A. Rajagopal, A. Kahn, Y. Hu, Molecular Level Alignment At Organic Semiconductor-Metal Interfaces. *Appl. Phys. Lett.* **73**, 662 (1998).

17. Z. Liu, M. Kobayashi, B. C. Paul, Z. Bao, Y. Nishi, Contact Engineering For Organic Semiconductor Devices Via Fermi Level Depinning At The Metal-Organic Interface. *Phys. Rev*.B **82**, 035311 (2010).

18. M. Marinkovic, D. Belaineh, V. Wagner, D. Knipp, On the Origin of Contact Resistances of Organic Thin Film Transistors. *Adv.Mater.* **24**, 4005 (2012)

19. T. Hirose, T. Nagase, T. Kobayashi, R. Ueda, A. Otomo and H. Naito, Device Characteristics Of Short-Channel Polymer Field-Effect Transistors. *Appl. Phys. Lett*, **97**, 083301 (2010).

20. J. Z. Wang, Z. H. Zheng, H. Sirringhaus, Suppression Of Short-Channel Effects In Organic Thin-Film Transistors. *Appl. Phys. Lett*, **89**, 083513 (2006).

21. L. Hu, D. S. Hecht, G. Gruener, Carbon Nanotube Thin Films: Fabrication, Properties, and Applications. *Chem. Rev*. **110**, 5790 (2010).

22. P. Avouris, Z. Chen, V. Perebeinos, Carbon-based electronics. *Nature Nanotech*. **2**, 605 (2007).

23. J. Liu, J. Zou, L. Zhai, Bottom-up Assembly of Poly(3-hexylthiophene) on Carbon Nanotubes: 2D Building Blocks for Nanoscale Circuits. *Macromol. Rapid Com*. **30**, 1387 (2009).

24. P. G. Collins, M. S. Arnold, P. Avouris, Engineering Carbon Nanotubes and Nanotube Circuits Using Electrical Breakdown. *Science* **292**, 706 (2001).

25. D. Zhang, K. Ryu, X. Liu, E.Polykarpoy, J. Ly, M. E. Thompson, C. Chow, Transparent, Conductive, and Flexible Carbon Nanotube Films and Their Application in Organic Light-Emitting Diodes. *Nano Lett.* **6**, 1880 (2006).

26. M. W. Rowell, M. A. Topinka, M. D. McGehee, H.-J. Prall, G. Dennler, N. S. Sariciftci, L. Hu and G. Gruner, Organic Solar Cells With Carbon Nanotube Network Electrodes. *Appl. Phys. Lett.* **88**, 233506 (2006).

27. P. F. Qi, A. Javey, M. Rolandi, Q. Wang, E. Yenilmez and H. J. Dai, Miniature Organic Transistors With Carbon Nanotubes As Quasi-One-Dimensional Electrodes. *J.Am.Chem. Soc*. **126**, 11774 (2004).

28. C. M. Aguirre, C. Ternon, M. Paillet, P. Desjardins, R. Martel, Carbon Nanotubes as Injection Electrodes for Organic Thin Film Transistors. *Nano Lett*. **9**, 1457 (2009).

29. C. Chia-Hao, C. Chao-Hsin, Y. Jung-Yen, Pentacene-Based Thin-Film Transistors With Multiwalled Carbon Nanotube Source And Drain Electrodes. *Appl. Phys. Lett.* **91**, 083502 (2007).

30. Q. Cao, Z.-T. Zhu, M. G. Lemaitre, M.-G. Xia, M. Shim and J. A. Rogers. Transparent Flexible Organic Thin-Film Transistors That Use Printed Single-Walled Carbon Nanotube Electrodes. *Appl. Phys. Lett.* **88**, 113511 (2006).

31. Southard, V. Sangwan, J. Cheng, E. D. Williams, M. S. Fuhrer, Solution-Processed Single Walled Carbon Nanotube Electrodes For Organic Thin-Film Transistors. *Organic Electron*. **10**, 1556 (2009).

32. M. Lefenfeld, G. Blanchet, J. A. Rogers, High-Performance Contacts in Plastic Transistors and Logic Gates That Use Printed Electrodes of DNNSA-PANI Doped with Single-Walled Carbon Nanotubes. *Adv.Mater.* **15**, 1188 (2003).

33. S. L. Hellstrom, R. Z. Jin, R. M. Stoltenberg, Z. Bao, Driving High-Performance n- and p-type Organic Transistors with Carbon Nanotube/Conjugated Polymer Composite Electrodes Patterned Directly from Solution. *Adv.Mater.* **22**, 4204 (2010).

CHAPTER 2: BACKGROUND

2.1 Organic Field Effect Transistors (OFETs)

Since the first discovery of the organic field effect transistors (OFETs) (Figure 2.1) based on organic semiconductors in the 1980's, OFETs have attracted broad attention because they could serve as a key component in the organic electronic devices such as organic flexible display, sensor arrays, flexible smart cards, radiofrequency identification (RF-ID) tags [1-9]. One of the main components of the OFETs is organic semiconductors, which are carbon-rich compound with semiconductor properties. Although mobility of the organic semiconductors is lower than inorganic ones, organic semiconductors have a number of special advantages. One of the major advantages is that organic devices can be fabricated at low temperature (less than 200 ^{0}C) using various simple and low-cost techniques such as spin-coating, drop-casting, spray-coating, and vacuum thermal deposition. In addition, organic semiconductor devices are flexible, transparent and light-weight. Another advantage of the organic semiconductors over the inorganic one is that it can be easily tuned the properties by tailoring structure of the organic semiconductors.

Due to continuous advancement of organic semiconductor materials by tailoring their electronics properties and significant improvement in device fabrication process, the performance of the OFETs is increased with time. The field-effect mobility of the OFETs based on organic semiconductor materials is in the ranges of of 0.1–1 cm^2 /V.s [1-9]. The prototypes of the OFETs based organic electronic devices have been demonstrated such as OFET-driven liquid-crystal displays (LCD), organic light-emitting diode (OLED) displays, and organic logic

circuits [1-9]. On the scientific sides, OFETs are also use an effective and powerful tool unit to test charge transport in high band-gap and low-conductivity organic semiconductors.

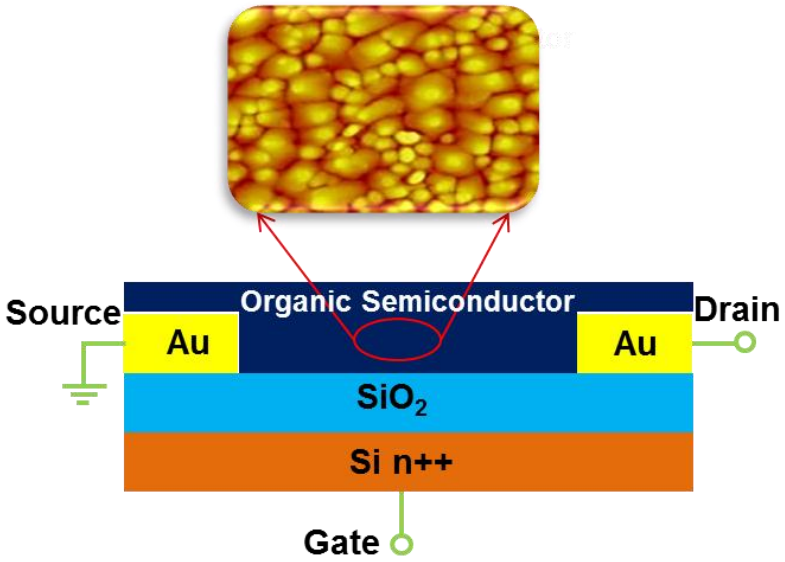

Figure 2.1: Schematic of a typical bottom-contact bottom-gate organic field effect transistor (OFET).

2.2 Organic Semiconductors for OFETs

Organic semiconductors are carbon-rich and pi-conjugated materials with semiconductor properties. The term conjugated refers as the existence of the alternative single and double carbon-carbon bond. Other components of the organic semiconductors are hydrogen and oxygen. Organic semiconductors can be classified into two categorize: small molecule and polymer regioregular polythiophene (P3HT) (Figure 2.2) [10]. In the small molecule organic semiconductors, such as pentacene, the carbon atoms form larger molecules and typically with benzene ring as basic unit and π-electrodes are delocalized through the molecules. On the other hand, in polymer carbon atoms form a long chain and the π-electrodes along the chain and form a one-dimensional π-electrodes system. Since the properties of the carbon atoms are the origin for

the both of small molecule and polymer semiconductor, their electronics transport properties are almost similar. A large number organic small molecules and polymers are used to fabricate the OFETs. Two representative and well-studied organic semiconductors (one small molecule and one polymer) are discussed in below.

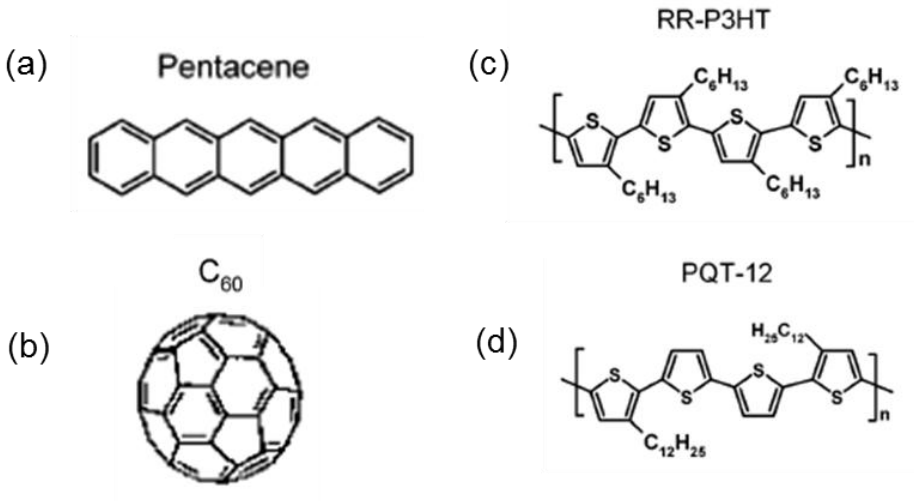

Figure 2.2: Organic semiconductors. Schematic representation of (a) pentacene and (b) Buckminsterfullerene (or buckyball) (C60) (b) regioregular poly(3-hexylthiophene) (RR-P3HT), (d) poly (3, 3 didodecylquarterthiophene) (PQT). Adapted from reference [5].

(a) Pentacene

Pentacene ($C_{22}H_{14}$) is one of the well-studied and most promising organic semiconductors for their potential application in future organic electronic devices [11, 12]. The highest occupied molecular orbital (HOMO), or ionization potential of the pentacene of is 5.1 eV. Transistors fabricated with pentacene usually shows p-channel transistor behavior. This is because the work function of Fermi level of gold (5.1 eV) is well matched with HOMO level of the pentacene, which results in a small barrier for holes (positive charge carrier) and a large barrier for the electrons. The common deposition technique of fabricating the pentacene device

is the vacuum evaporated method, and the vacuum evaporated pentacene thin film shows better polycrystalline structure than that of the solution processible polymers thin film. Due to their well crystalline structure (better morphology), the charge transport through the pentacene thin film is more efficient. Pentacene thin film transistors have shown higher mobility, better on-off ratio, and better reliability than that of the most other organic semiconductors [1].

(2) P3HT

Poly(3-hexylthiophene) (P3HT) $(C_{10}H_{14}S)_n$ is one of the first solution-processible organic semiconductors which was used to fabricate transistors. The HOMO level of the P3HT typically in the range of 4.9-5.0 eV [9], which is well- matched with work-function of the many air stable electrode material such as gold. The P3HT has excellent solubility in variety of solvent such as chloroform, and P3HT thin films can be prepared in different solution processible methods such as spin-coating, dip-coating, screen printing or inkjet printing. The P3HT thin films are microcrystalline structure and it is microcrystalline structure depends on several factors such as regioregularity, molecular weight, deposition conditions. The mobility of the regioregular P3HT thin film transistors varies by two order of magnitude depending on the solvent used and highest mobility has been achieved with chloroform solvent.

2.3 Device Structure of OFETs

The main component of the OFETs is organic semiconductors (OSC), which can be either conjugate polymers or small molecules organic semiconductors [1-2]. Relatively wide band gap organic semiconductors with band gaps in the range of 2-3 eV are used in fabricating the OFETs. Besides the OSC, the other major components of typical OFETs are source-drain electrodes with channel length (L) and width (W) that are contacted with OSC thin layer, gate

electrode which is separated from the OSC layer by a dielectric layer. The structure of OFETs depends on the arrangement of the components, which can be divided into bottom-gate bottom-contact, bottom-gate top-contact, and top-gate bottom contact and top-gate top-contact configurations [5]. The schematic of a bottom-contact bottom-gate OFET is shown OFETs in Figure 2.1. In these OFETs, the source and drain metal electrodes are fabricated using either photolithography or electron beam lithography (EBL) or combination of photolithography and EFL on substrate, and finally organic semiconductor is deposited on the electrodes. The most common substrate for the OFETs is heavily doped silicon (Si) wafer with a thermally grown insulating silicon dioxide (SiO_2) layer. The SiO_2 (dielectric constant of 3.9) is used as dielectric layer and heavily doped silicon (Si) wafer is used as the gate electrode. The major advantage of the bottom contact and bottom contact devices is that these OFETs can be fabricated with smaller device feature size through the photolithography or EBL techniques.

2.4 OFET Operation and Electrical Characterization

In order to operate OFETs, gate-voltage (V_g) is applied at the gate electrode and drain-voltage (V_d) is applied at the drain electrode. The source electrode are usually kept at ground ($V_d = 0\ V$). When a positive V_g is applied at the gate electrodes, the source electrode becomes more negative than the gate electrodes and the electron are injected from the source electrodes. On the other hand, when a negative V_g is applied at the gate electrodes, the source electrode becomes more positive than the gate electrodes and the holes are injected from the source electrodes. When V_g is applied at gate electrodes, charge carriers (holes due to negative V_g and electrons due to positive V_g) accumulate at near the dielectric/OSC interface and formed a conducting channel in the thin layer OSC in the between the source and drain electrodes (Figure 2.3).

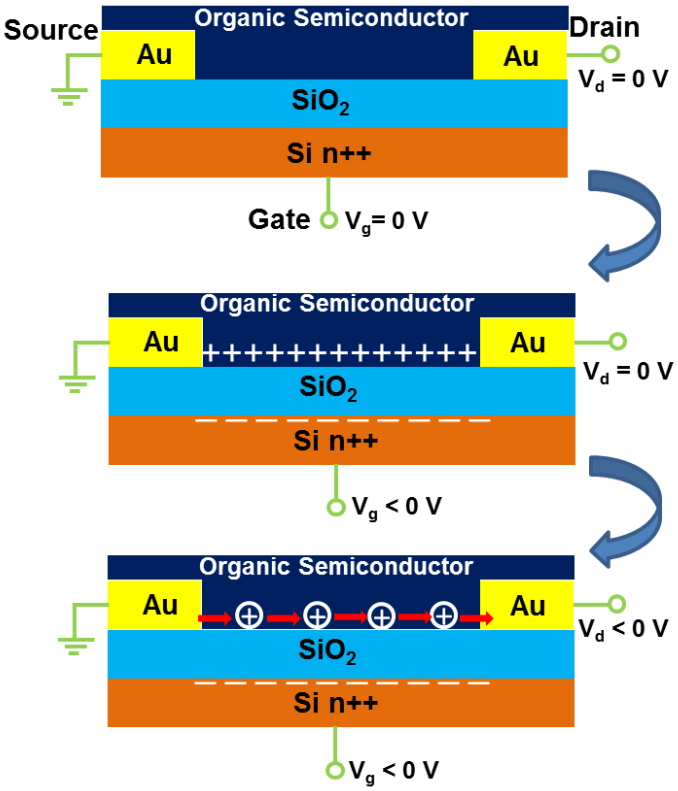

Figure 2.3: Schematic illustration of the operation of the OFETs at gate-voltage (V_g) and is drain-voltage (V_d).

The induced charge carriers and output current of the OFETs can easily be tuned by controlling the V_g. When V_d is applied at the drain electrodes, the charge carriers injection from the source electrodes into the OSC and then transport though the conducting channel to drain electrode. The output characteristics (I-V_d curves at different V_g) of a typical transistor are shown in Figure 2.4(a**)**. The current is increased linearly with bias voltage at the low bias regime, and it saturates at higher bias-voltage. Figure 2.4 (b) and 2.4 (c) show transfer characteristics (I-V_g curve) of the OFETs at linear regime and transfer characteristics at saturation regime.

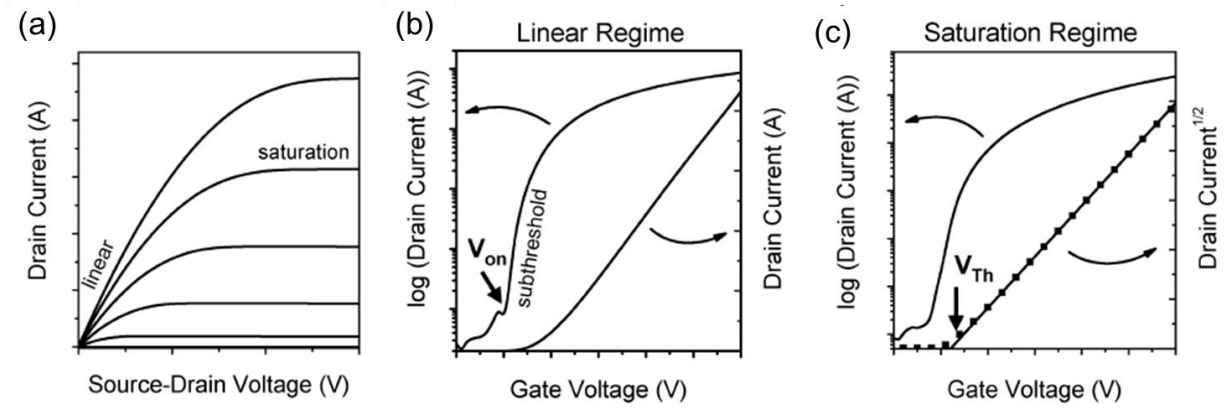

Figure 2.4: Transistor characteristics of typical OFETs (a) Output characteristics, (b) Transfer characteristics at linear regime and (c) Transfer characteristics at saturation regime. Adapted from reference [5].

(1) Mobility:

To determine the quality of the OFETs, one of the most important parameters is field effect mobility. The mobility of the devices is related to the efficiency of the charge carrier transport in the materials. The mobility is derived from linear regimes and saturation regimes. At low V_d, ($\left|V_d\right| > \left|V_g - V_t\right|$), drain current increase linearly with increasing V_d (known as linear regime of the transistor curve). When the $\left|V_d\right| < \left|V_g - V_t\right|$, I_d becomes independent of V_d and it saturates (saturation regime). The drain current in the linear and saturation regimes of the OFETs are given by Equation 1 and 2 respectively [2]:

$$I_D = \frac{WC_i\mu}{L}(V_g - V_t - \frac{V_d}{2})V_d \tag{2.1}$$

$$I_D = \frac{WC_i\mu}{2L}(V_g - V_t)^2 \tag{2.2}$$

Where C_i is the capacitance per unit area of the insulating layer, V_t is the threshold voltage, and the μ is the field effect mobility. The transconductance g_m is the change of the drain-current with gate voltage and it is calculated from the transfer curves:

$$g_m = \frac{\partial I_d}{\partial V_g} \tag{2.3}$$

The linear mobility of the OFETs is determined by extracting the (g_m). Using equation (2.1) the linear mobility is given by

$$\mu = \frac{L}{WC_i V_d} \frac{\partial I_d}{\partial V_g} \tag{2.4}$$

In the saturation regime the drain current varies with the square of gate-voltage. The threshold voltage is extracted from the slope of square root of drain current versus gate voltage curve and the saturation mobility is calculated using equation (2.5).

$$\mu_{sat} = \frac{2LI_{d,sat}}{WC_i(V_g - V_T)^2} \tag{2.5}$$

(2) Current On-Off Ratio

The current on-off ratio is the maximum-current (on-current) divided by the minimum-current (off-current) between source and drain electrodes. The definition of the current on-off ratio is somewhat arbitrary and there is no standard way of reporting the on-off. The voltage range (both gate-voltage and drain-voltage) for the measurement of current as function of gate-voltage are varies from studies to studies and the on-off ratio is calculated from the corresponding I-V_g curves.

The current on-off ratio is very important parameter for any organic transistors and it is particularly important for their application in flexible display and logic circuit. The high on-off ratio provides a high contrast in the organic flexible display and higher on-off ratio provides clear switching in between the on-state and off-state in the logic circuits. If the on-off ratio is low with a high on-current, even the circuit is in the off-state, the circuit will dissipate a large

amount of energy due to high off-current, which results in a large power dissipation. The lower power dissipation of logic circuit is important factors for their practical applications [7].

(3) Threshold Voltage

Threshold voltage (V_T) is the minimum gate-voltage at which conducting channel is formed in between the source and drain electrodes and current is started to flow of a transistor. At the threshold voltage, all the traps in the semiconductors are filled and thermally activated charge carriers begin to play a major rule in the transport of the transistors. The V_T can be determined from the *I-Vg* curves at different techniques such as by extrapolating a linear fit of the I_d-V_g plot (for low V_d), or $(I_d)^{½}$- V_g plot (for high V_d) to the $I_d = 0$ (Figure 2.4).

(4) Subthreshold Swing

Subthreshold Swing (*S*), also known as subthreshold slope, is defined as the rate at which drain current changes by one decade with the gate-voltages. A small value of subthreshold swing indicates a higher speed of the devices. The subthreshold swing is calculated from the transfer curves of the devices and it is given by

$$S = \left(\frac{d \ln I_d}{dV_g}\right)^{-1} \tag{2.6}$$

2.5 Limitation of Charge Injection at Metal/Organic Semiconductor Interface

The charge transport in the organic filed effect transistors mainly governed by the two processes: charge injection at metal electrode /organic semiconductor interface and charge transport through the channel formed in the organic semiconductor in between source and drain electrodes [13-19]. The schematic of charge injection and charge transport through the grain boundaries are illustrated in in Figure 2.5. It can be seen from this figure that at first charge

carriers are injected from the source electrode into the organic semiconductor though the electrodes/organic semiconductor interface and then the charge carriers transport though the transistor channel.

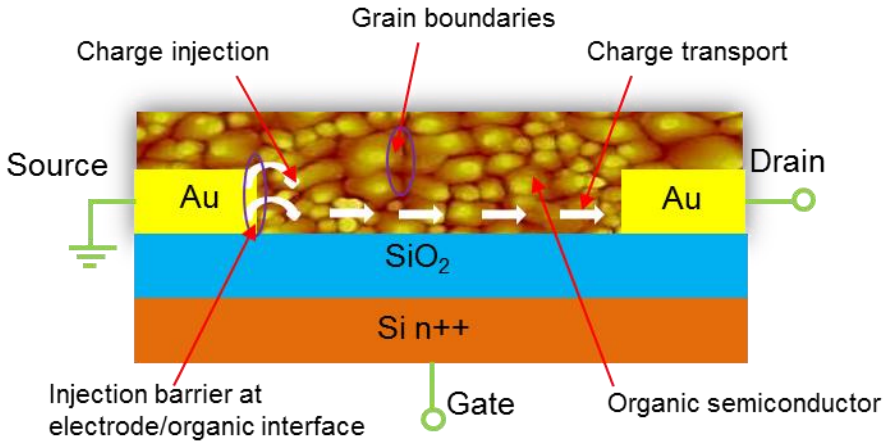

Figure 2.5: (a) The charge injection at the electrode/ organic semiconductor interface and charge transport though grain boundaries the channel of organic transistor.

In the p-channel transistor, holes have to be injected from the source electrode into the LUMO level, and in n-channel OFETs, the electrons need to be injected from the electrodes into the LUMO (lowest unoccupied molecular orbital) level of the organic semiconductors. In order to efficient injection from the electrode to organic semiconductors, the charge carriers have to overcome the charge injection barrier at between metal/organic semiconductor interfaces.

In Mott-Schottky model, the barrier height is defined by the difference of the metal work-function and the HOMO or LUMO level of the OSC (Figure 2.6 a) [13, 14]. The barrier formed at the metal/OSC interface known as Schottky barrier height. The hole injection barrier (Φ_{Bh}) and electrodes injection barrier (Φ_{Be}) depend on the position of the HOMO and LUMO with respect

to the Fermi level of the metal (E_{FM}) [13]. According the theoretical description of the metal/OSC contacts, electron injection barrier is given by

$$\phi_{B,e} = E_{FM} - E_{LUMO} = \phi_m - E_A \tag{2.7}$$

where, ϕ_m is the work-function of the metal, which is the energy the energy required to remove an electron from the Fermi level to vacuum level (VL), and E_A is the electron affinity of the OSC which is energy difference from the LUMO level to the vacuum level. The hole injection barrier is given by

$$\phi_{B,h} = E_{HOMO} - E_{FM} = E_I - \phi_m \tag{2.8}$$

Where, E_I is the ionization potential of the organic semiconductor which corresponds to the energy difference from the HOMO level to the vacuum level.

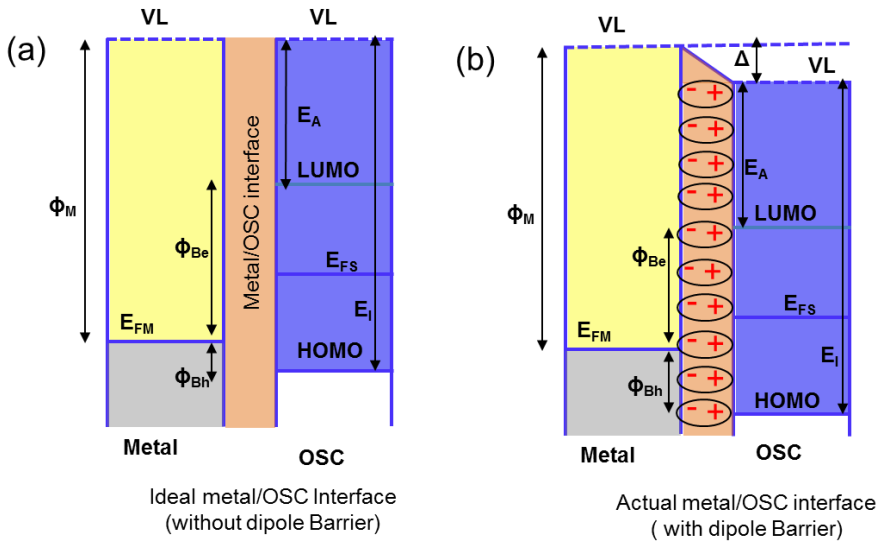

Figure 2.6: Energy band diagram of a contact at between a metal and OSC (a) without diploe barrier and (b) diploe barrier at the metal/OSC interface. The charge injection barrier height for electrode and hole are denoted by Φ_{Be} and Φ_{Bh}.

According to Mott-Schottky model, a good Ohmic contact is expected when the work-function of the metal electrodes is well-matched with HOMO level or LUMO of the OSC. Although Mott-Schottky model gives a general idea about the metal/OSC interface, the scenario of actual metal/OSC interface is more complicated, which cannot simply be explained by this model. Previous studies showed that Schottky barrier formed at the metal/OSC interface irrespective to work-function of the metal electrodes and geometry of the interface, known as Fermi level pining [19]. Even the work-function of the metal is well matched with the HOMO level of the OSC, in actual system barrier is formed at the interface due to diploe formation. The dipole layer is formed at the interfaces due to for various reasons such as charge transfer, covalent bonding, redistribution of the electrode cloud, image force induced polarization, permanent surface molecular dipole [13, 14, 19].

Because of the formation of dipole layer, the vacuum level of the OSC is shifted and makes a barrier at the interfaces, which is known as dipole barrier (Figure 2.6 b). The value of the dipole barrier is determined by the magnitude of the dipole layer formed at the interface. If a diploe barrier (Δ) is formed at metal/OSC interface then the injection barrier is modified from the simple equation 1 and 2 by Δ as follows [13]:

$$\phi_{B,e} = E_{FM} - E_{LUMO} = \phi_m - E_A + \Delta \tag{2.9}$$

$$\phi_{B,h} = E_{HOMO} - E_{FM} = E_I - \phi_m - \Delta \tag{2.10}$$

The formation of dipole barrier has a detrimental effect on the charge injection of the OFET. This is because the dipole barrier gives rise to a “push back” effect, a decrease of surface dipole potential energy of the metal surface in contact with the organic semiconductor [13,14].

As a result, the effective work- function of metal is reduced significantly. It is reported that when atomically clean gold with work function of ~ 5.2 eV is contacted with OSC in either top contact or bottom contact, the work-function of the gold is reduced to ~ 4.5 eV [13, 15, 20]. This shows that the effective work-function of the metal actually reduced significantly due to formation of diploe barriers at the interface. As a result dipole barrier increase the barrier, leading to a large contact resistance at metal/OSC interface and the charge injection is limited by the metal/OSC interfaces. In addition, the charge injection at metal/OSC interface is also limited by several factors such as presence of impurities, morphological discontinuities, interfacial traps, and structural disorder at the interfaces [13-15].

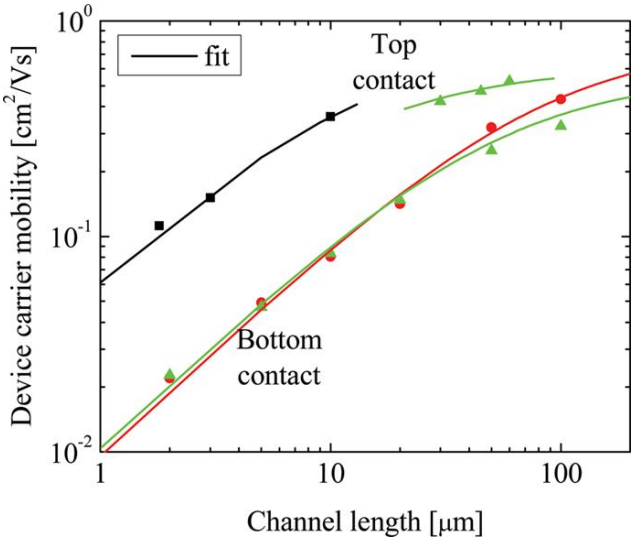

Figure 2.7: Variation of field effect mobility with channel length of the OFETs. Adapted from reference [21]

Because of the large interfacial barriers at metal/OSC interface, contact resistance becomes large and limits the charge injection in the OFETs [13-17,22-29]. This becomes more significant in the short channel devices. When the channel length is reduced; the contact resistance at metal/OSC interface becomes very high compared to the resistance of the organic

semiconductors in the channel, leading to a significant reduction in mobility (Figure 2.7) and current on-off ratio [25-29]. However, short channel OFETs is required in fabricating high switching speed OFETs. This is because the switching speed of transistors is inversely proportional to channel length, to increase the switching speed OFETs should fabricate with short channel [30].

To improve the charge injection from the metal electrodes into the organic semiconductors, several approaches has been developed and tested in the literature. The common approaches are control of the interfacial dipoles though thio-based self-assemble monolayers (SAMs), and charge injection layer in OFETs [31-33]. However, these techniques are strongly dependent on the materials or architecture. Improving charge injection using the matching electrodes is clearly not technologically appealing, because some of the electrode materials are not environment friendly .For example: low work-function metal have strong reactivity with air which results in poor stability of the OFETs. Although the use of the polar, thio-based self-assemble monomers is one of the most successful approaches for the controls of the metal/OSC interface barrier, this approach has shortcomings. The surface energy of the metal electrodes can be dramatically altered by growing of the SAMs on the electrodes. This may occurs in variation of work-function of the metal. In addition, the variation of the wettability induced by the SAM growth can have an effect on the film morphology at the metal/OSC interface [31].

2.6 Carbon Nanotube (CNT) Electrode for OFETs

In order to overcome the limitations of the metal electrodes, recently carbon nanotubes (CNTs) are considered as promising electrode materials in fabricating organic electronic devices.

Now we briefly discuss about the basic of CNTs and their electronic, optical and mechanical properties. Then we review and summarize the previous works on CNT electrodes for OFETs.

2.6.1 Properties of CNTs

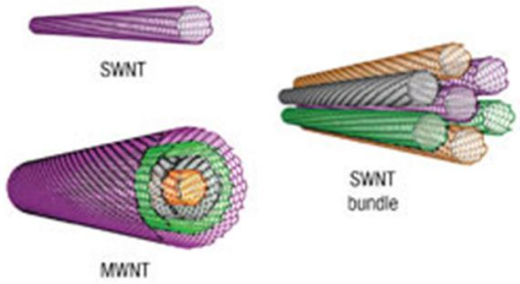

Figure 2.8: schematic representations of a single-walled carbon nanotube (SWNT), a multiwalled carbon nanotube (MWNT) and a bundle of SWNTs. Adapted from reference [34].

The carbon nanotubes are the sheets of the carbon atom rolled into one or more concentric hollow cylinders. The CNTs can be either single-walled carbon nanotube (SWNT) or multi-walled carbon nanotube (MWNTs). The single-walled carbon nanotube (SWNT) is a cylinder of single layer of graphene sheet, whereas the MWNT is a coaxial cylinder of multiple layers of graphene sheet [35, 36] (Figure 2.8). The typical diameter of an individual SWNT is in the range of 1-3 nm and length up to few cm. Due to high aspect ratio CNTs are considered as one-dimensional materials. The electronic properties of the CNT strongly depend on rolling on the graphene sheet. Depending on the chirality CNTs can be either semiconducting or metallic. The electronic and optical properties of the individual semiconducting CNT depends on the band gaps and that the band gap varies inversely proportional to CNT diameter as $E_g \sim 1/r$, where E_g is the band gap and r is radius of the CNTs. The individual semiconducting SWNT field effect transistors have shown extraordinary device performances such as mobility, and current on-off

ratio. The semiconducting SWNT have shown a high mobility up to 100 000 cm^2/Vs as well as high conductivity up to 400 000 S/cm [35].

Due to their exceptional electronic, optical and mechanical properties, CNT thin films, both randomly distributed (Figure 2.9 a) or aligned array CNTs, have been considered promising materials in the next-generation devices. The CNT thin film of thickness 50-100 nm shows high optical transparency in the visible light and high electrical conductivity [35, 37]. The electronic and optical properties of the CNT thin films are strongly depend on chirality of the nanotube, purity, doping, length, orientation of nanotubes, thin thickness. For example, resistivity of the thin film is decreased with increasing the film thickness (Figure 2.9 b, c). The CNT thin films have extraordinary mechanical properties such as mechanical flexibility, strechability, and transparency (Figure 2.9 d). This suggest that CNT thin films can be used as transparent and conducting electrodes in the optoelectronics device applications such as solar cells [38], light emitting diodes [37] and organic field effect transistors [39-48]. One of the most important properties of CNT thin films is their high work-function which is in the range of 4.7-5.2 eV,[35]. The work-function of the CNT is well-matched with HOMO level of the most of p-type organic semiconductors. This suggest that CNT thin films can be used as source and drain electrode material in the p-channel organic transistors, and as an anode in the organic solar cell.

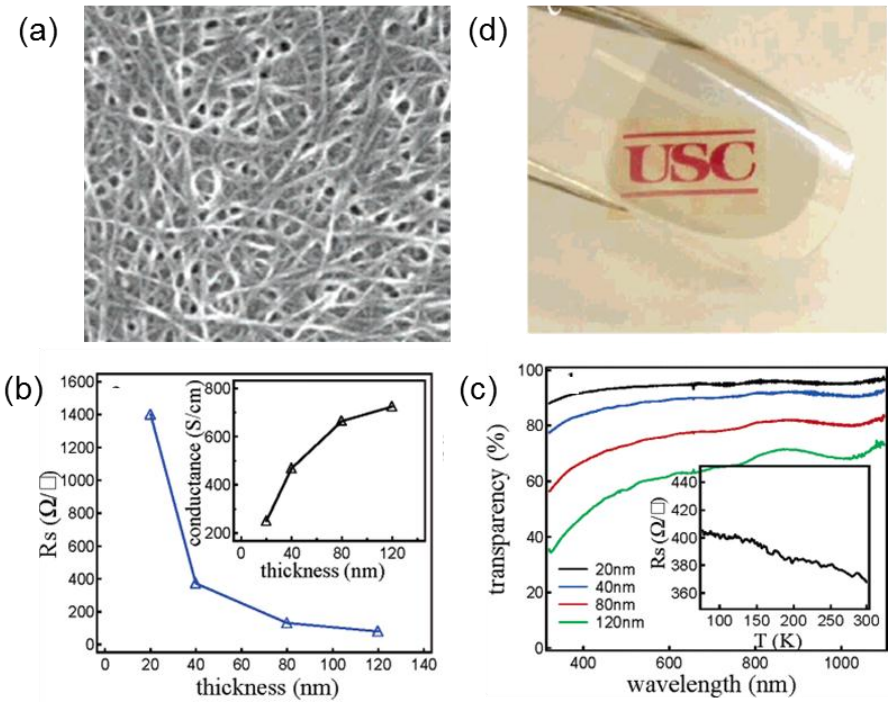

Figure 2.9: (a) SEM images of carbon nanotube thin film. (b) Sheet resistance versus film thickness of SWNT films. Inset: conductivity versus film thickness. (c) Transmittance spectra for SWNT films of thickness 20, 40, 80, and 120 nm. The transmittance of the SWNT films decreases monotonically with the film thickness. The 20 and 40 nm films exhibit sufficiently high transparency (>80%) over a wide spectral range from 300 to 1100 nm. Inset: sheet resistance versus temperature curve taken with a SWNT film of 40 nm in thickness. Adapted from reference [37].

In addition, since carbon is the common material in the both CNTs and organic semiconductors, a better interfacial contact at the CNT/organic semiconductor interface is expected due to a strong π-π interaction between the CNTs and organic semiconductors.(Figure 2.10) [49]. Another important feature of the CNTs is that they have electric field emission properties due to their one dimensional structure and it is believe that the field emission property enhanced charge injection from the CNT into the organic semiconductors. The reason for such an enhancement is that when an electric field is applied in CNT electrodes, a large local field is generated at the nanotube apex and increases charge injection.

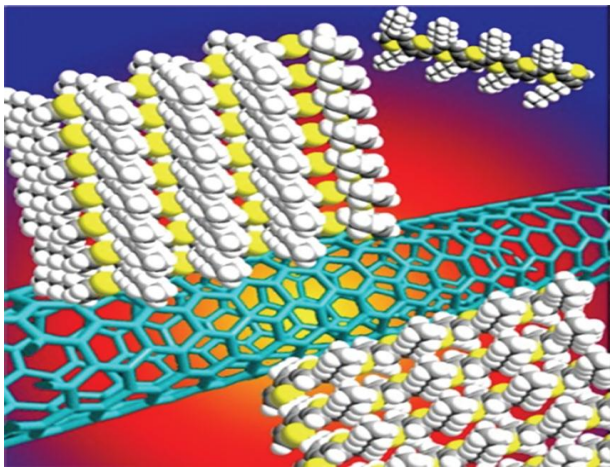

Figure 2.10: Supramolecular structures of CNTs and organic semiconductors due to Strong π-π interaction. Adapted from reference [49]

2.6.2 Progress in OFET fabrication with CNT Electrodes

Because of the extraordinary electrical, optical, and mechanical properties, carbon nanotubes have been considered as a promising electrode material for organic electronics devices. Recently, CNTs have been used as electrode materials to fabricate organic field effect transistors [39-48]. Carbon nanotube electrode has been fabricated using both the individual CNT as well as CNT thin films. Based on number of CNTs and their orientations in the electrodes, these techniques can be classified into three major categories: (a) Individual CNT electrodes, (b) random network CNT electrodes, and (c) CNT/polymer composite electrodes (Figure 2.11). Although different research groups used their own approaches to fabricate CNT electrodes and OFETs using CNT electrodes, performance of the OFETs with CNT electrodes are higher that of their control OFETs with metal electrodes. All the techniques for the CNT electrode fabrication have their own advantages and limitations. Now, we discuss different techniques of the CNT electrode fabrication, their advantages as well as the limitation involved in the processes.

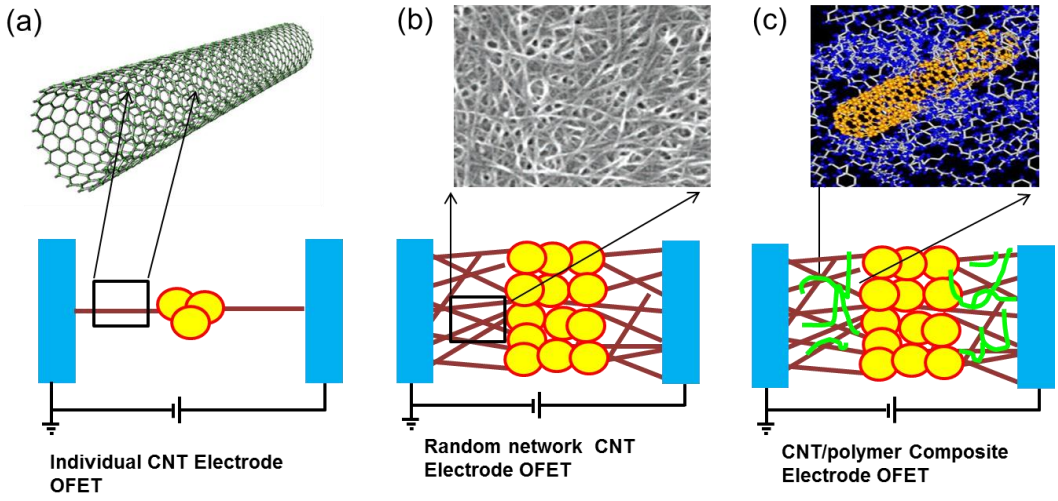

Figure 2.11: Schematic diagram of the OFETs fabrication using (a) individual CNT electrode (b) Random network CNT electrode and (c) CNT/polymer composite electrodes. SEM image of carbon nanotube adopted from reference [37].

(1) Individual CNT Electrodes

The individual CNT electrodes are fabricated by cutting the CNTs and leaving the two ends separated by a nano-gap. The most common and simplest technique in fabricating nanogap electrode from individual CNT is the electrical breakdown (Figure 2.12) [39-42]. Individual CNT electrodes were fabricated by the electrical breakdown of the SWNTs [39], as well as MWNTs [42]. In this technique, the CNTs were deposited onto silicon wafer by using either chemical vapor deposition spin-coating or arc-discharging method followed by making top electrical contacts by conventional lithography and thermal deposition of metal. Then, a high current is applied between the two metal leads. As a result the nanotubes break due to joule heating, which is known as electrical breakdown [51]. The each ends of the nanotubes are served as source and drain electrodes for the organic transistors.

Fabrication of OFETs using individual CNT electrodes has been demonstrated by depositing the organic semiconductors such as pentacene [40], P3HT [41], and fullerene (C60). [45] The organic semiconductors were deposited into the electrode gap onto the CNT electrodes by either in solution phase or thermal evaporation method. A composite of atomic force microscopy (AFM)/ scanning electron microscopy (SEM) image of the pentacene OFETs connected by individual CNT source and drain electrodes is shown in Figure 2.12 a and 2.12 b. The channel length of the transistor is 40 nm (here gap size is the channel length) and channel width is 2.5 nm (CNT diameter). The characteristics of the OFETs with individual CNT electrodes are in Figure 2.12c. The output curve of the transistor shows superliner behavior; which is a signature of short channel effect [25-29]. The short channel effect in the nanotransistor with high oxide thickness (comparable to the channel length) is not unexpected due to inefficient gate coupling. The transfer curves shows a typical p-type transport characteristics with current on-off ratio of 10^2 and on-current of 2 nA at V_d = 8V. The performance of the nanotransistor using CNT electrodes is better than that of transistor fabricated using gold (Au) electrode with channel length of 20 nm and width of 250 nm. By normalizing the channel width, the estimated on-current of the transistor with individual CNT electrode is about 100 times higher than that on-current of the transistor fabricated using gold (Au) electrode. The improved devices performance using CNT electrodes is attributed to the efficient electron injection from the CNT electrode into the pentacene. Although all OFETs tested in this study have shown the similar on-current, however, the on-off various from 10 to 10^4. This variation of the on-off ratio is attributed to the variation in the nanotube diameter because small variations in nanotube diameter significantly alter the electrostatic in the interface of the nanotube/pentacene [40].

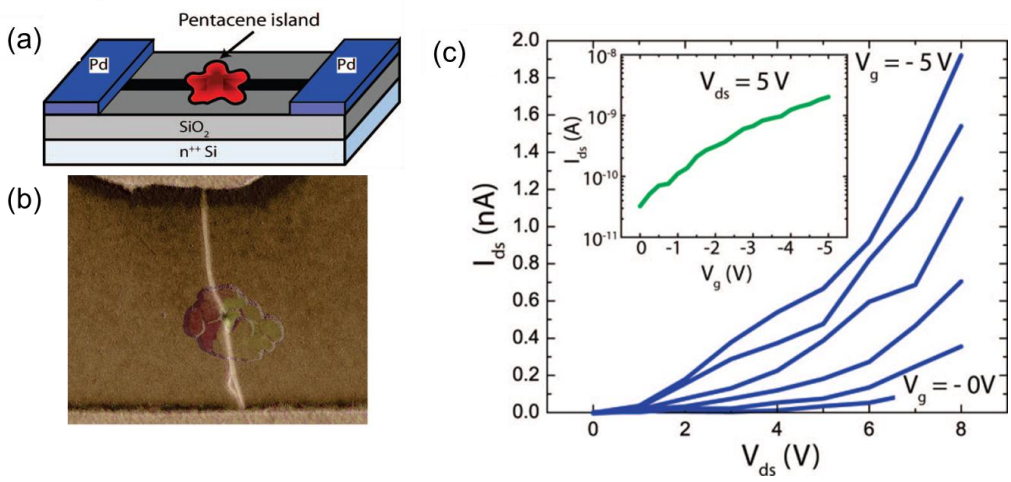

Figure 2.12: (a) Schematic diagram (top) of an individual pentacene island contacted by two metallic carbon nanotubes that act as source and drain electrodes. (b) Pentacene nanotransistor having a channel length of 40 nm and width of 2.5 nm (nanotube diameter). (c) Transfer and output (inset) characteristics of the corresponding device. The transfer characteristic is shown using Vds = 5 V. Adapted from reference [40].

The electric breakdown method for fabricating of nanogap electrodes has both the advantages as well as disadvantages. The advantages of this method are that it is simple, easy and cost-effective, as it does required the sophisticated nanofabrication tools such as EBL instruments. On the other hand, the major limitation is that the electrode gap sizes formed by the electrical breakdown are not well-controlled. For example, C. M. Aguirre et al found the electrode gap is in the range of ~ 20-200 nm, whereas D. et al. found that it is in the range of 10-60 nm [40, 43]. The variation of the nanotube electrode gap may be related to several factors such as nanotube length, diameter, substrate, breaking environments, charity of the CNTs, and defect in the CNTs.

Controlled fabrication of the individual CNT electrodes has been demonstrated by Guo et al. They formed nanotube electrodes by cutting the individual nanotube using precise local oxidation though window opened by the electron beam lithography (EBL) [39]. In this study,

individual CNTs with diameter of 1-2 nm were grown by CVD on silicon substrate followed by contact with metallic electrodes (5 nm Cr and 50 nm gold) with a separation of ~ 20 μm. The CNTs devices were coated with polymethylmethacrylate (PMMA) by spin coating and a window less than 10 nm were opened by EBL. Finally the nano-gap electrodes of 10 nm were fabricated by locally oxygen plasma ion etching the nanotube through the open window. Focused ion beam as well as electron beam induced oxidation methods are also used to fabricate nano-gap CNT electrodes [45, 51]. K. Horiuchi et al used focused Ga^{2+} ion beam in fabricating individual CNT electrode using MWNT contacted by metal pads on a silicon substrate.

(2) Random Network CNT electrodes

As we discussed in the last section that individual CNT electrode can be used as an efficient point contact for organic nanotransistor. Although nanotransistor has potential applications in the area of nanoelectronics, they are not suitable for large area organic electronics. In order to large scale application, the large area transistors are required that required long channel length and width electrodes. Carbon nanotube random network (CNT thin film) has been used as electrode materials for fabricating the large area organic transistor. To fabricate random network CNT electrodes, at first CNT this are deposited by both vapor-phase and solution-phase deposition methods, such as CVD [44], transfer-printing of CVD grown CNT [53], surface selective deposition [52], spray coating [48] and airbrushing [53].

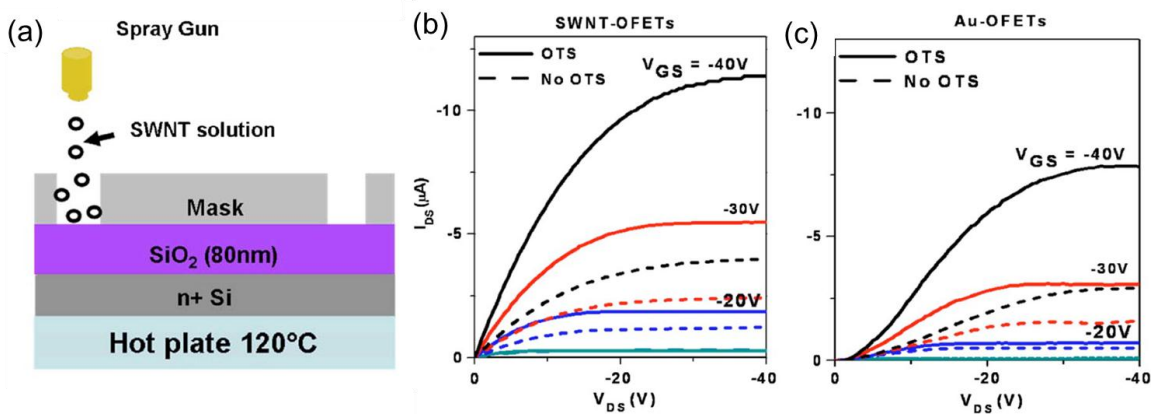

Figure 2.13: (a) Schematic of the fabrication the SWNT electrode by spray coating technique. Output characteristics of a representative PQT OFET with (b) SWNT electrodes, and (c) gold electrode. Adapted from reference [48].

C. H. Chang et al reported pentacene based thin film transistor with MWNT source and drain electrodes [44]. They formed the MWNT source and drain electrodes by depositing and pattering a Fe/Ti catalyst layer followed by growing of MWNT though the CVD (Figure 2.13). Finally, a thin layer of the pentacene film (~40 nm) was deposited using thermal evaporation to fabricate the transistor. The pentacene transistor with MWNT exhibits good device performance with saturation mobility of 0.14 $cm^2/(V.s)$, on-off ratio of 10^6 and low contact resistance (30 kΩ-cm) at V_g = -50V. Similarly, Q. Cao et al fabricated transparent and flexible OFETs using CNT network electrodes which are formed by transfer-printing of nanotube grown by CVD [46]. Although OFETs fabricated using CVD grown CNT electrodes shown improved performance, this method has limitations in the practical application. This is because the CVD method is expensive and laborious. In addition, in the CVD method the CNT electrodes are fabricated at temperature up to 700 ^{0}C. Therefore, CVD is not a suitable method for fabricating CNT electrode for low-cost, and low-temperature processible organic electronic devices.

Solution-processed carbon-paste electrode fabrication using surface selective deposition techniques was demonstrated by Wada et al [52]. In this process a carbon paste solution is deposited on the region and the ultraviolet light irradiation is used to remove the self-assembled monolayers. The resulting CNT thin film using this process shows mechanical and thermal stability. The CNT paste electrodes of channel length of 150 µm and width 1000 µm were used to fabricate OFETs using pentacene as well as P3HT. In this study, it is found that the performances of these OFETs are higher than the corresponding the control devices using gold electrodes. Similar to the carbon-paste electrode, Zhang et al used spray deposited SWNT as the bottom contacted source and drain electrodes for poly (3, 3 didodecylquarterthiophene) (PQT) based OFET[48]. The schematic of the CNT electrode fabrication by spray coating technique is shown in Figure 2.13a, where the electrodes dimension were defined by photo resist and masks and CNT solution is deposited by spray coating. Finally, the transistors were fabricated by the spin coating of the PQT solution onto the CNT electrode.

The output characteristics of a representative PQT OFET with CNT electrodes and gold electrodes are shown in Figure 2.13 b and 2.13 c. It is clearly seen in this Figure that the output current of the PQT transistor with CNT electrode is higher than that of the PQT transistor with gold electrodes. In addition, compare to gold contact PQT OFET, the CNT contacted PQT OFET shows higher mobility of 0.12 cm^2/V.s and higher on-off ratio of 10^6. The linear behavior of the output curves at low bias of the PQT transistor with CNT electrode indicates excellent interfacial contact at between the CNT and PQT. It is believed that the improved device performance of the CNT contact PQT OFETs is due to the low injection barrier. A. Southard et al has shown another easy and inexpensive method for fabricating of solution-processed CNT electrode [53]. They fabricated CNT electrodes from airbrushed CNT thin films with sheet resistance < 1 kΩ/sq and

transparency >80%. They fabricate an all-carbon transparent, flexible organic thin film transistor in which pentacene used as active channel materials, and the CNT films are used as a gate, source, and drain electrodes. They found that performance of the airbrushed CNT electrode is similar to the performance of the CNT electrodes fabricated from CVD grown.

(3) CNT/polymer Composites Electrodes

CNT/polymer composites have also attracted special interest to the researchers as electrode material for the OFETs. The composites materials are not only demonstrate enhanced the properties of the individual components but also provide additional functionalities. In addition, the CNT/polymer composite is cheap and printable, which allow fabricating of low cost organic devices. The development of the CNT/polymer composite pattern without degradation of CNT properties plays an important rule to fabricate the CNT/polymer composite electrodes and controlled design of such pattern is the key challenge for practical application of the composite electrodes in organic electronics.

M. Lefenfeld et al demonstrated the high-performance organic transistors with printed dinonylnaphalene sulfonic acid doped polyaniline/SWNT (DNNSA-PANI/SWNT) electrode (Figure 2.14) [54]. The thickness of the electrodes is ~ 1 μm with a conductivity of 3 S cm. The DNNSA-PANI/SWNT electrodes formed the excellent contact with both the p-type and n-type OSC. The minimum channel length that used for electrode fabrication was 15 μm. The DNNSA-PANI/SWNT electrodes were fabricated using thermal imaging, a technique that enables the printing of multiple layer, successive layers via transferring conducting polymer from the donor sheet to circuit using localized laser-induced heating [56]. The printed-transferred method does suffer from any issue about chemical incompatibilities that commonly arise in the solution

processed multilayer plastic circuit. However, the edges of the electrodes fabricated in this method are not well defined, which makes difficult to control the dimension of electrodes.

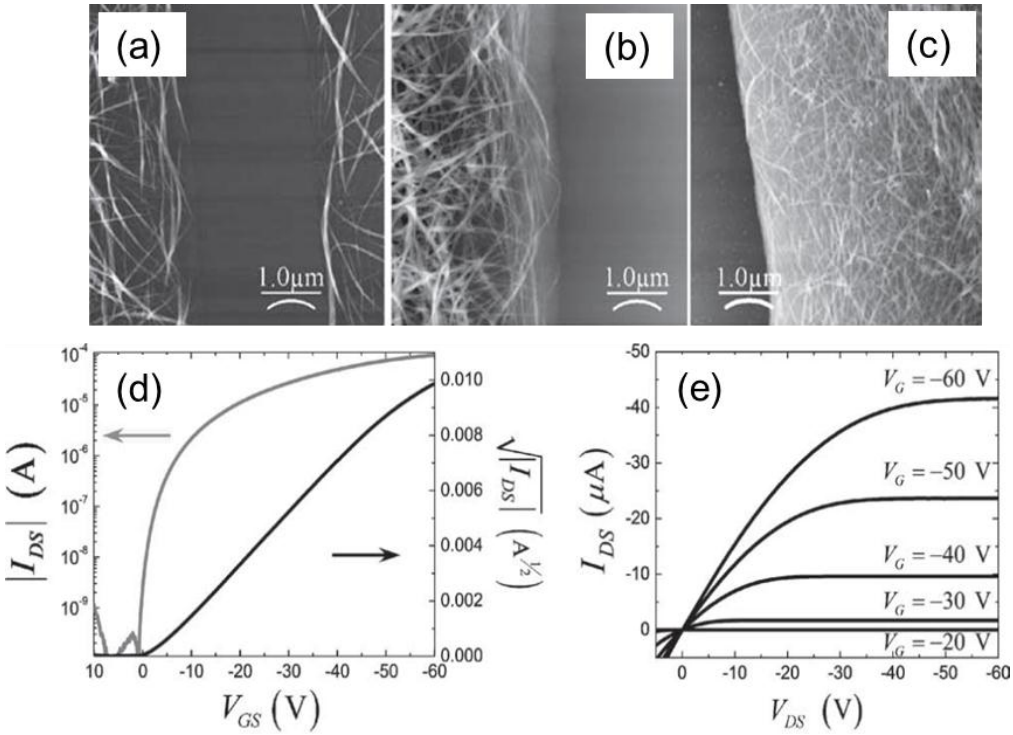

Figure 2.14: (a) AFM image of a 1:1 P3HT: SWNT composite deposited on a surface with prepatterned regions of SiO_2 and Octadecyltrimethoxysilane (OTMS) , illustrating successful resolution of 3 μ m feature sizes. (b) AFM image of a 1:1 P3HT: SWNT composite deposited on a surface with prepatterned regions of SiO_2 and OTMS, illustrating a typically achievable tube density gradient. (c) AFM image of a 1:1 P3HT: SWNT composite deposited on a surface with prepatterned regions of Au and OTMS. (d) Transfer curve, SWNT/pentacene and (e) Output curves, SWNT/pentacene device. Adapted from reference [55].

In order to achieve better resolution of the electrode channel, solution-processed selective surface functionalization techniques has been used by Hellstrom et al [55]. They deposited the Al of 40 nm using shallow masks by thermal evaporation followed by self-assembled monolayer of octadeyltrimethoxysilane treatment. After silane treatment, Al was etched away and 1:5 rr-P3HT: SWNT composite was spin-casted. Finally, the samples were annealed and then

immersed in chloroform and sonicated until any stray materials were removed. Compared to the patterning on pristine the CNT, the CNT/polymer composite shows improved the reliability of the pattering process and improved the overall electrode uniformity. In addition, the minimum feature size of CNT electrodes of 3 μm over areas of 3 cm^2 is achieved. The typical sheet resistance of the CNT/polymer composite electrode is in the range of 1-4 kΩ/sq. By integrating of the CNT/polymer composite electrodes of channel length of 50-150 μm with the pentacene and C60, both p-type and n-type OFETs were fabricated. These devices have showed excellence field effect transistors with mobility of 0.2-0.7 cm^2/(V.s) for pentance devices and 0.6-1.5 cm^2/(V.s) for C60 devices [55]. Most recently, Chang et al used have demonstrated the solution based direct pattering of the SWNT/poly(3, 4 - ethylenedioxythiophene)-poly(styrenesulfonate)(PEDOT-PSS) composite electrodes by microcontact printing [56] These pattern electrodes show high transparency, conductivity and electromechanical stability.

In addition to SWNTs, MWNTs are also good candidate for to be used as electrode for the organic transistor due to their high conductivity and mechanical strength [57]. However, there are some limitations to fabricate and application of MWNT electrodes. The MWNT are not well soluble in solution and their work is low, which is not matched with HOMO level of the p-type OSC. To address this issue, Hong K et al showed that if MWNTs are wrapped with PSS, they become water soluble and their work-function are increased to 4.83 eV, which is 0.36 higher than that of untreated MWNTs [59].The mobility of the pentacene transistor fabricated using wrapped MWNTs (0.043 cm^2/V.s) have shown four time higher than mobility of the control devices fabricated using gold electrodes (0.011 cm^2/V.s). The major advantage of the CNT/polymer composite electrodes are solution processible cover the large area and low-cost fabrication.

2.7 Why There Is a Need More Study On CNT Electrodes

Although all research groups have showed improved device performance with CNT electrodes than that of the control OFET devices with metal electrodes, fabrication of high-performance OFETs with CNT electrodes is still remained a significant challenge. The reported CNT electrodes were fabricated from the individual CNTs, random network CNTs and CNT/polymer composite electrodes [40-49,51-57]. Individual CNTs have shown as efficient point contact for nano-scale OFET, they are not appropriate for practical application in large area electronic devices. The most commonly used approach is to use random network of CNTs as electrode materials, which were fabricated using either transfer printing, spray coating, or airbrushing method. In these methods, short channel length CNT electrodes cannot be fabricated due their low resolution, which are required for fabricating the high-performance OFETs. In addition, optimum charge injection may not occur due to the random alignment of CNT tips in the electrodes. One possible drawback of the CNT/polymer composite electrodes is that when gate voltage is applied to the OFET, a part of the applied gate voltage also modulates the electrodes which affect the device performance. As a result, the performance parameter such as mobility extracted from the OFETs contacted with CNT/polymer composite electrodes may earthier under or overestimated. In another report, CNT array electrode was fabricated by anchoring CNTs onto titanium contact using vacuum filtration method [40]. In this electrode pattern, CNTs appears to be random, density of the CNT is very low and dimension of the electrodes appears to be not well defined which may cause charge injection not only from the CNT electrode but also from the base metal electrode where CNTs are anchored.

Therefore, in order to fabricate high-performance OFETs we need a new approach for fabricating CNT electrodes which should have well defined channel length and width with high

resolution, highly conducting, and metallic in nature. The more efficient charge injection may be obtained if CNT electrode is fabricated from ultra-high density aligned array where individual CNTs are closely packed with tips parallel to each other's with well-defined channel lengths. In addition, electrode fabricated aligned array CNTs they may provide more homogeneity from electrode to electrodes and can cover large areas.

In addition to limitation of the CNT electrodes fabrication techniques, the nature of the CNT/OSC interface is not understood from the previous work. In particular, charge injection and transport mechanisms in the device with CNT electrode are still unexplored. Therefore, fabricating the high-performance OFETs with aligned array CNT electrodes, understanding the charge injection and transport mechanism, and determining the charge in injection barriers at the CNT/OSC interface are of great importance for achieving the overreaching goal of the CNT electrodes in organic electronics.

2.8 References

1. H. Klauk, Organic Thin-Film Transistors. *Chem. Soc. Rev*. **39**, 2643 (2010).

2. C. D. Dimitrakopoulos, P. R. L. Malenfant, Organic Thin Film Transistors for Large Area Electronics. *Adv.Mater*. **14**, 99 (2002).

3. Y. Guo, G. Yu, Y. Liu, Functional Organic Field-Effect Transistors. *Adv.Mater*. **22**, 4427 (2010).

4. D. Braga, G. Horowitz, High-Performance Organic Field-Effect Transistors. *Adv.Mater* **21**, 1473 (2009).

5. J. Zaumseil, H. Sirringhaus, Electron and Ambipolar Transport in Organic Field-Effect Transistors. *Chem. Rev.* **107**, 1296 (2007).

6. Y. Chen, J. Au, P. Kazlas, A. Ritenour, H. Gates and M. McCreary,Electronic paper: Flexible active-matrix electronic ink display. *Nature* **423**, 136 (2003).

7. B. Crone, A. Dodabalapur, Y. Y. Lin, R. W. Filas, Z. Bao, A. LaDuca, R. Sarpeshkar, H. E. Katz and W. Li, Large-scale complementary integrated circuits based on organic transistors. *Nature* **403**, 521 (2000).

8. G. Horowitz, Organic Field-Effect Transistors. *Adv.Mater* **10**, 365 (1998).

9. T. B. Singh, N. S. Sariciftci, Progress In Plastic Electronics Devices. An. Rev.Mater. Res.**36**, 199 (2006).

10. X. Zhang, Device Engineering Of Organic Field-Effect Transistors toward Complementary Circuits, *Ph.D. Thesis*, (2009).

11. P. T. Herwig, K. Müllen, A Soluble Pentacene Precursor: Synthesis, Solid-State Conversion into Pentacene and Application in a Field-Effect Transistor. *Adv.Mater* **11**, 480 (1999).

12. J. E. Anthony, J. S. Brooks, D. L. Eaton, S. R. Parkin, Functionalized Pentacene: Improved Electronic Properties from Control of Solid-State Order. *J. Am. Chem. Soc*. **123**, 9482 (2001).

13. H. Ishii, K. Sugiyama, E. Ito, K. Seki, Energy Level Alignment and Interfacial Electronic Structures at Organic/Metal and Organic/Organic Interfaces. *Adv.Mater* **11**, 605 (1999).

14. S. Braun, W. R. Salaneck, M. Fahlman, Energy-Level Alignment at Organic/Metal and Organic/Organic Interfaces. *Adv.Mater* **21**, 1450 (2009).

15. S. D. Wang, T. Minari, T. Miyadera, K. Tsukagoshi, Y. Aoyagi, Contact-Metal Dependent Current Injection In Pentacene Thin-Film Transistors. *Appl. Phys. Lett* **91**, 203508 (2007).

16. D. Natali, M. Caironi, Charge Injection in Solution-Processed Organic Field-Effect Transistors: Physics, Models and Characterization Methods. *Adv.Mater* **24**, 1357 (2012).

17. J. C. Scott, Metal-Organic Interface And Charge Injection In Organic Electronic Devices. J. Vac.Sci.& Tech.A: **21**, 521 (2003).

18. G. Hill, A. Rajagopal, A. Kahn, Y. Hu, Molecular Level Alignment At Organic Semiconductor-Metal Interfaces. *Appl. Phys. Lett.* **73**, 662 (1998).

19. Z. Liu, M. Kobayashi, B. C. Paul, Z. Bao, Y. Nishi, Contact Engineering For Organic Semiconductor Devices Via Fermi Level Depinning At The Metal-Organic Interface. *Phys. Rev*.B **82**, 035311 (2010).

20. W. Osikowicz, M. P. d. Jong, S. Braun, C. Tengstedt, M. Fahlman and W. R. Salaneck Energetics At Au Top And Bottom Contacts On Conjugated Polymers. *Appl. Phys. Lett* **88**, 193504 (2006).

21. M. Marinkovic, D. Belaineh, V. Wagner, D. Knipp, On the Origin of Contact Resistances of Organic Thin Film Transistors. *Adv.Mater*. **24**, 4005 (2012)

22. A. K. Thakur, A. K. Mukherjee, D. M. G. Preethichandra, W. Takashima, K. Kaneto, Charge Injection Mechanism Across The Au-Poly(3-Hexylthiophene-2,5-Diyl) Interface. *J.Appl. Phys*. **101**, 104508 (2007).

23. T. Minari, T. Miyadera, K. Tsukagoshi, Y. Aoyagi, H. Ito, Charge Injection Process In Organic Field-Effect Transistors. *Appl. Phys. Lett.* **91**, 053508 (2007).

24. T. N. Ng, W. R. Silveira, J. A. Marohn, Dependence of Charge Injection on Temperature, Electric Field, and Energetic Disorder in an Organic Semiconductor. *Phys. Rev. Lett*. **98**, 066101 (2007).

25. T. Hirose, T. Nagase, T. Kobayashi, R. Ueda, A. Otomo and H. Naito, Device Characteristics Of Short-Channel Polymer Field-Effect Transistors. *Appl. Phys. Lett*, **97**, 083301 (2010).

26. G. S. Tulevski, C. Nuckolls, A. Afzali, T. O. Graham, C. R. Kagan, Device Scaling In Sub-100 Nm Pentacene Field-Effect Transistors. *Appl. Phys. Lett.* **89,** 183101, (2006).

27. Y. Chen, I. Shih, Scaling Down Of Organic Thin Film Transistors: Short Channel Effects And Channel Length-Dependent Field Effect Mobility. *J.Mater.Science* **44**, 280 (2009).

28. J. Z. Wang, Z. H. Zheng, H. Sirringhaus, Suppression Of Short-Channel Effects In Organic Thin-Film Transistors. *Appl. Phys. Lett*, **89**, 083513 (2006).

29. J. N. Haddock, X. Zhang, S. Zheng, Q. Zhang, S. R. Marder and B. KippelenA Comprehensive Study Of Short Channel Effects In Organic Field-Effect Transistors. *Org. Electron*. **7**, 45 (2006).

30. J. Collet, O. Tharaud, A. Chapoton, D. Vuillaume, Low-voltage, 30 nm channel length, organic transistors with a self-assembled monolayer as gate insulating films. *Appl. Phys. Lett.* **76**, 1941 (2000).

31. S. A. DiBenedetto, A. Facchetti, M. A. Ratner, T. J. Marks, Molecular Self-Assembled Monolayers and Multilayers for Organic and Unconventional Inorganic Thin-Film Transistor Applications. *Adv.Mater* **21**, 1407 (2009).

32. S. Kobayashi et al., Control of carrier density by self-assembled monolayers in organic field-effect transistors. *Nature Mater*.**3**, 317 (2004).

33. B. H. Hamadani, D. A. Corley, J. W. Ciszek, J. M. Tour, D. Natelson, Controlling Charge Injection in Organic Field-Effect Transistors Using Self-Assembled Monolayers. *Nano Lett*. **6**, 1303 (2006).

34. M. C. Hersam, Progress towards monodisperse single-walled carbon nanotubes, Nature Nanotech. **3**, 387 (2008)

35. L. Hu, D. S. Hecht, G. Gruener, Carbon Nanotube Thin Films: Fabrication, Properties, and Applications. *Chem. Rev*. **110**, 5790 (2010).

36. P. Avouris, Z. Chen, V. Perebeinos, Carbon-based electronics. *Nature Nanotech*. **2**, 605 (2007).

37. D. Zhang, K. Ryu, X. Liu, E.Polykarpoy, J. Ly, M. E. Thompson, C. Chow, Transparent, Conductive, and Flexible Carbon Nanotube Films and Their Application in Organic Light-Emitting Diodes. *Nano Lett*. **6**, 1880 (2006).

38. M. W. Rowell, Mark A. Topinka, Michael D. McGehee, Organic Solar Cells With Carbon Nanotube Network Electrodes. *Appl. Phys. Lett.* **88**, 233506 (2006).

39. X. Guo, J. P. Small, J. E. Klare, Y. Wang, M. S. Purewal, I. W. Tam, B. H. Hong, R. Caldwell, L. Huang, S. O'Brien, J. Yan, R. Breslow, S. J. Wind, J. Hone, P. Kim and C. Nuckolls, Covalently Bridging Gaps in Single-Walled Carbon Nanotubes with Conducting Molecules. *Science* **311**, 356 (2006).

40. C. M. Aguirre, C. Ternon, M. Paillet, P. Desjardins, R. Martel, Carbon Nanotubes as Injection Electrodes for Organic Thin Film Transistors. *Nano Lett*. **9**, 1457 (2009).

41. P. F. Qi, A. Javey, M. Rolandi, Q. Wang, E. Yenilmez and H. J. Dai, Miniature Organic Transistors With Carbon Nanotubes As Quasi-One-Dimensional Electrodes. *J.Am.Chem. Soc*. **126**, 11774 (2004).

42. K. Tsukagoshi, I. Yagi, Y. Aoyagi, Pentacene Nanotransistor With Carbon Nanotube Electrodes. *Appl. Phys. Lett.* **85**, 1021 (2004).

43. D. Wei, Y. Liu, L. Cao, Y. Wang, H. Zhang and G. Yu, Real Time and in Situ Control of the Gap Size of Nanoelectrodes for Molecular Devices. *Nano Lett.* **8**, 1625 (2008).

44. C. Chia-Hao, C. Chao-Hsin, Y. Jung-Yen, Pentacene-Based Thin-Film Transistors With Multiwalled Carbon Nanotube Source And Drain Electrodes. *Appl. Phys. Lett.* **91**, 083502 (2007).

45. K. Horiuchi, T. Kato, S. Hashii, A. Hashimoto, T. Sasaki, N. Aoki and Y. Ochiai. Fabrication Of Nanoscale C[Sub 60] Field-Effect Transistors With Carbon Nanotubes. *Appl. Phys. Lett.* **86**, 153108 (2005).

46. Q. Cao, Z.-T. Zhu, M. G. Lemaitre, M.-G. Xia, M. Shim and J. A. Rogers. Transparent Flexible Organic Thin-Film Transistors That Use Printed Single-Walled Carbon Nanotube Electrodes. *Appl. Phys. Lett.* **88**, 113511 (2006).

47. X. Guo, S. Xiao, M. Myers, Q. Miao, M. L. Steigerwald and C. Nuckolls. Photoresponsive Nanoscale Columnar Transistors, *PNAS* **106**, 691 (2009).

48. Y. Y. Zhang, Y. M. Shi, F. M. Chen, S. G. Mhaisalkar, L. J. Li, B. S. Ong and Y. L. Wu. Poly(3,3 "'-Didodecylquarterthiophene) Field Effect Transistors With Single-Walled Carbon Nanotube Based Source And Drain Electrodes. *Appl. Phys. Lett* **91**, 223512 (2007).

49. J. Liu, J. Zou, L. Zhai, Bottom-up Assembly of Poly(3-hexylthiophene) on Carbon Nanotubes: 2D Building Blocks for Nanoscale Circuits. *Macromol. Rapid Com*. **30**, 1387 (2009).

50. P. G. Collins, M. Hersam, M. Arnold, R. Martel, P. Avouris, Current Saturation and Electrical Breakdown in Multiwalled Carbon Nanotubes. *Phys. Rev. Lett.* **86**, 3128 (2001).

51. C. Thiele, M. Engel, F. Hennrich, M. M. Kappes, K.-P. Johnsen, C. G. Frase, H. v. Lohneysen and R. Krupke. Controlled Fabrication Of Single-Walled Carbon Nanotube Electrodes By Electron-Beam-Induced Oxidation. *Appl. Phys. Lett.* **99**, 173105 (2011).

52. H. Wada, T. Mori, Solution-Processed Carbon Electrodes For Organic Field-Effect Transistors. *Appl. Phys. Lett*. **93**, 213303 (2008).

53. Southard, V. Sangwan, J. Cheng, E. D. Williams, M. S. Fuhrer, Solution-Processed Single Walled Carbon Nanotube Electrodes For Organic Thin-Film Transistors. *Organic Electron*. **10**, 1556 (2009).

54. M. Lefenfeld, G. Blanchet, J. A. Rogers, High-Performance Contacts in Plastic Transistors and Logic Gates That Use Printed Electrodes of DNNSA-PANI Doped with Single-Walled Carbon Nanotubes. *Adv.Mater.* **15**, 1188 (2003).

55. S. L. Hellstrom, R. Z. Jin, R. M. Stoltenberg, Z. Bao, Driving High-Performance n- and p-type Organic Transistors with Carbon Nanotube/Conjugated Polymer Composite Electrodes Patterned Directly from Solution. *Adv.Mater.* **22**, 4204 (2010).

56. J. Chang, C. K. Najeeb, J.-H. Lee, J.-H. Kim, Single-Walled Carbon Nanotubes/Polymer Composite Electrodes Patterned Directly from Solution. *Langmuir* **27**, 7330 (2011).

57. K. Hong, S. Nam, C. Yang, S. H. Kim, D. S. Chung, W. M. Yun and C. E. Park. Solution-Processed Organic Field-Effect Transistors Composed Of Poly(4-Styrene Sulfonate) Wrapped Multiwalled Carbon Nanotube Source/Drain Electrodes. *Org. Electronic.* **10**, 363 (2009).

CHAPTER 3: DEVICE FABRICATION AND EXPERIMENTAL METHODS*

3.1 Introduction

Electronic and optoelectronic devices based on carbon nanotubes and organic semiconductors were fabricated using various micro and nanofabrication tools. I have developed new techniques to fabricate high-performance electronics devices. Organic electronic devices (mainly organic filed effect transistors) were fabricated using aligned array carbon nanotube electrodes (CNTs) thin films, which will be discussed in chapter 4, 5, and 6. In addition, I also fabricate optoelectronic devices where CNT thin films were used as an active channel material, which will be discussed in chapter 7.

Organic field effect transistors (OFETs) based on various organic semiconductors were fabricated using aligned array CNT were materials. To compare the OFET device performance with CNTs aligned array, control OFETs devices were also fabricated with metal electrodes such as Au, Pd. All the transistors are fabricated in the bottom-contact and bottom-gate configuration. The schematic of a typical bottom-contact and bottom-gate configuration OFETs is shown in Figure 3.1. The geometry of the devices such as the channel length (L), channel width (W) is different in the different studies. For example: To demonstrate high-performance organic transistors we fabricated the devices using CNT electrodes with L = 0.7 μm (will discuss in chapter 4), whereas to investigate the charge injection mechanism though the carbon nanotube and organic interface, we fabricate devices with L = 0.2 μm (will discuss in chapter 5). In this

* Portions of this chapter have been published in the following journals: **Mater. Express** *1, 80 (2011);* ***ACS Appl. Mater. Interfaces*** *3, 1180 (2011);* ***Appl. Phys. Lett****. 100, 023301 (2012*); and ***ACS Nano*** *6,* 4993 *(2012).*

chapter, we discuss in details about the electrodes fabrication as well as OFETs fabrication. The room temperature electronics transport properties and device performance are discuss in the chapter 4, and the low temperature electrical transport characterization and charge injection mechanism through the carbon nanotube and organic semiconductor interface are discussed in chapter 5. To improve the better charge injection we also fabricated OFETs by directly growth nanowires on the surface of the carbon nanotube electrodes. We discuss the characterization of the growth of the nanowires on the electrodes and the device performance in the chapter 6.

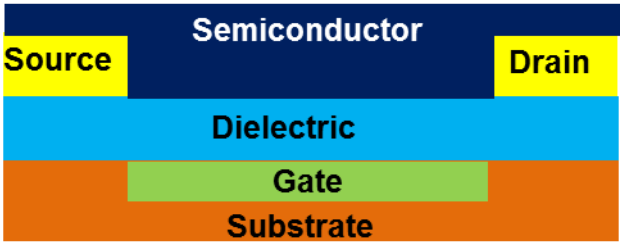

Figure 3.1: Schematic of a bottom-contact and bottom-gate configuration organic field effect transistor (OFETs).

In this chapter, fabrication of OFETs using aligned array CNTs source and drain electrodes will be discussed. Single walled carbon nanotube (SWNT) electrodes are fabricated through dielectrophoretic (DEP) assembly of SWNTs in a dense array and oxidative cutting of the SWNTs array by electron beam lithography (EBL) followed by precise oxygen plasma etching. At first I will discuss the fabrication of the metal electrodes which are used to assemble the carbon nanotube via DEP technique. Then the assembly of the carbon nanotube using DEP method will be discussed. Then the fabrication steps of the aligned array carbon nanotubes

electrodes will be discussed. Finally I will discuss the different fabrication methods of the organic transistors using aligned array carbon Nanotube electrodes.

3.2 Fabrication of Metal Electrodes

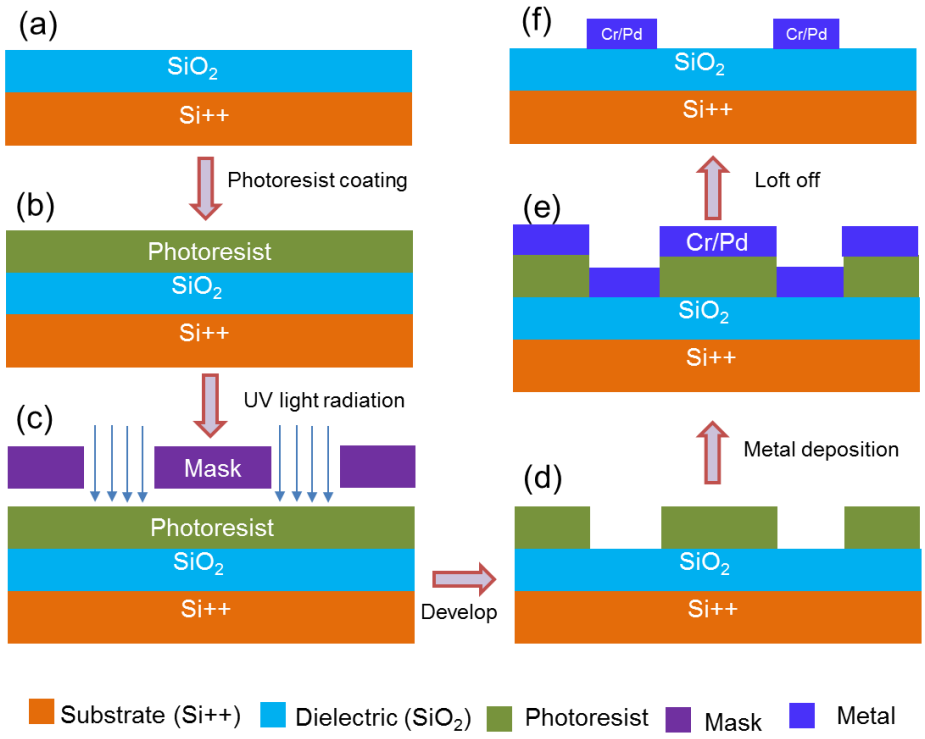

Figure 3.2: Schematic illustration of photolithography process. (a) Heavily doped Si substrates with a thermally grown 250 nm thick SiO_2 layer as a dielectric. (b) Spin-coating photoresist (c) Radiation of the UV light on the photoresistant though the mask. (d) Developing the photoresist. (e) Thermal deposition of metal (f) Lift off (removing the photoresist).

We used heavily doped silicon (Si) wafer with diameter of 3 inch, obtained from Silicon Quest International, used as substrate. The silicon substrate is covered with thermally grown 250 nm thick SiO_2 layer which is used as a dielectric layer with dielectric constant of 3.9. We used both photo-lithography and electron beam lithography (EBL) followed by metal deposition in fabricating the metal electrodes.

3.2.1 Photo Lithography

The schematic steps for the photo lithography are illustrated in Figure 3.2. The contact pad, connecting wires between contact pad and electrode, and alignment markers for secondary EBL are drawn on the Si substrate by photo lithography (Figure 3.3). At first the photoresist (Shipley S1813) is spin coated on the silicon wafer at 300 rms for 30 seconds followed by baking in oven at 110 ^{0}C for 3 minutes. The wafer is then exposed in UV through a Karl Seuss mask aligner for 8.3 seconds. Finally the Si wafer is developed in CD-26 for 25 seconds and rinse with deionize water (DI) water followed by nitrogen blown dry. The optical patterns are checked with optical microscopy.

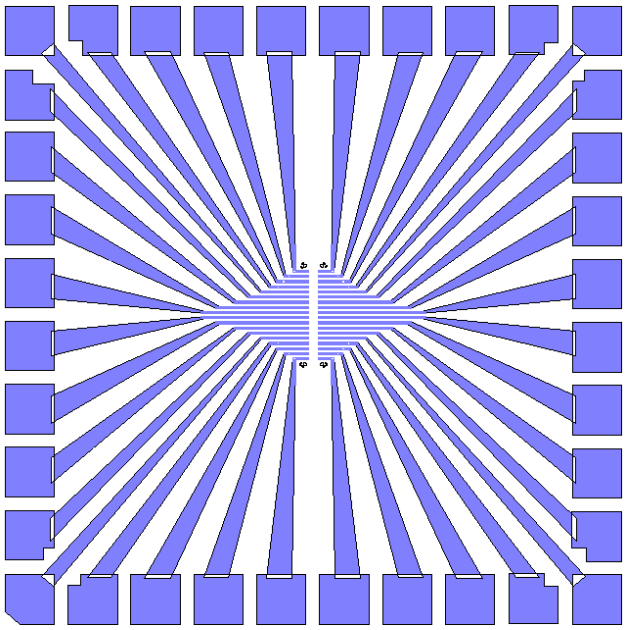

Figure 3.3: Schematic of a chip (without electrode pattern) contains contact pads, connecting leads and alignment markers for EBL.

3.2.2 Metallization

After develop, metal are deposited on the wafer by thermal deposition method. The contact pad, connecting wires between contact pad and electrode, markers for secondary EBL are

fabricated by depositing the chromium (Cr) of 3 nm followed by gold of 45 nm. Cr is used as a sticking layer in between gold and SiO_2 substrate. The thermal deposition is performed at vacuum pressure of less than 5×10^{-6} torr and the deposition rate are 0.1 A^0/s and 0.4 A^0/s for Cr and Au respectively. After metallization, the wafer is kept into PG remover, obtained from Microchem, for 1-2 hours. After that wafer were rinse with acetone, IPA and DI water followed by blown away nitrogen gas. Sometimes it is found that the liftoff was not work properly, that means that if the metal are still remained in the unwanted position on the chips. In this case, the wafer is kept into the acetone for longer time and then perform the sonication about few seconds (say 30s) and rinse with acetone, IPA and DI water and blown away with nitrogen gas.

3.2.3 Electron Beam Lithography (EBL)

The electron beam lithography (EBL) is used to fabricate the small metal electrode pattern (Figure 3.4) . The EBL was done by Zeiss Ultra-55 SEM combined with Nabity pattern generator. At first, PMMA (poly(methylmethacrylate)) is spin coated on the chips at 4000 rpm for 60 seconds, (thickness less than 300 nm) followed by baking at 180^0 C for 15 minutes on a hotplate. The electrode pattern was designed by designed CAD software. The electrode patterns with different channel lengths and channel widths are then defined by opening a window in PMMA resist via EBL writing. In the EBL, 28 KeV is used to expose the resist at current level of 30 PA and area dose of 300 $\mu C/cm^2$. After that the chips are developed by a mixture of MIBK and IPA (1:3) for 70 sec, kept into IPA for 15 sec and blown dry with nitrogen.

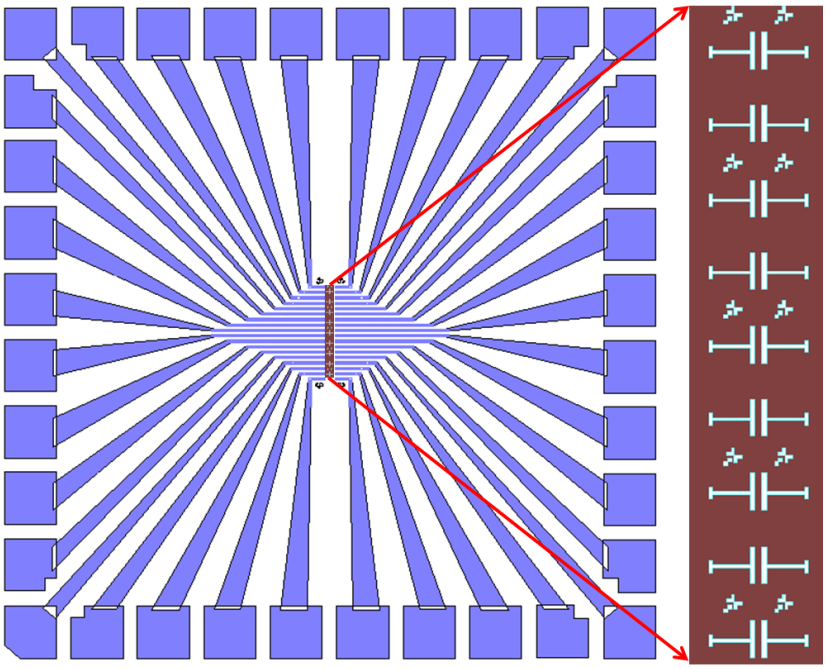

Figure 3.4: Schematic of a chip with electrode pattern (shown in right side). The electrodes are drawn by electron beam lithography (EBL).

Then metal is deposited by either electron beam deposition as well as thermal disposition deposition depending on the metal. Thermal deposition is used to deposit gold, whereas electron beam deposition is used to deposit Pd, Cr, and Ti. The metallization is performed at pressure less than 5×10^{-6} torr with deposition rate of 0.3 A^0/s for Pd and gold, and 0.1 A^0/s for Cr. Before depositing the Pd or gold, Cr with thickness of 3 nm is deposited as a striking layer. Usually the thickness of the deposited metal is 30 nm. After the metallization, the chip/wafer is kept in acetone and rinse with IPA, DI water and blown with nitrogen. The fabricated electrodes patterns are checked with optical microscopy. The small electrode patterns were checked by scanning electron microscopy (SEM) or atomic force microscopy (AFM) imaging. Figure 3.5 shows optical image of the electrode pattern fabricated using EBL.

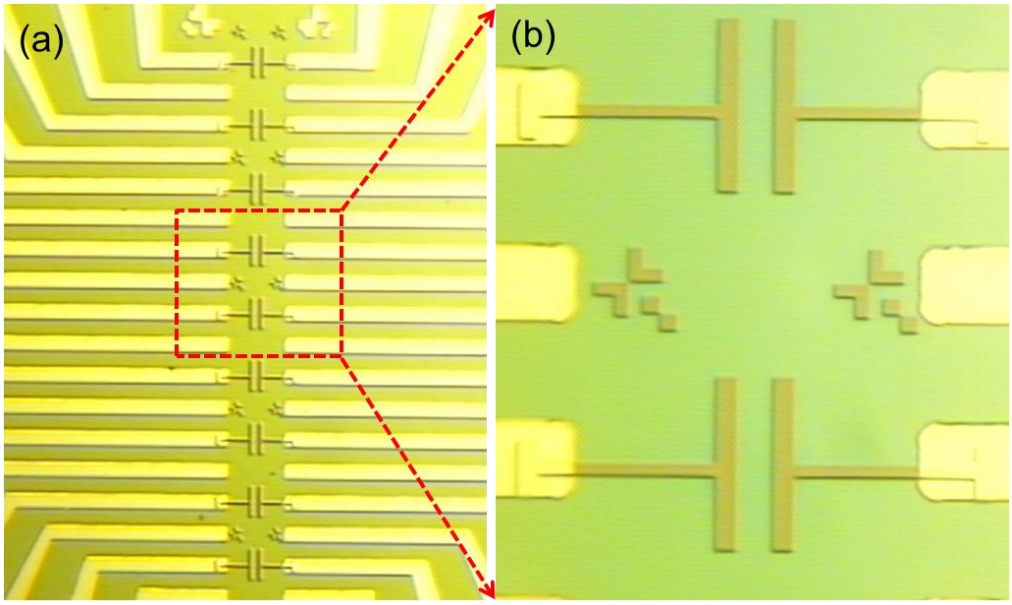

Figure 3.5: (a) Optical microscopy image of the electrodes pattern fabricated by electron beam lithography (EBL) (b) High magnified image. This image shows two electrodes along with markers.

3.3 Fabrication of Carbon Nanotube Aligned Array Electrodes

I have developed a new technique fabrication of aligned array CNT electrodes. The major steps for fabricating of aligned array CNT electrodes are follows and details of these are discussed in the following sections:

(a) Assembly of CNT by Dielectrophoretic

(b) Defined CNT electrode pattern by EBL

(c) Make CNT electrode by plasma etch

3.3.1 Carbon Nanotube Solution

An important step for fabricating of aligned array CNT electrodes is the alignment of CNT with ultra-high density which was done via dielectrophoretic (DEP) technique [1-8]. We used high quality single walled carbon nanotube (SWNT) solution obtained from Brewer Science

to assemble SWNT in a dense array via dielectrophoresis (DEP). The SWNT solution was free from surfactant, catalytic particles and bundles, stable for many months, and contained mostly individual SWNTs [9]. The average diameter of the SWNTs was 1.7 nm and the length of the nanotubes varied from 0.3 to 10 μm with a median value of 1.5 μm as determined from atomic force microscopy (AFM) and scanning electron microscopy (SEM) investigations [10].

3.3.2 Dielectrophoresis Assembly of Carbon Nanotubes

If the charge particles are placed in a uniform or non- uniform electric field, effective dipoles are formed due to redistribution of the free and bound charges. For an isotropic and electrically neutral particles the dipoles are equal and opposite charge. If the uniform electric field is applied to the isotopic and electrically neutral particles the net electrostatic force is zero because the magnitude of the electric forces are equal but opposite directions. When a non-uniform electric field is applied to particles, forces acted on the dipole at the two ends are different, which induces force and torque on the charge particle that cause it to rotation and translation motion along the electric fields (Figure 3.6)[5, 10, 11]. The dielectrophoretic (DEP) method is very efficient for particle with high aspect ratio particle such as carbon nanotube, nanowire. Due to their high aspect ratios and anisotropic shape, these particles act efficiently with electric field, which result in the large diploe moment at the two end of the particle and make large DEP force on the particles.

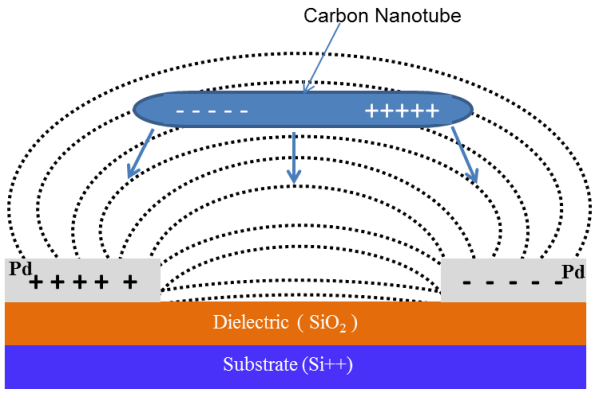

Figure 3.6: A carbon nanotube in the electric field between two charge electrodes.

The relation between the DEP force (F_{DEP}) and created dipole moment (P) in the chage particle due to non-uniform electrical field (E) is given by [5]

$$\vec{F} = (\vec{p}.\nabla)\vec{E} \tag{3.1}$$

Considering carbon nanotube are considered as a long prolate spheroid the induced dipole moment is given by

$$\vec{p} = (1/2)\pi r^2 l \varepsilon_m \,\mathrm{Re}(K)\vec{E} \tag{3.2}$$

where, r and l is the radius and length of the CNTs respectively, absolute permittivity of the medium (solvent), K_f is the Claussius-Mossotti factor which is described by

$$K_f = \frac{\varepsilon_p^* - \varepsilon_m^*}{\varepsilon_m^*},\ \varepsilon_{p,m}^* = \varepsilon_{p,m} - i\frac{\sigma_{p,m}}{\omega}, \tag{3.3}$$

where ε_p is the permittivity of the nanotube, σ is the conductivity, and $\omega = 2\pi f$ is the frequency of the applied ac voltage. Combining 3.1 and 3.2, the time averaged DEP force (F_{DEP}) is [5,12]

$$F_{DEP} \propto \varepsilon_m \,\mathrm{Re}\left[K_f\right]\nabla E_{RMS}^2, \tag{3.4}$$

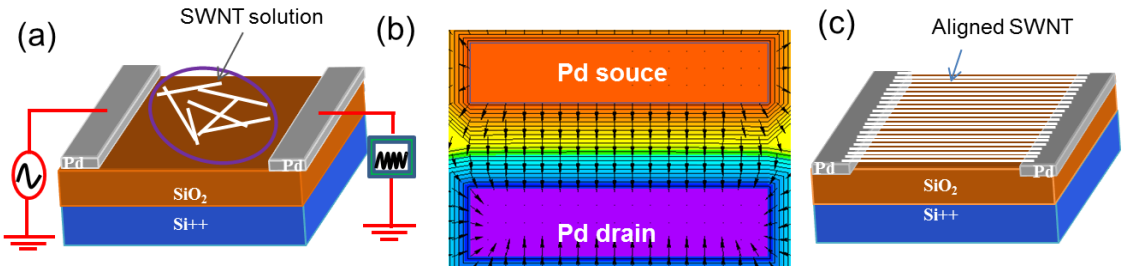

Figure 3.7: (a) Dielectrophoretic (DEP) setup for assembly of CNTs. (b) Simulated electric field around in between Pd source and drain electrodes. (c) Schematic of aligned array CNT via DEP.

DEP is very simple, easy, low-cost and time effective method for assembly the nanoparticles. DEP has been shown to assemble 2*D*, 1*D* and 0*D* nanomaterial's at the selected position of the circuit for device applications [2, 3, 6, 10, 13]. Our group recently shown that CNT can be directly integrated to the prefabricated patterns in a 2D array with controllable alignment and linear density using DEP method. Figure 3.7a show a cartoon of the DEP assembly set up. Palladiums (Pd) of 5 µm x 25 µm were used as a base material to anchor the aligned CNTs. We obtained the CNT aqueous solution from Brewer Science Inc. The solution was highly purified, stable, and surfactant free and it was diluted by six times in DI water for the DEP assembly. A 3 µL drop of the solution was placed on the Pd patterns and an ac voltage of 5 Vp-p at 300 kHz was applied between the Pd patterns for 30 seconds. Because of the non-uniform electric field, the DEP force act on the dipoles at the two end of the nanotube differently which result in a translational motion of the nanotube along the electric field gradient and align the nanotubes in the direction of the electric field lines (Figure 3.7b, 3.7c) [5].

The SWNT assembly by DEP depends on several parameters such as applied voltage (*V*), frequency (*f*) of the applied voltage, concentration of nanotube solution, and time of the applied field. By optimization these parameters such as (V= 5V, f = 300 kHz, and t = 30 s) and by controlling the concentration of the nanotube solution, we can reproducibly control the linear

density of the nanotube in the aligned array. For this study we used parameters (solution concentration 8 µg/ml) to obtain dense array. Figure 3.8 shows a representative SEM image of a part of the assembled SWNTs with an average linear density of ~30 SWNTs/µm. The resistance of this array is ~ 525 Ω and the corresponding sheet resistance is ~2.6 KΩ/sq. In addition, the SWNT aligned arrays are metallic. The low resistance and metallic behavior of the SWNT aligned array make them ideal material for electrodes. The details of the SWNT are characterized by AFM, SEM and electrical transport measurement. (will be discussed in Chapter 4).

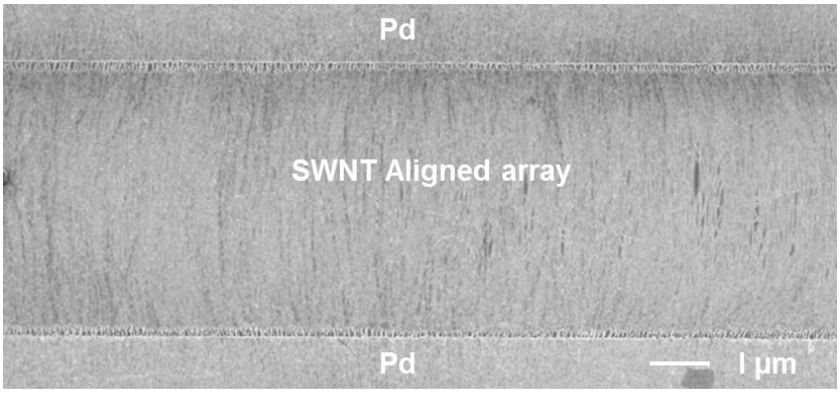

Figure 3.8: Scanning electron microscopy (SEM) of aligned array SWNT array. The linear density of the array is ~ 30 SWNT/µm.

3.3.3 Electron Beam Lithography (EBL) for CNT Electrodes Fabrication

After assembly of SWNTs in a dense array, the electrode patterns are drawn by EBL followed by precise oxidative cutting of the SWNTs array though the open window using plasma etching (Figure 3.9). The process steps of the EBL are similar to what I discussed in earlier about fabrication of the metal electrodes (see section 3.2.4). In order to perform EBL on the CNT array, a layer of PMMA (~thickness 400 nm) was spin coated on the chips containing aligned CNT arrays followed by baking at 180^0 C for 15 minutes on a hotplate (Figure 3.9). The CNT

electrode was then defined by opening a window in PMMA resist via EBL writing and developing in a mixture of MIBK and IPA (Figure 3.10). The channel length and channel width of the electrodes are controlled using the DisignCAD software. We fabricated CNT electrodes of L = 200 nm, 700 nm, 2, 3, 4 µm with W = 25 µm to fabricate devices.

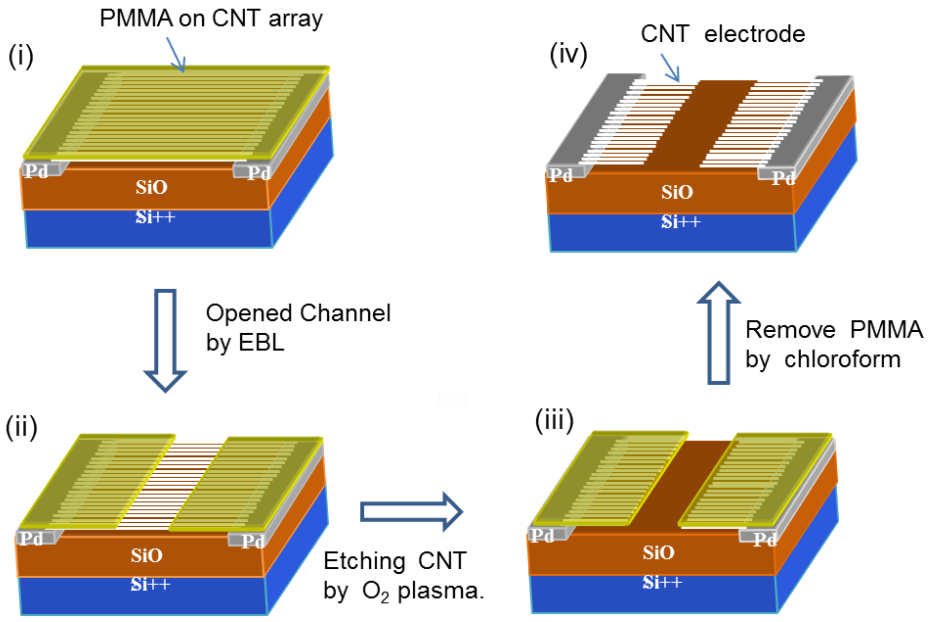

Figure 3.9: Schematic illustration of carbon nanotube electrodes fabrication method from the aligned array. (i) Spin coating PMMA resist, (ii) opening a window on the CNTs array via EBL, (iii) etching the exposed CNTs by oxygen plasma, and finally (iv) remove PMMA by keeping into chloroform for 12 hours.

3.3.4 Plasma Etching

Etching is a method which is used to remove the material from the wafer or any other substrates. The etching process can be classified into mainly in two categories: wet etching and dry etching. To fabricate the CNT electrodes, we used plasma etching which is a purely chemical dry etching technique. During the process of electrode fabrication, I found that the fabrication of the CNT electrodes depends on several parameters such as thickness of PMMA layer, dose

parameter of the EBL, etching time, and gas flow in the plasma etcher chamber. It is found that compared to the other parameters, etching time is dominated and more sensitive. When the devices process with same parameters and then etched with different etching time, I found that device to device varies significantly. For example, when the sample is etched for 30 sec, the CNTs are not etched completely from the desired place (uncoated CNTs by PMMA). On the other hand, when the sample is etched for 90 sec, the CNTs etched from entire place (both coated CNT as well as uncoated CNTs by PMMA). To optimize this process, I made a series of the devices and then used different plasma etching times for different devices and checked with the devices by SEM. Finally, I found that optimize etching time is 80 seconds for fabrication of the CNT electrodes.

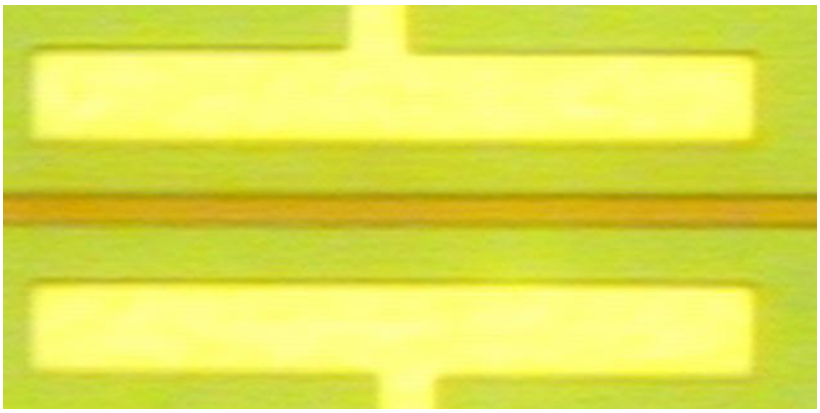

Figure 3.10: Optical microscopy image of CNT electrode fabrication steps (after EBL and develop). This figure shows a straight window is opened by EBL.

After the EBL and development, the chips were then placed in an oxygen plasma chamber and exposed CNT were etched away through the open window (Figure 3.9 and 3.10). A mixture of oxygen (20%) and argon (80%) gas with flow rate of 15-20 CCM was used. Finally, devices were kept into the chloroform for 12 hours and rinse with acetone, IPA, and DI water to

remove the remaining PMMA (Figure 3.9). The SEM of a part of SWNT aligned array electrodes are shown in Figure 3.11. As we see from this Figure shows that SWNT electrodes have well defined channel length and width.

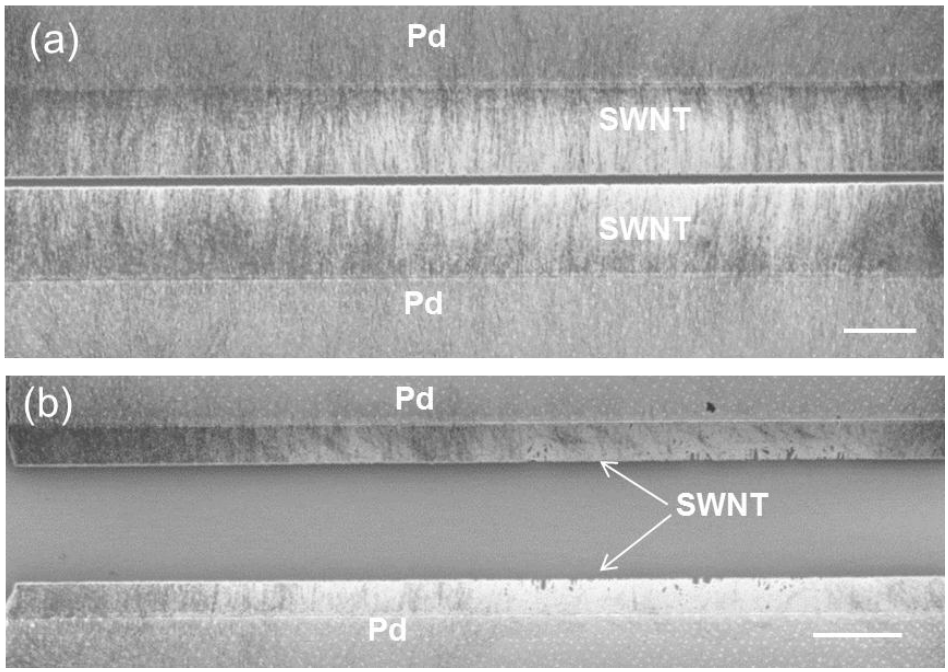

Figure 3.11: Scanning electron microscopy (SEM) image of CNT aligned array electrodes with length of (a) 400 nm, (b) 2 µm. The image shows a part of the whole electrodes. The width of the electrodes is 25 µm.

3.4 Fabrication of Organic Field Effect Transistors

After the CNT electrodes and metal electrode, OFETs were fabricated with various organic semiconductors such pentacene, P3HT, P3HT nanowires. All the OFETs are fabricated in bottom-gated and bottom-contacted configurations. The OFETs are fabricated either thermal vacuum deposition method or solution processed deposition methods depending on the organic semiconductors. To fabricate pentacene OFETs thermal deposition method was used whereas to fabricate the P3HT film and P3HT nanowire OFETs, solution processed method was used.

3.4.1 Vacuum Thermal Deposition Methods

We used vacuum thermal deposition method to deposit the thin film of small molecule organic semiconductors such as pentacene, buckminsterfullerene (or buckyball) (C60). Pentacene power was purchased from Sigma Aldrich. Pentacene was deposited by thermal evaporation onto both aligned array electrodes and Pd electrodes. To pentacene deposition, the pentacene power is loaded into the quartz crucible and kept is metal boat. The pentacene deposition is performed at pressure of 1×10^{-6} pa. The deposition rate was 0.2 A^0/s and thickness of the pentacene thin film was 30 nm. Although deposition of the pentacene is similar to metal deposition, I found that deposition rate in the pentacene is more sensitive than the metal deposition and the grain size of the pentacene thin film varies on the deposition rate. The deposition rate is kept slow to get a smooth thin film with a uniform grain size. The details characterization of pentacene thin films will be discussed in the next chapter. Similar steps are also followed to deposit the buckminsterfullerene (or buckyball) (C60).

3.4.2 Solution Processed Deposition Methods

We used solution process vacuum deposition method (drop costing, direct growth) to deposit the thin film of polymer semiconductors such as P3HT (poly(3-hexylthiophene)), P3HT nanowire, and Poly (2,5-bis(3-tetradecylthiophen-2-yl)thieno[3,2-b] thiophene) (PBTTT).

P3HT powder was purchased from EMD chemicals Inc and was dissolved into 1,2 dichlorobenzene by stirring the solution with magnetic stirrer for 2 hours at 40 ^{0}C. The concentration of the solution was 5 mg/ml. The solution was then filtered with 0.2 μm syringe filter. A thin film of P3HT was then deposited onto chips containing both CNT and Au electrode

by drop cast method inside a N_2 glove box. The fabricated devices were then thermally annealed at 130-140 ^{0}C on a hot plate for 15 minutes to evaporate the solvent.

PBTTT power was dissolved in anisole with a concentration of 0.25 mg/mL at 90 ^{o}C in a glass vial. Bottom contacted PBTTT FETs were fabricated by depositing PBTTT film onto chips containing both CNT and Au electrode by drop cast method inside a N_2 glove box and kept 12 h to evaporate the solvent.

P3HT nanowire OFETs were fabricating by directly growing the nanowire on the surface on the CNTs. The details about this fabrication will be discussed in chapter 6.

3.5 Characterization and Measurement

3.5.1 Process Characterization

The scanning electron microscopy (SEM) images were taken using Zeiss Ultra -55 SEM with an accelerating voltage 1 kV. Tapping mode atomic force microscopy (AFM) images were acquired by Dimension 3100 AFM (Veeco). We performed the Raman spectroscopy using a Renishaw In via Raman microscope. The spectrometer was calibrated with a Si standard using a Si band position at 520.3 cm^{-1}.

3.5.2 Room Temperature Transport Measurement Setup

The electrical transport measurements of the CNT arrays was carried out by DL instruments 1211 current preamplifier and a Keithley 2400 source meter interfaced with LabView program. The OFET characteristics were measured using Hewlett-Packed (HP) 4145B semiconductor parametric analyzer connected to a probe station inside an enclosed glove box system filled with nitrogen gas (Figure 3.12)

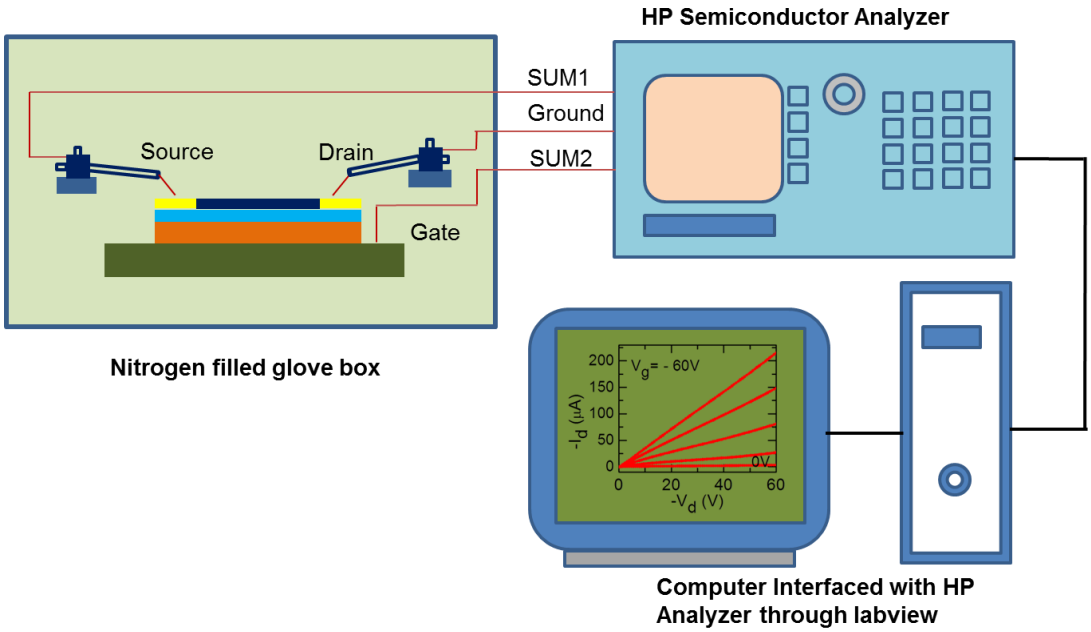

Figure 3.12: Electronics transport measurement setup for device characterization at room temperature.

3.5.3 Low Temperature Transport Measurement Setup

We measured current-voltage (*I-V)* characteristics of our devices at different temperatures in the range of 300 K to 77 K. In order to take reproducible measurements at each temperature, we measured each *I-V* curve at least two times, and waited for 15 minutes in successive measurements. The temperature was controlled with a lakeshore temperature controller and we waited at least 10 minutes to stabilize the temperature before taking data.

3.6 References

1. S. Shekhar, P. Stokes, S. I. Khondaker, Ultrahigh Density Alignment of Carbon Nanotube Arrays by Dielectrophoresis. *ACS Nano* **5**, 1739 (2011).

2. P. Stokes, E. Silbar, Y. M. Zayas, S. I. Khondaker, Solution Processed Large Area Field Effect Transistors from Dielectrophoreticly Aligned Arrays of Aarbon Nanotubes. *Appl. Phys. Lett.* **94**, 113104 (2009).

3. P. Stokes, S. I. Khondaker, Evaluating Defects in Solution-Processed Carbon Nanotube Devices via Low-Temperature Transport Spectroscopy. *ACS Nano* **4**, 2659 (2010).

4. R. Krupke, F. Hennrich, M. M. Kappes, H. v. Lohneysen, Surface Conductance Induced Dielectrophoresis of Semiconducting Single-Walled Carbon Nanotubes. *Nano Lett.* **4**, 1395 (2004).

5. M. Dimaki, P. Boggild, Dielectrophoresis of Carbon Nanotubes Using Microelectrodes: A Numerical Study. *Nanotechnology* **15**, 1095 (2004).

6. S. I. Khondaker, Fabrication of nanoscale device using individual colloidal gold nanoparticles. *IEE Proceedings-Circuits Devices and Systems* **151**, 457 (2004).

7. M. Dimaki, P. Boggild, Dielectrophoresis of carbon nanotubes using microelectrodes: a numerical study. *Nanotechnology* **15**, 1095 (2004).

8. R. Krupke, F. Hennrich, M. M. Kappes, H. V. Lohneysen, Surface Conductance Induced Dielectrophoresis of Semiconducting Single-walled Carbon Nanotubes. *Nano Lett.* **4**, 1395 (2004).

9. Brewer Science Inc. http://www.brewerscience.com/carbon-nanotube.

10. S. Shekhar, P. Stokes, S. I. Khondaker, Ultrahigh Density Alignment of Carbon Nanotube Arrays by Dielectrophoresis. *ACS Nano* **5**, 1739 (2011).

11. M. Duchamp, K. Lee, B. Dwir, J. W. Seo, E. Kapon, L.Forró, and A. Magrez, Controlled Positioning of Carbon Nanotubes by Dielectrophoresis: Insights into the Solvent and Substrate Role. *ACS Nano* **4**, 279 (2010).

12. B. K. Sarker, S. Shekhar, S. I. Khondaker, Semiconducting Enriched Carbon Nanotube Aligned Arrays of Tunable Density and Their Electrical Transport Properties. *ACS Nano* **5**, 6297 (2011).

13. D. Joung, A. Chunder, L. Zhai, S. I. Khondaker, High yield fabrication of chemically reduced graphene oxide field effect transistors by dielectrophoresis. *Nanotechnology* **21**, 165202 (2010).

14. J. Moscatello, V. Kayastha, B. Ulmen, A. Pandey, S. Wu, A. Singh and Y. K. Yap.Surfactant-Free Dielectrophoretic Deposition Of Multi-Walled Carbon Nanotubes With Tunable Deposition Density. *Carbon* **48**, 3559 (2010).

CHAPTER 4: DEVICE PERFORMANCE OF ORGANIC FIELD EFFECT TRANSISTORS WITH CARBON NANOTUBE ELECTRODES*

4.1 Introduction

Organic field effect transistor (OFET) has attracted tremendous attention due to their low-cost fabrication process and prospect for large area, flexible, transparent electronic device applications [1-2]. The performance of the OFET device is not only depends on the molecular properties of the organic semiconducting material, but also it is extremely sensitive to the organic material-metal electrode interface [3-5]. The metals such as gold, palladium are widely used as source and drain (S/D) electrodes for OFET device [3]. When metal electrodes are contacted with organic semiconducting material, in addition to the Schottky barrier, dipole barrier is formed at the interface [6,7]. As a result, the contact resistance between the metal and semiconductor become very large and charge transport is often limited by the interface [1-5, 7-9] . In addition, metal electrodes are not solution processed and they are not flexible. However, flexible electrodes are required in the application of flexible electronics. In order to overcome the problems of high contact resistance, dipole formation and non-flexibility of metal electrodes, carbon nanotube (CNT) has been considered as a promising electrode materials for organic electronics due to their highly conducting, flexible, and one-dimensional structure [10-19]. In the previous chapter, we demonstrated a novel, controlled and highly reproducible approach for the fabrication of CNT aligned array electrode. The ultra-high density CNTs were aligned with a very high linear density (~30 CNTs/μm) from high quality CNT aqueous solution by

* Portions of this chapter have been published in the following journals: **Mater. Express** *1, 80 (2011);* ***ACS Appl. Mater. Interfaces*** *3, 1180 (2011);* ***Appl. Phys. Lett****. 100, 023301 (2012*); and ***ACS Nano*** *6,* 4993 *(2012).*

dielectrophoresis (DEP) techniques. The CNT source and drain electrodes are fabricated with electron beam lithography (EBL) followed by etching CNTs with oxygen plasma.

In this chapter, at first we discuss the characterization of the CNT assembly as well as CNT aligned array electrodes. Then we demonstrate fabrication of high-performance OFETs using aligned array CNT electrodes and investigate the detailed electronic transport properties of the fabricated devices. A number of promising organic semiconductors, such as poly(3-hexylthiophene) (P3HT) and pentacene, are used to fabricate OFETs. To examine the functionality and efficiency of the CNT array electrodes, the performance of the CNT contact OFETs are compared with the performance of the metal electrode contact OFETs. The OFETs with CNT electrodes show a remarkable enhancement in the device performance such as high mobility, high current on-off ratio, higher cutoff frequency, absence of short channel effect and better charge carrier injection than those OFETs with metal electrodes.

4.2 Characterization of CNT Assembly and CNT Electrodes

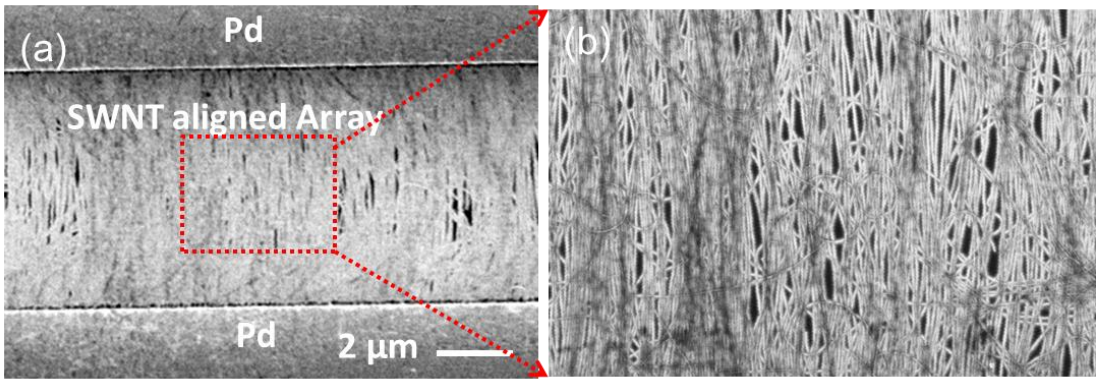

Figure 4.1: The scanning electron microscopy (SEM) image of a typical aligned array single walled carbon Nanotubes (SWNTs), assembled by dielectrophoresis (DEP).(b) High magnified image of the SWNT assembly.

Figure 4.1 shows a representative SEM image of a densely aligned array of CNT assembled via DEP and the high magnified SEM image is shown in inset of this Figure 4.1 b. The linear density of the SWNT in the electrodes is about 30 SWNTs/μm. The resistance of this array was ~ 525 Ω (Figure 2b) with a corresponding resistivity of ~2.5 kΩ/sq. We have recently shown that by controlling the concentration of the CNT in the solution, we can reproducibly control the linear density of the CNT in the array from 1 CNT/μm to 30 CNT/μm [20] .This study also showed that at low densities, almost all of the nanotubes are well aligned and are parallel to each other whereas, at higher density, about 90% are aligned within $\pm 10^0$ of the longitudinal axis [20]. In this experiment, we only used densely packed aligned array so that the resistance of the array is low (<1 KΩ). In addition we have also verified the metallic nature of the array by measuring current-gate voltage characteristics (Figure 4.2). This Figure clearly show that current is independent of the gate voltage, indicating that CNT array act as a metallic sheet. The low resistance and metallic behavior of the array makes them ideal material for OFET electrodes.

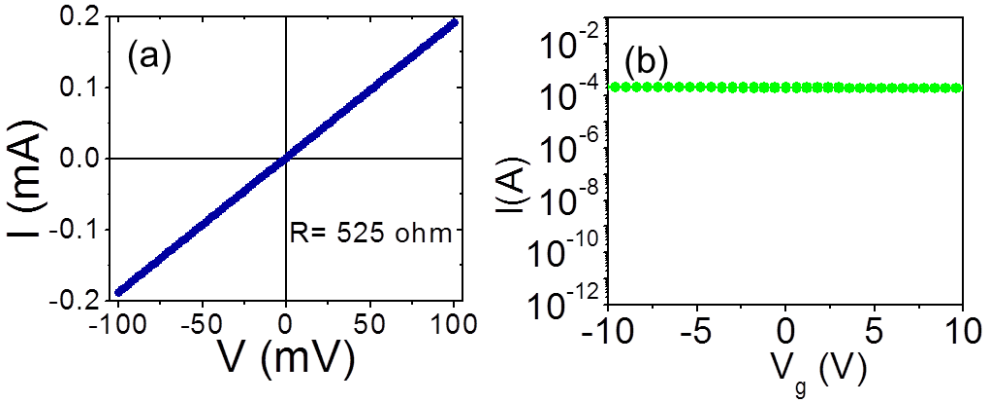

Figure 4.2: (a) Current (*I*)-voltage (*V*), and (b) Current-gate voltage (V_g) characteristics at V =100 mV of typical aligned array SWNT.

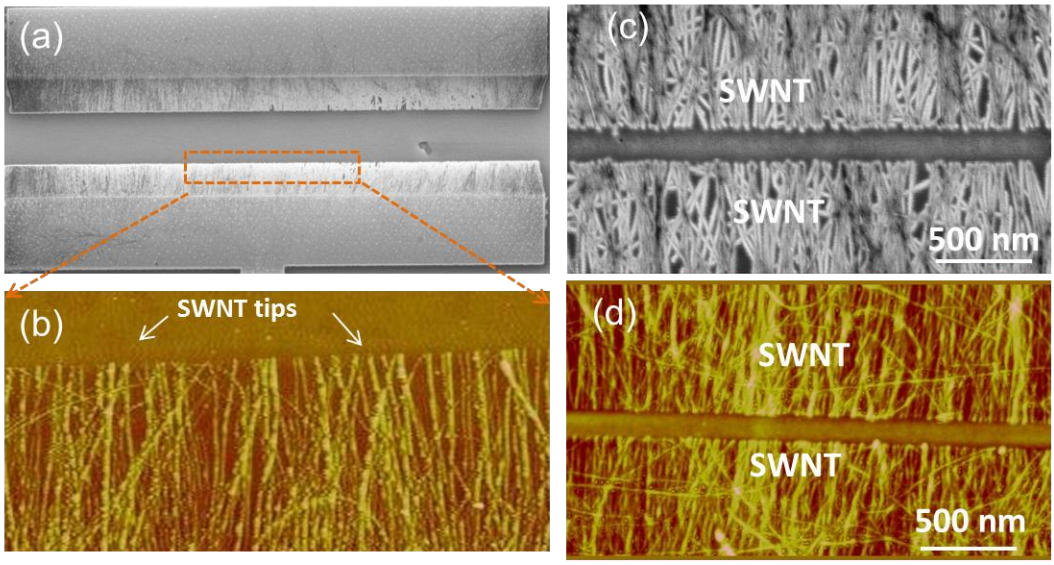

Figure 4.3: (a) SEM image of a part of the SWNT aligned array electrodes. (b) High magnification AFM image of CNT tips in the CNT electrodes. (c) SEM image of a part of aligned array SWNT electrodes.

Figure 4.3 shows a SEM image of a part of CNT electrodes with well-defined channel length and width. Figure 4.3a shows of an electrodes with channel length L = 2 µm, whereas Figure 4.3 shows of a electrodes with channel length L = 200 nm. The linear density of the CNT in the electrodes is about 30 CNTs/µm. The rms surface roughness of the CNT arrays in the electrodes is about 1.8 nm. The images also show no residual nanotubes in the channel which was further confirmed by measuring current-voltage characteristics of the electrodes before depositing pentacene, which showed negligible current (sub pA noise current, not shown here).

In the electrodes, the nanotubes are well aligned where individual nanotubes are closely packed with parallel and open-ended tips, as shown in the atomic force microcopy (AFM) image (Figure 4.3b). One fundamental advantage of our electrode pattern is that all the tips of CNTs in the electrodes are parallel and open ended; because in our experiment, electrodes are formed though oxidative cutting of each CNTs in the middle by oxygen plasma etching. This is in

distinct contrast to the previous reports of CNT electrode fabrication. The parallel and open-ended tips are advantageous because parallel tips can enhance tunneling of the charge carriers at nanotube electrodes and pentacene interface due to electric field enhancement at these tips. In addition, open-ended tips provide higher field emission than the close-end nanotube tips.

4.3 Poly(3-hexylthiophene)(P3HT) Transistor with CNT Aligned Array Electrodes

4.3.1 Fabrication of P3HT Transistors

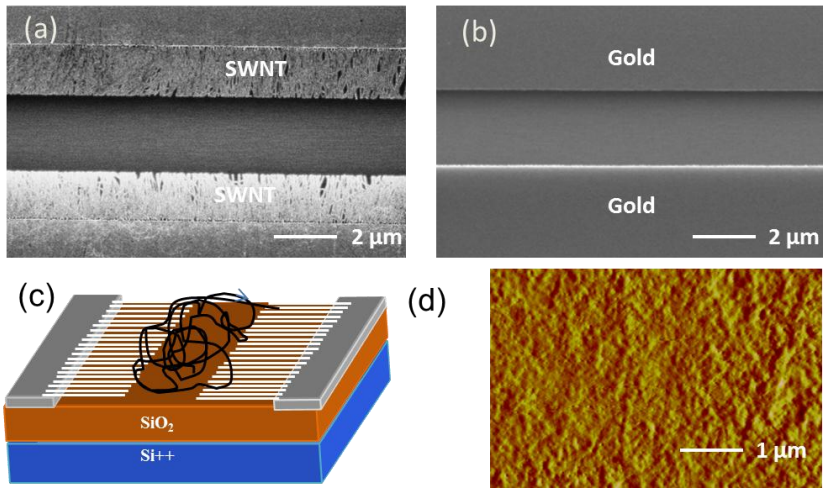

Figure 4.4: The representative SEM images of the (c) CNT electrode and (d) gold electrode. The electrode geometry of the both CNT and gold electrodes are the same. (c) Schematic diagram of P3HT OFET with aligned array CNT electrodes. (d) AFM image of deposited P3HT thin film.

We fabricated P3HT OFET using aligned array CNT electrodes with channel length of 2 um and width 25 um (Figure 4.4a) To investigate the performance of the OFET with CNT electrodes, control devices were also fabricated using gold electrodes with the similar geometry of the CNT electrodes (Figure 4.4b). The schematic diagram of the P3HT OFET with CNT electrodes is shown in Figure 4.4c. A thin film of P3HT was then deposited onto chips containing both CNT and Au electrode by drop cast method inside a N_2 glove box. The fabricated devices were then thermally annealed at 130-140 ^{0}C on a hot plate for 15 minutes to

evaporate the solvent. The atomic force microscopy (AFM) image of the P3HT thin film is shown is Figure 4.4d. The details of the P3HT OFET fabrication are discussed in chapter 3. The OFET characteristics were measured using Hewlett-Packed (HP) 4145B semiconductor parametric analyzer connected to a probe station inside an enclosed glove box system filled with nitrogen gas.

4.3.2 Transport Properties of P3HT Transistors

As an example of the effectiveness of our aligned CNT array electrode, we fabricated P3HT thin film OFET using CNT array electrodes (CNT/OFET). For control experiment, OFET with gold electrodes was also fabricated (Au/OFET). The SEM of the gold electrode is shown in Figure 4.4b. The source-drain current (I_d) versus source-drain voltage (V_d) characteristics (output curve) of the CNT/ OFET and Au/OFET were measured at different gate voltages (V_g) and are shown in Figure 4.5a and 4.5b respectively.

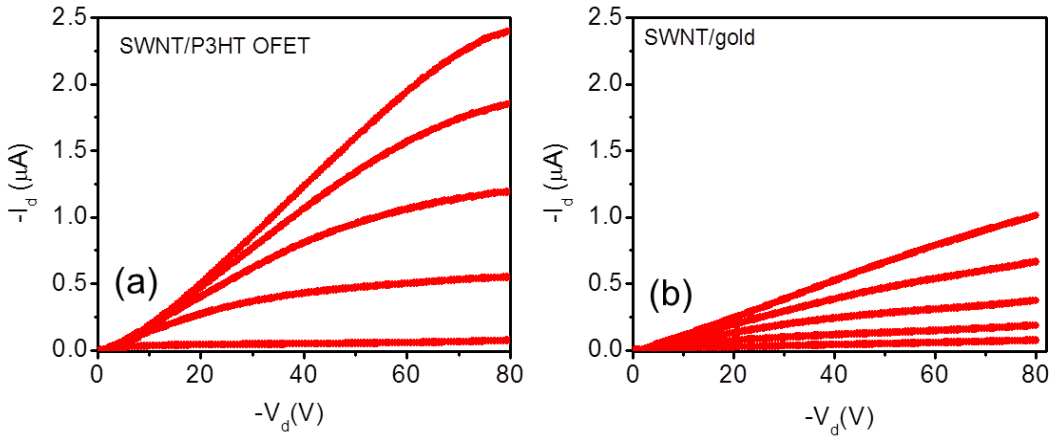

Figure 4.5: Output characteristics (I_d versus V_d at various Vg) of P3HT film OFET with (a) CNT align array electrodes and (b) gold electrode at V_g = 0, -20,-40, -60 and -80V. Both OFETs has L= 2 μm and W = 25 μm. Both curves are plotted in the same scale to see the clear difference in output current value of these two OFETs.

Compared to the output curve of Au/OFET device, output curve of CNT/OFET device shows better drain current modulation with V_g. In addition, saturation current $I_{d,sat}$ (2.5 μA) of CNT/OFET device is higher than the saturation current (0.9 μA) of the Au/OFET device at V_g= -80 V. In low V_{ds} region, the curve shows a sub-linear onset due to contact resistance, hallmark of short channel OFETs. Since the channel length of our device is only 2 μm, the nonlinear onset behavior appears in our device. Similar nonlinear behavior has also been observed for the OFETs fabricated with RGO electrode as well as OFET with metal electrode[21].

Transfer characteristics of the CNT/OFET and Au/OFET device are shown in left axis in Figure 4.6a and 4.6b respectively ,where I_d is plotted as a function of V_g with a fixed V_d = -60V. The $\sqrt{I_d}$ versus V_g plots are shown right axis of Figure 4.6a and 4.6b, from where threshold voltage (V_T) was calculated to be 0 V and 10 V for CNT/OFET and Au/OFET device respectively. From here, the saturation mobility (μ_{sat}) and linear mobility (μ_{lin}) of the devices were calculated using following standard formula

$$\mu_{sat}=I_{d,sat}(2L/WC_i)(1/(V_g-V_T)^2) \quad (4.1)$$

$$\mu_{lin}= (L/WC_iV_d)(dI_d/dV_g) \quad (4.2)$$

where C_i is the capacitance per unit area of the gate insulator (13.8 nF/cm^2) [21]. The calculated μ_{lin} and μ_{sat} of CNT/OFET device are 0.004 and 0.005 cm^2/Vs respectively. On the other hand, both μ_{lin} and μ_{sat} of Au/OFET device are 0.001 cm^2/Vs, five times smaller than that of CNT/OFET. The current on/off ratio of CNT/OFET device is 5×10^3, whereas I_{on}/I_{off} of Au/OFET is only 9×10^1. The current on-off ratio of CNT/OFET device is more than two order magnitude higher than the on-off ratio of Au/OFET. From these results, we conclude that OFET with aligned CNT array electrode shows superior device performance including higher mobility, higher on-current and higher current on-off ratio than OFET with gold electrodes.

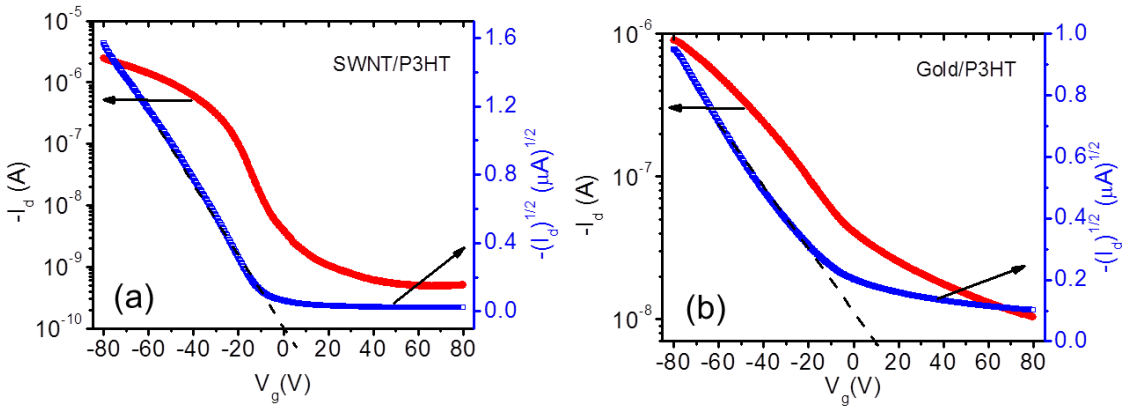

Figure 4.6: Transfer characteristics (I_d versus V_g) at V_d = -60V (left axis) and $\sqrt{I_d}$ (right axis) of the P3HT film OFET with (a) CNT aligned array electrode and (b) gold electrode

The reasons for better device performance with aligned array CNT electrode compared to Au electrode are as follows: The work function of gold (5.1 eV) and CNT (5.0 eV) are very close, and according to Schottky-Mott model, good contact of P3HT is expected with both gold and CNT [1, 6, 17]. However, when gold electrode is contacted with organic material, the dipoles barriers are formed at the interface [6,7] and charger carrier transport though the interface is limited by this barrier. In addition, the gold contact exhibits 2D electrostatic effect and it has little influence on the tunneling of the charge carrier though the Au/semiconductor interface. On the other hand, the individual CNTs in the CNT array electrodes having a form factor which enhance the electric field at the apex of nanotube that assists the tunneling the charge carrier though the contact barrier [15, 16, 19]. Moreover, the strong π-π bonding between CNT and organic material makes strong interfacial contact and reduces the barrier height [14, 16]. Therefore, the possible reasons for improved device performance using CNT electrode over gold electrode device are due to absence of the dipole barrier, CNT geometry induced electric field and strong π-π bonding between CNT and organic material.

In this section, I showed the fabrication of OFET using both CNT array electrode and gold electrode in order to examine the functionality of the CNT array electrodes. It was found that OFET device with CNT electrode has shown better performance than the device with gold electrode. The improved device performance using CNT array electrode is attributed to absence of dipoles formation, strong bonding interaction between CNT/organic material and the geometry structure of aligned array CNT electrode.

4.4 Pentacene Transistors with CNT Aligned Array Electrodes

For many applications of organic electronic such as integrated circuits, OFETs should operate at high switching speed with a high on-current [22, 23]. The switching speed of OFETs is proportional to the mobility (μ) and inversely proportional to the square of the channel length (L) [24, 25]. In addition, the on-current is also inversely proportional to the channel length. Therefore, in order to raise the switching speed and on-current, OFETs with small channel length (short channel OFETs) and high mobility are required. Up until now, short channel OFETs were fabricated using metal electrodes (mostly gold) where interfacial barriers such as Schottky barrier and dipole barrier are known to create major bottleneck for charge carrier injection [6, 7]. Both the theoretical and experimental studies reveal that when the channel length is reduced, the contact resistance at metal-organic semiconductor interface becomes very high compared to the resistance of the organic semiconductors in the channel[8],[8] leading to a significant reduction in mobility. Moreover, these devices show a lower current on-off ratio due to a high off current and displays parabolic behavior in the output current, known as short channel effect.[8, 25] Therefore, achieving high performance short channel OFETs still remains a significant challenge. One way to overcome the challenges of short channel devices is to search for

alternative electrode materials with more efficient charge injection into organic materials. In the last section I have shown that due to its unique electronic properties and strong π-π interaction with organic semiconductors [14] carbon nanotubes electrode can overcome the limitations of metal electrodes in fabricating high performance short channel devices.

In this section, we discuss the high-performance pentacene OFETs using aligned array carbon nanotubes electrode with L = 0.7 μm. The electronic transport measurement of 10 such devices show that the maximum mobility is 0.65 cm^2/Vs with an average of 0.25 cm^2/Vs, and the current on-off ratio is in the range of 2.9×10^3 to 1.7×10^6. The maximum mobility and on-off ratio reported here are the highest reported for the short channel pentacene OFETs. We also show that the calculated maximum cutoff frequency (f_c) of the device is 211 MHz with an average of 81.5 MHz. The maximum f_c of our device is one order of magnitude higher than the f_c of control and reported devices fabricated using gold electrodes. We attribute the high performance of our devices using nanotubes electrodes to improve charge injection and better interfacial contacts between pentacene and the aligned array carbon nanotube electrodes.

4.4.1 Fabrication of Pentacene Transistors

To fabricate penance OFETs, we used CNT electrodes with channel length 700 um and channel with of 25 μm. Here short channel CNT electrodes were used deliberately because we discussed that to fabricate high-switching speed OFETs, the device channel length should be small. The scanning electron microscopy (SEM) image of a part of the SWNT aligned array electrodes is shown in Figure 4.7.

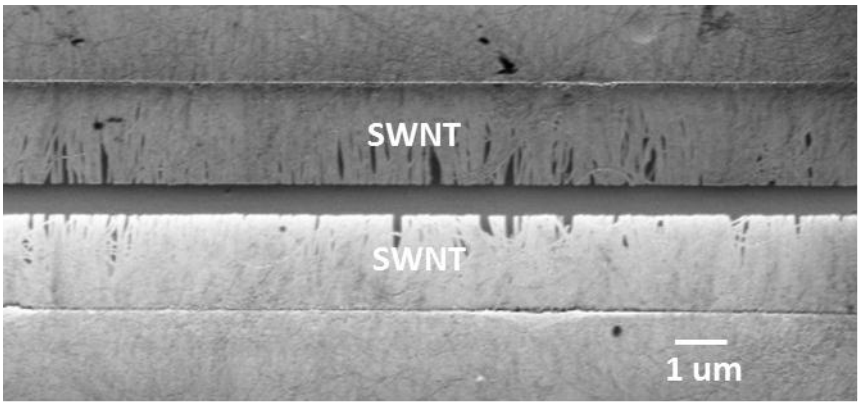

Figure 4.7: (a) SEM image of a part of the CNT aligned array electrodes with channel length of 700 nm.

In order to compare the performance of our SWNT aligned array electrodes, gold electrodes of similar geometry were fabricated for control experiments. The pentacene thin film (30 nm) was thermally evaporated on top of the SWNT electrodes and gold electrodes. Figure 4.8 is a part of the AFM image of the deposited pentacene thin film, showing a nearly uniform gain size and morphology throughout.

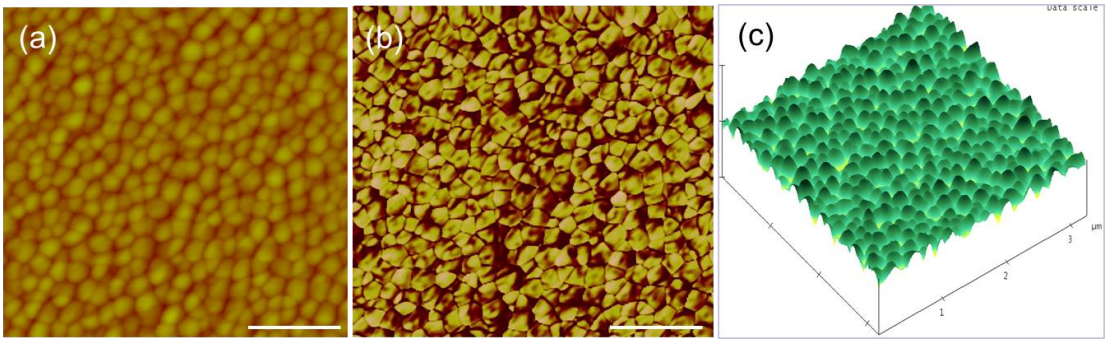

Figure 4.8: AFM image of deposited pentacene thin film. (a) height image (b) phase image and (c) surface image. The scale bars in Figures (a), (b), and (c) are 1 μm.

We did not observe any noticeable difference between the morphologies of the pentacene films deposited on SWNT and gold electrodes (Figure 4.9). The OFET characteristics were

measured using Hewlett-Packed (HP) 4145B semiconductor parametric analyzer connected to a probe station inside an enclosed glove box system with nitrogen gas flow.

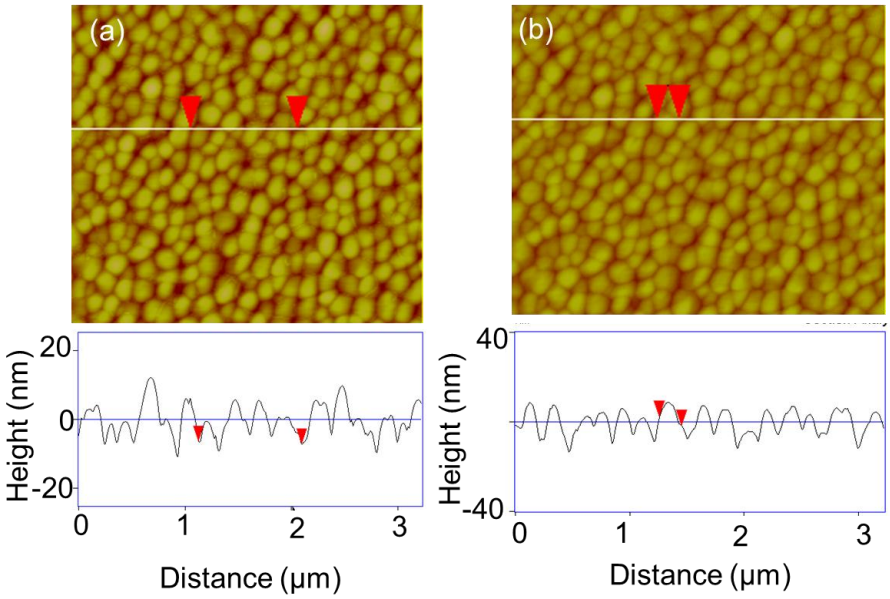

Figure 4.9: (a) AFM height image of deposited pentacene thin film. The morphology of the film (a) rms surface roughness is ~ 3-4 nm (b) grain size is 100-150 nm.

4.4.2 Short Channel Pentacene Transistors

The electronic transport characteristics of a typical pentacene OFET using aligned SWNT array electrodes with high mobility and high current on-off ratio are shown in Figure 4.10a and 4.10b respectively. The transfer characteristics (Figure 4.10a) show a well modulation of drain current (I_d) with gate voltage (V_g) with a current on-off ratio of 1.7×10^6.The linear mobility (μ) of the device is 0.25 cm^2/Vs, calculated using standard formula $\mu = (L/WC_iV_d)(dI_d/dV_g)$ where, V_d is the source-drain voltage, C_i is the capacitance per unit area of the gate insulator (13.8 nF/cm^2). The output characteristics (I_d-V_d curves) of the same device (Figure 4.10b) displays a high output current of ~ 215 μA at V_g = - 60 V and V_d = - 60 V. Although a high output current in

the short channel OFETs is expected, well gate modulation with high on-off ratio is not typically observed in short channel OFETs using conventional metal electrodes. The linear behavior of the output curves at low bias is consistent with ideal ohmic contact, suggesting a good interfacial contact between the aligned nanotube electrode and pentacene. Out of the 10 pentacene/SWNT OFET devices that we have measured, we found that the motilities are in the range of 0.09 to 0.65 cm^2/Vs with an average of 0.25±0.16 cm^2/Vs and the on-off ratios of the most of the devices are greater than 10^4 with a maximum of 1.7×10^6. The maximum mobility of 0.65 cm^2/Vs and maximum on-off ratio of 1.7×10^6 of our short channel devices using SWNT aligned array electrodes are the highest reported for any submicron pentacene OFETs [25, 26].

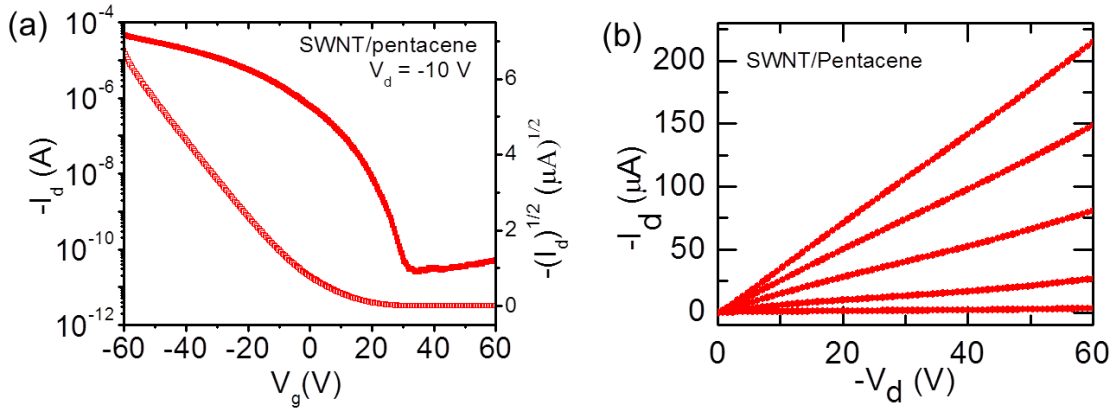

Figure 4.10: (a) Transfer characteristics (I_d versus V_g) at V_d = -10 V (left axis) and $\sqrt{I_d}$ (right axis) of typical OFETs using SWNT aligned array electrodes and. Output characteristics (I_d versus V_d) at V_g = 0 to -60 V with -15 steps of the same device.

The performance of our OFETs using SWNT aligned array electrodes are also better compared to our control OFETs using gold electrodes with identical device geometry, which were fabricated and measured under same experimental conditions. The transfer and output characteristics of a typical pentacene/gold device are shown in Figure 4.11a and 4.11b

respectively. The mobility, on-off ratio, and output current of this device are 0.03 cm^2/Vs, 1.3×10^4 and 17 μA (at V_g = -60V and V_d = -60V) respectively. The mobility of the measured 10 pentacene/gold devices is in the range of 5×10^{-3} to 0.05 cm^2/Vs with an average of 0.02±0.01 cm^2/Vs, and the on-off is in the range of 5.8×10^2 to 2.1×10^4. Therefore, the maximum mobility and maximum on-off ratio of the devices using nanotube electrodes are ~13 times and ~100 times higher than that of devices using gold electrodes, respectively. In addition, the output curves of the OFETs using gold electrodes show a non-linear behavior at both low and high bias, a common phenomenon observed in short channel OFETs with metal electrodes and high gate thickness [23, 24].

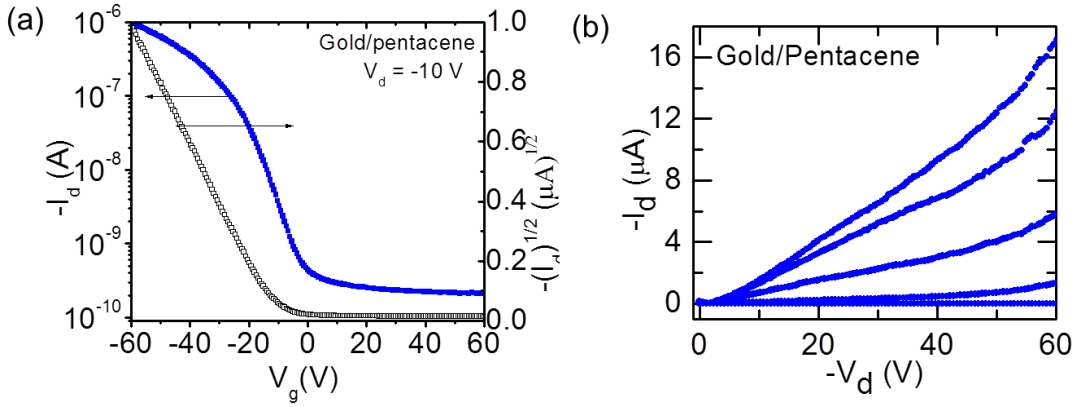

Figure 4.11: (a) Transfer characteristics (I_d versus V_g) at V_d = -10 V (left axis) and $\sqrt{I_d}$ (right axis) of typical OFETs using gold electrodes and. Output characteristics (I_d versus V_d) at V_g = 0 to -60 V with -15 steps of the same device.

In contrast, although our pentacene/SWNT OFETs fabricated using a small channel length (0.7 μm) and comparable oxide thickness (0.25 μm), they show linear behavior of the output curves and provide a higher mobility along with higher on-off ratio (Figure 4.10), suggesting that the performance is not limited by short channel effect. As the short channel effect is a major

bottleneck in reducing the device size for high performance OFETs, [5, 8, 23] the improvement of our short channel devices using SWNT electrodes is very significant. The performance of the OFETs mainly depends on the film morphology of the channel materials and the contact barriers between the films and electrodes. As the both the film morphologies of the pentacene/SWNT and pentacene/gold devices are the same, the improved performance of pentacene/SWNT devices are mainly arose from the improved contact.

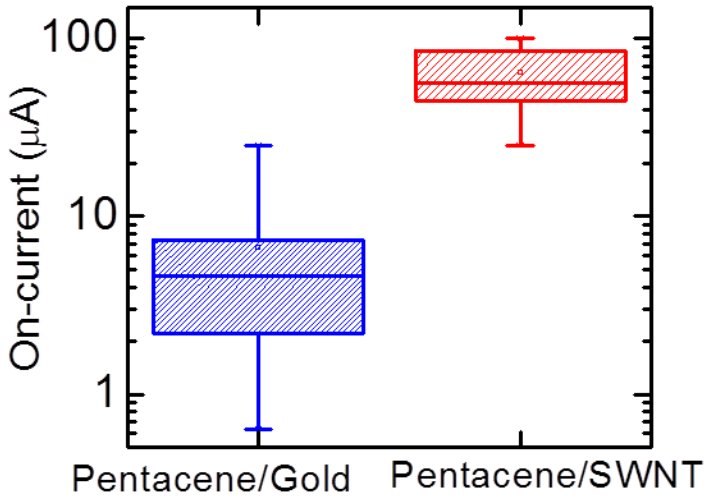

Figure 4.12: Box plot of the on-current of 10 pentacene/SWNT (top red box) and 10 pentacene/gold devices (bottom blue box).

In order to demonstrate improved charge injection of the SWNT aligned array electrodes, we show box plots of on-current of all measured pentacene/SWNT devices (red) along with all pentacene/gold devices (blue) in Figure 4.12. The on-current is calculated from the transfer curve at V_g= -60 V and V_d = -10V. The average on-current of pentacene/SWNT devices is 65 μA with a maximum of 100 μA, whereas the average on-current of pentacene/gold device is only 6.6 μA with a maximum of 11 μA. Therefore, the both average and the maximum on-current of the

pentacene/SWNT devices are ~10 times higher than that of pentacene/gold devices. This clearly demonstrates that the charge injection from densely aligned SWNT array electrodes with open ended tips is much better than that of the gold electrodes.

4.4.3 High-Frequency Pentacene Transistors

The short channel OFETs with high mobility can provide improved switching speed, which is required for many practical applications such as display electronics. The unity gain cutoff frequency of the transistors in the linear region is described as

$$f_c = (\mu V_d/2\pi L^2)[C_i WL/(C_i WL+C_p) \quad (4.3)$$

where C_i is the gate capacitance per unit area and C_P is the parasitic capacitance. Considering $C_p << C_i WL$, [5, 27] we calculated f_c of our devices and a plot of the f_c versus on-off ratio is shown in Figure 4.13. This plot shows that compared to the pentacene/gold devices (blue circles), most of the pentacene/SWNT devices (red stars) have a higher f_c along with a higher on-off ratio. The average f_c of the pentacene/SWNT device is 81.5±54.4 MHz with a maximum of 211 MHz, On the other hand, average f_c of the pentacene/gold devices is only 6.5±4.5 MHz with a maximum of 16.5 MHz. While the f_c of the pentacene/gold devices is similar to the other reported f_c the OFETs using gold electrodes,[28] the maximum f_c = 211 MHz for SWNT/pentacene OFET reported here is one order magnitude higher than the previous best reported f_c of the OFETs (Table 4.1).[4, 24, 28] Recently, it was shown that calculated value of f_c is similar to the measured value [28] justifying the assumption of negligible C_p in our devices. Nevertheless, if we consider C_p is comparable $C_i WL$ in our devices, the maximum f_c of the SWNT/pentacene will still be more than 100 MHz, which is still higher than f_c for any OFETs using metal electrodes.

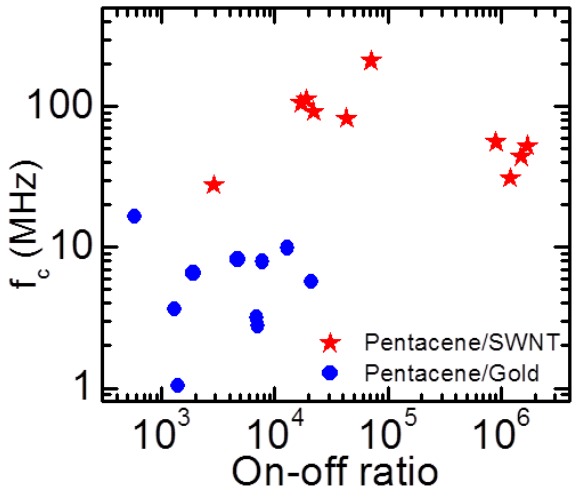

Figure 4.13: Cutoff frequency is plotted against corresponding current on-off ratio for 10 pentacene/SWNT devices (red star) and 10 pentacene/gold devices (blue circle).

The improved performance of our short channel OFETs using SWNT electrodes over the control and reported OFETs using gold electrodes is attributed to enhanced charge injection from aligned array SWNT electrodes. Compared to gold, carbon nanotube form a lower contact barrier with pentacene due to strong pi-pi interaction leading to higher charge injection from nanotube electrodes into the pentacene [14]. Additionally, in contrast to gold, carbon nanotubes have electric field emission properties due to their one dimensional structure and the larger field emission comes from the nanotube tips than the side-wall [29, 30]. The open-ended tips composed of irregular-shaped graphitic sheets which have more dangling bond states on their edges than the flat edge of the usual close-ended nanotubes [30]. These dangling bond states have a better coupling with states of the emitted electrons which results in more emission current[30, 31]. The density of nanotubes in our aligned array electrodes is very high (~15-20 SWNTs/μm) and they are parallel to each other's. Since, in our nanotubes electrodes, all the nanotube tips are open-ended fabricated through oxidative etching, the field emission of the nanotubes are enhanced [32]. Therefore, a large number of parallel nanotubes with open-ended

tips contribute to the field emission simultaneously resulting in higher charge injection in the devices.

Table 4.1: Comparison of our OFETs performance with the reported short channel OFETs.

Electrodes	Material	L (μm)	W (μm)	On/off	μ(cm^2/Vs)	f_c (MHz)	References
Gold	α- 6T	0.2	20	1.0×10^4	0.0001	0.02	APL 76, 1941 (2000)
Gold	Pentacene	3	2	2.2×10^2	0.3	13.56	APL 88, 1123502 (2006)
Gold	DNTT	0.5	2200	1.0×10^5	0.31	5	APL 97, 013301 (2009)
Gold	DTTT	1	1100	1.0×10^6	0.2	4	Adv. Mater 23, 3047 (2011)
Gold	Pentacene	0.7	25	2.1×10^4	0.05	16	This work (control device)
Align SWNT	Pentacene	0.7	25	1.7×10^6	0.65	211	This work

(a) α- 6T : Sexithiphene; (b) DNTT : Dinaphtho[2,3-b:2',3'-f] thieno[3,2-b]thiophene

4.5 PBTTT Transistor with CNT Aligned Array Electrodes

In this section, we show fabrication and electronic transport properties of the Poly (2,5-bis(3-tetradecylthiophen-2-yl)thieno[3,2-b] thiophene) (PBTTT) field effect transistors using aligned array CNT electrodes.

4.5.1 Fabrication of PBTTT Transistors

PBTTT power was dissolved in anisole with a concentration of 0.25 mg/mL at 90 ^oC in a glass vial. Bottom contacted PBTTT FETs were fabricated by depositing PBTTT film onto chips containing both CNT and Au electrode by drop cast method inside a N_2 glove box and kept 12 h to evaporate the solvent. The channel length and width for both CNT and gold electrode were 2 μm and 25 μm respectively. The CNT/PBTTT and Au/PBTTT devices were fabricated at same run and measured at the same time to minimize the experimental errors. The AFM images of the thin films with thickness of ~ 80 nm on the chip contain CNT electrodes are shown in Figure 4.14.

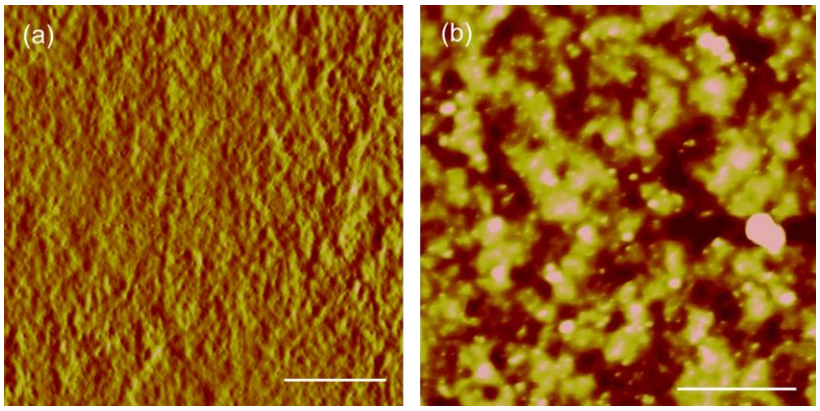

Figure 4.14: AFM image of deposited PBTTT thin film. (a) height image (b) phase image. The scale bars: 500 nm.

4.5.2 Transport Properties of PBTTT Transistors

Figure 4.15 shows I_d - V_d curves at V_g = 0 V to -80 V with -20 V interval of a representative CNT/PBTTT device. This figure shows excellent current modulation along with current saturation with gate voltage. In addition, the linear behavior of the output curves a low V_d indicating a good interfacial contact between CNT electrode and PBTTT. The calculated linear mobility for this device is found to be 0.06 $cm^2/V.s$ and current on-off ratio of 1×10^4.

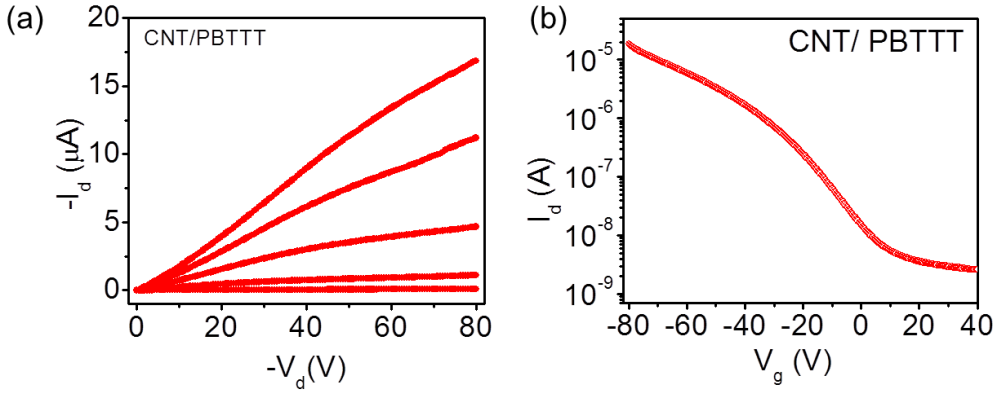

Figure 4.15: (a) Output characteristics (I_d versus V_d) at V_g = 0 to -80 V with -20V steps of the same device. (b) Transfer characteristics (I_d versus Vg) at V_d = -20 V of typical CNT/PBTTT device.

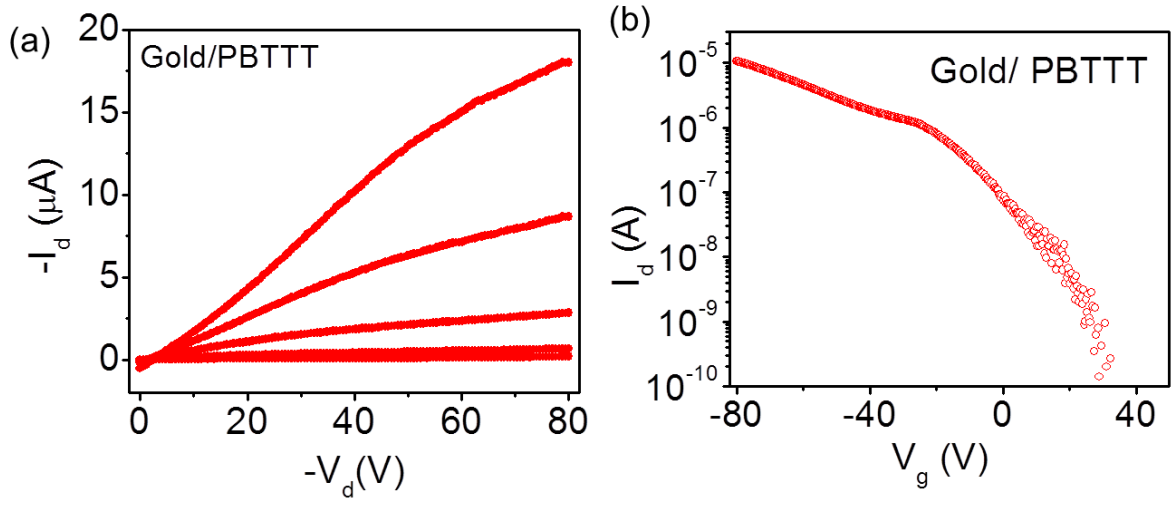

Figure 4.16: (a) Output characteristics (I_d versus V_d) at V_g = 0 to -80 V with -20V steps of the same device. (b) Transfer characteristics (I_d versus V_g) at V_d = -20 V of typical gold/PBTTT device.

The I_d-V_d and I_d -V_g curves of the gold/PBTTT device are shown in Figure 4.16. The mobility and current on-off ratio of this device are 9.3×10^3 and 0.03 cm^2/V.s, respectively. Although mobility of the CNT/PBTTT is slightly higher than that of the mobility of the gold/PBTTT OFET, the improvement is not significant. This slightly higher mobility in the CNT/PBTTT device may due to device-to-device variation. In order to examine the device-to-device reproducibility, we measured total 18 devices (9 CNT/PBTTT devices and 9 gold/PBTTT devices). The mobility versus corresponding current on-off ratio of these devices is shown in Figure 4.17. This figure shows that the device performances such as mobility, current on-off ratio are not improved with the CNT electrode. This result is a sharp contrast to our result obtained for the CNT/P3HT and CNT/pentacene OFETs. We showed in the last sections that both the performance of the P3HT and pentacene OFETs were significantly improved with CNT

electrodes. Currently it is not clear why CNT electrodes cannot improve the performance of the PBTTT OFETs. We are still working on this project to understand this.

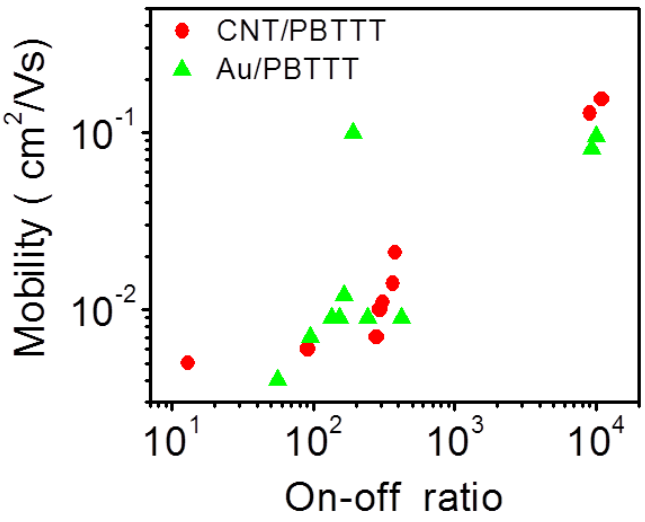

Figure 4.17: Mobility versus corresponding current on-off ratio for 9 CNT/PBTTT devices (red circle) and 9 gold/PBTTT devices (green circle).

4.6 C60 Transistor (n-type) with CNT Aligned Array Electrodes

In the last few sections, we have demonstrated p-type OFETs with aligned array CNT electrodes such as P3HT OFET, pentacene OFETs. In this section, we show the fabrication and characterization of n-type OFETs based on Buckminsterfullerene (or buckyball) (C60). Both p-type and n-type transistor are required in fabricating the logic circuits.

4.6.1 Fabrication of C60 Transistors

We obtained C60 power from Nano-C. The C60 OFETs were fabricated by thermal evaporation of C60 into the chip contained CNT electrodes in a vacuum chamber at pressure 1×10^{-6} Pa. Since the fabrication process of the C60 OFETs is similar to the fabrication process of the pentacene OFETs, here we do not discuss the details fabrication steps of C60 FETs.. The

thickness of the C60 film is ~ 30 nm. In this study we used CNT electrodes with channel length of 2 um and channel width 25 um.

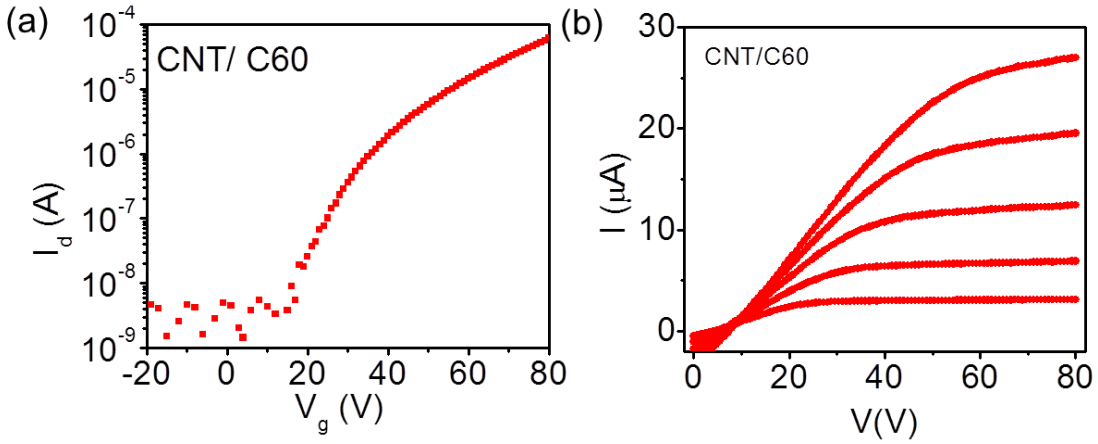

Figure 4.18: (a) Transfer characteristics (I_d versus V_g) at V_d = 80 V of typical CNT/C60 device. (b) Output characteristics (I_d versus V_d) at V_g = 0 to 80 V with 20V steps of the same device.

4.6.2 Transport Properties of C60 Transistors

The I_d - V_g and I_d - V_d characteristics of a typical CNT/C60 OFETs are shown in Figure 4.18a and 4.18b respectively. The main different of the CNT/C60 OFETs devices with p-type OFETs (CNT/P3HT, CNT/pentacene) is that in this device the magnitude of the current is increased with positive gate-voltage, which is typical behavior of the n-type. The current on-off ratio and mobility of CNT/C60 device is 1.7×10^4 and 0.12 cm^2/Vs. We also measured the control devices fabricated with gold electrodes. The I_d - V_g and I_d - V_d characteristics of a typical gold/C60 OFETs are shown in Figure 4.19a and 4.19b respectively. The current on-off ratio and mobility of gold/C60 device is 5.8×10^3 and 0.07 cm^2/Vs, which are lower than that of the CNT/C60 device.

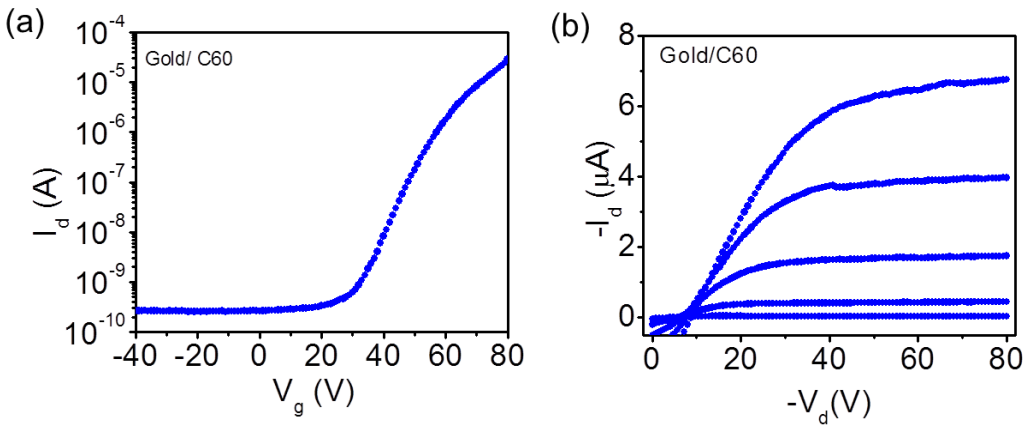

Figure 4.19: (a) Transfer characteristics (I_d versus V_g) at V_d = 80 V of typical gold/C60 device. (b) Output characteristics (I_d versus V_d) at V_g = 0 to 80 V with 20V steps of the same device.

4.7 Conclusion

We demonstrated high performance OFETs using aligned array carbon nanotube source and drain electrodes. For fabricating OFETs we used various organic semiconductors (both p-type and n-type). All the devices fabricated with CNT electrodes have shown improved device performance than that of the device fabricated with metal electrodes. Our short channel OFETs with SWNT array electrode show high on-current, high current on-off ratio and does not show "short channel" effect owing to improved charge injection from densely aligned SWNTs with open-ended and parallel tips. The maximum mobility of 0.65 cm^2/Vs and a maximum on-off ratio of 1.7×10^6 of the OFETs with CNT electrodes reported here are higher than that of other reported short channel devices. The maximum cutoff frequency of our device is 211 MHz, which is the best reported so far for organic transistors. Our result presented here is a significant step forward in fabricating high performance organic electronic devices.

4.8 References

1. G. Horowitz, Organic Thin Film Transistors: From Theory To Real Devices. *J. Mater. Research* **19**, 1946 (2004).

2. C. D. Dimitrakopoulos, P. R. L. Malenfant, Organic Thin Film Transistors for Large Area Electronics. *Adv. Mater.* **14**, 99 (2002).

3. C.-a. Di, Y. Liu, G. Yu, D. Zhu, Interface Engineering: An Effective Approach toward High-Performance Organic Field-Effect Transistors. *Account. Chem. Res.* **42**, 1573 (2009).

4. S. D. Wang, T. Minari, T. Miyadera, K. Tsukagoshi, Y. Aoyagi, Contact-Metal Dependent Current Injection In Pentacene Thin-Film Transistors. *App. Phys. Lett.* **91**, 203508 (2007).

5. R. Schroeder, L. A. Majewski, M. Grell, Improving Organic Transistor Performance With Schottky Contacts. *App. Phys. Lett.* **84**, 1004 (2004).

6. N. Koch, A. Kahn, J. Ghijsen, J. J. Pireaux, J. Schwartz, R. L. Johnson and A. Elschner Conjugated Organic Molecules On Metal Versus Polymer Electrodes: Demonstration Of A Key Energy Level Alignment Mechanism. *App. Phys. Lett.* **82**, 70 (2003).

7. I. G. Hill, A. Rajagopal, A. Kahn, Y. Hu, Molecular Level Alignment At Organic Semiconductor-Metal Interfaces. *App. Phys. Lett.* **73**, 662 (1998).

8. L. Burgi, T. J. Richards, R. H. Friend, H. Sirringhaus, Close Look At Charge Carrier Injection In Polymer Field-Effect Transistors. *J. Appl. Phys.* **94**, 6129 (2003).

9. K. A. Singh, G. Sauve, R. Zhang, T. Kowalewski, R. D. McCullough and L. M. Porter, Dependence Of Field-Effect Mobility And Contact Resistance On Nanostructure In Regioregular Poly(3-Hexylthiophene) Thin Film Transistors. *App. Phys. Lett.* **92**, 263303 (2008).

10. X. Guo, C. Nuckolls, Functional Single-Molecule Devices Based On Swnts As Point Contacts. *J.Mater. Chem.* **19**, 5470 (2009).

11. X. Guo, S. Xiao, M. Myers, Q. Miao, M. L. Steigerwald and C. Nuckolls Photoresponsive Nanoscale Columnar Transistors. *PNAS* **106**, 691 (2009).

12. P. F. Qi, A. Javey, M. Rolandi, Q. Wang, E. Yenilmez and H. J. Dai, Miniature Organic Transistors With Carbon Nanotubes As Quasi-One-Dimensional Electrodes. *J.Am.Chem. Soc.* **126**, 11774 (2004).

13. K. Tsukagoshi, I. Yagi, Y. Aoyagi, Pentacene Nanotransistor With Carbon Nanotube Electrodes. *App. Phys. Lett.* **85**, 1021 (2004).

14. C. Chia-Hao, C. Chao-Hsin, Y. Jung-Yen, Pentacene-Based Thin-Film Transistors With Multiwalled Carbon Nanotube Source And Drain Electrodes. *App. Phys. Lett.* **91**, 083502 (2007).

15. F. Cicoira, C. M. Aguirre, R. Martel, Making Contacts to n-Type Organic Transistors Using Carbon Nanotube Arrays. *ACS Nano* **5**, 283 (2011).

16. C. M. Aguirre, C. Ternon, M. Paillet, P. Desjardins, R. Martel, Carbon Nanotubes as Injection Electrodes for Organic Thin Film Transistors. *Nano Lett.* **9**, 1457 (2009).

17. A. Southard, V. Sangwan, J. Cheng, E. D. Williams, M. S. Fuhrer, Solution-Processed Single Walled Carbon Nanotube Electrodes For Organic Thin-Film Transistors. *Org. Electron.* **10**, 1556 (2009).

18. Y. Y. Zhang, Y. Shi, F. Chen, S. G. Mhaisalkar, L.-J. Li, B.S. Ong, Y. Wu, Poly(3,3 '''-Didodecylquarterthiophene) Field Effect Transistors With Single-Walled Carbon Nanotube Based Source And Drain Electrodes. *App. Phys. Lett.* **91**, (Nov, 2007).

19. S. L. Hellstrom, R. Z. Jin, R. M. Stoltenberg, Z. Bao, Driving High-Performance n- and p-type Organic Transistors with Carbon Nanotube/Conjugated Polymer Composite Electrodes Patterned Directly from Solution. *Advan.Mater.* **22**, 4204 (2010).

20. S. Shekhar, P. Stokes, S. I. Khondaker, Ultrahigh Density Alignment of Carbon Nanotube Arrays by Dielectrophoresis. *ACS Nano* **5**, 1739 (2011).

21. J. Zaumseil, H. Sirringhaus, Electron and Ambipolar Transport in Organic Field-Effect Transistors. *Chem. Rev.* **107**, 1296 (2007).

22. A. Dodabalapur, Organic and polymer transistors for electronics. *Mater. Today* **9**, 24 (2006).

23. B. Crone, A. Dodabalapur, Y.-Y. Lin, R. W. Filas, Z. Bao, A. LaDuca, R. Sarpeshkar, H. E. Katz & W. Li., Large-Scale Complementary Integrated Circuits Based On Organic Transistors. *Nature* **403**, 521 (2000).

24. J. Collet, O. Tharaud, A. Chapoton, D. Vuillaume, Low-Voltage, 30 Nm Channel Length, Organic Transistors With A Self-Assembled Monolayer As Gate Insulating Films. *App. Phys. Lett.* **76**, 1941 (2000).

25. J. Z. Wang, Z. H. Zheng, H. Sirringhaus, Suppression Of Short-Channel Effects In Organic Thin-Film Transistors. *App. Phys. Lett.* **89**, (Aug, 2006).

26. V. Wagner, P. Wobkenberg, A. Hoppe, J. Seekamp, Megahertz Operation Of Organic Field-Effect Transistors Based On Poly(3-Hexylthiopene). *App. Phys. Lett.* **89**, 243515 (2006).

27. B. Bräuer, R. Kukreja, A. Virkar, H. B. Akkerman, A. Fognini, T. Tyliszczak and Z. Bao, Carrier Mobility in Pentacene As A Function Of Grain Size And Orientation Derived From Scanning Transmission X-Ray Microscopy. *Org. Electron.* **12**, 1936 (2011).

28. R. Rotzoll, S. Mohapatra, V. Olariu, R. Wenz, M. Grigas, K. Dimmler, O. Shchekin and A. Dodabalapur, Radio Frequency Rectifiers Based On Organic Thin-Film Transistors. *App. Phys. Lett.* **88**, 123502 (2006).

29. U. Haas, H. Gold, A. Haase, G. Jakopic, B. Stadlober, Submicron Pentacene-Based Organic Thin Film Transistors On Flexible Substrates. *App. Phys. Lett.* **91**, 043511 (2007).

30. M. S. Wang, L. M. Peng, J. Y. Wang, C. H. Jin, Q. Chen, Quantitative Analysis of Electron Field-Emission Characteristics of Individual Carbon Nanotubes: The Importance of the Tip Structure. *J.Phys. Chem. B* **110**, 9397 (2006).

31. K. Tada, K. Watanabe, Ab Initio Study of Field Emission from Graphitic Ribbons. *Phys. Rev. Lett.* **88**, 127601 (2002).

32. A. G. Rinzler, J. H. Hafner, P. Nikolaev, P. Nordlander, D. T. Colbert, R. E. Smalley, L. Lou, S. G. Kim and D. Tománek Unraveling Nanotubes: Field Emission from an Atomic Wire. *Science* **269**, 1550 (1995).

CHAPTER 5: CHARGE INJECTION AND TRANSPORT MECHANISMS OF ORGANIC FIELD EFFECT TRANSISTORS WITH CARBON NANOTUBE ELECTRODES*

5.1 Introduction

Due to large interfacial contact barrier, one of the major problems in the fabrication of high performance organic electronic devices is inefficient charge injection from metal electrode into organic semiconductors (OSC)[1-5]. When the metal electrodes are contacted with the OSC, interfacial barriers such as Schottky barrier, dipole barrier are formed at the metal-OSC interface [6-9]. To be injected into the OSC, the charge carriers must overcome the large interface potential barrier either by thermal emission or tunneling [10-14]. A decrease in barrier height and width will improve the charge injection which in turn will have significant impact in fabricating high-performance organic electronic devices. Due to their unique electronic properties carbon nanotubes (CNTs) are considered to be a promising electrode material that can overcome the limitations of metal electrodes [15-22]. Recent room temperature studies by our group and others have shown that, compared to organic field effect transistor (OFET) using standard metal electrodes, OFETs using CNT electrodes have better mobility and higher on-current [17-22]. It is speculated that such improved device performance may be due to the improved injection of charge carriers from CNT to OSC owing to strong π-π bonding between the CNTs and OSC.[18, 23] Although metal/OSC contact has been studied in great detail, very little information has been reported on the nature of CNT/OSC contact. In particular, there is no information about the barrier height or charge injection mechanism at the CNT/OSC interface. Such understanding can

* Portions of this chapter have been published in the following journals: ***ACS Nano*** *6,* 4993 *(2012).*

be obtained from low temperature transport study and is of great importance for achieving the overreaching goal of the CNT electrodes in organic electronics.

In this chapter, we study charge carrier injection mechanism at CNT electrode/ pentacene interface using the temperature dependent electronic transport measurements and provide direct evidences of low charge carrier injection barrier. We show that, the current density-voltage (*J-V)* characteristics of the device above 200 K are well described by Richardson Schottky (RS) model indicating that charge carrier injection is dominated by thermal emission at high temperature regime. We calculated a barrier height (φ_B) of 0.16 eV of the CNT/pentacene which is much lower compared to the reported value of barrier height for metal/pentacene devices. We also show that the charge carrier injection mechanism crosses over from thermal emission to tunneling mechanism below 200 K, where charge injection is weakly temperature dependent. The *J-V* characteristics show a transition from direct tunneling at low bias to F-N tunneling mechanism at high bias further confirming low charge injection barrier at the CNT/pentacene interface.

5.2 Theoretical Background of Charge Injection

The schematic diagram of a typical interface at different temperatures (*T*) and bias voltages (*V*) are shown in Figure 5.1a considering a simple rigid band model. Depending upon the temperature and bias voltage, different transport phenomena can occur as described by the phase diagram of Figure 5.1b. At low bias voltage and sufficiently high temperature, a large number of thermally activated charge carriers can overcome the barrier height (φ_B) in a classical way resulting in thermionic emission (Figure 5.1a, I) [13, 14]. If the barrier height is large, this kind of emission will occur at temperatures higher then room temperature. Whereas, for a low

barrier height, thermionic emission can occur even at low temperatures. The *J-V* characteristics in this regime can be modeled using Richardson-Schottky (RS) equation for thermionic emission [13]:

$$J = A^{*}T^{2}\exp[\frac{-(\Phi_B - \sqrt{q^3V/4\pi\varepsilon_0\varepsilon_r d})}{k_bT}] \quad (5.1)$$

where A^* is effective Richardson constant, ε_r is the permittivity of the OSC, ε_0 is the permittivity of vacuum, q is the electron charge, and d is the width of the interface barrier. The barrier height (φ_B) can be directly calculated from thermal emission regime by recognizing that at V = 0 V, $J = J_0 = A^{*}T^{2}\exp(-\Phi_B / k_bT)]$. Therefore, a plot of $ln(J_0/T^2)$ *versus* T^{-1} will show activated behavior and the slope will give the value for φ_B [24]

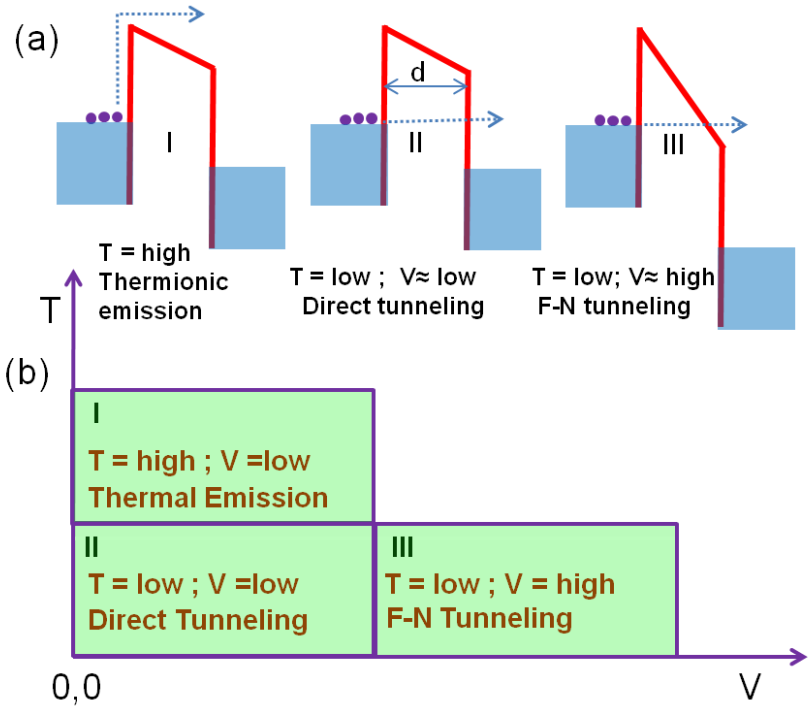

Figure 5.1: (a) Schematic diagram of a interfacial barrier at different temperatures and voltages. The circles represent the charge carriers and the arrow indicates the charge carrier injection processes: (I) thermionic emission, (II) direct tunneling, and (III) Fowler-Nordheim (F-N) tunneling. (b) Typical phase diagram of transport regimes at various temperature and voltages.

When the temperature decreases, there may not be enough thermal energy for the charge carriers to overcome the barrier height and the charge injection is dominated by tunneling through the interface barrier [13, 14, 25]. With increasing bias voltage, the shape of the tunnel barriers changes from trapezoidal (II in Figure 5.1a) to triangular (III in Figure 5.1a) [26]. At low bias voltage, the tunnel barrier is trapezoidal (Figure 5.1a, II) and the *J-V* relation is described by direct tunneling mechanism [13]:

$$J \propto V \exp\left[-\frac{2d\sqrt{2m\Phi_B}}{\hbar}\right] \tag{5.2}$$

where, $\hbar$ is the Planck's constant divided by 2π, m is the effective mass of the charge carrier. When the bias voltages exceed the barrier height, the tunnel barrier becomes triangular (Figure 5.1a, III) and the *J-V* relation is described by Fowler-Nordheim (F-N) tunneling [13]:

$$J \propto V^2 \exp\left[-\frac{4d\sqrt{2m\Phi_B^3}}{3\hbar qV}\right] \tag{5.3}$$

The above *J-V* relations in Eq (2) and Eq (3) can be linearized in a logarithm scale to become Eq. (4) and Eq. (5) respectively

$$\ln\left(\frac{J}{V^2}\right) \propto \ln\left(\frac{1}{V}\right) - \frac{2d\sqrt{2m\Phi_B}}{\hbar} \tag{5.4}$$

$$\ln\left(\frac{J}{V^2}\right) \propto -\left(\frac{1}{V}\right)\left(\frac{4d\sqrt{2m\Phi_B^3}}{3\hbar q}\right) \tag{5.5}$$

Therefore, a plot of *ln* (J/V^2) against *1/V* will show logarithmic dependence in direct tunneling (low bias) regime and linear dependence with a negative slope in F-N tunneling (high bias) regime with an inflection point, describing the transition from direct to F-N tunneling

regime. In cases of interfaces with large barrier height and width, only F-N tunneling can be observed and no measurable current can be detected before the onset of F-N tunneling. Whereas for the interface with a small barrier height and width, the both direct and F-N tunneling can be observed with a transition from one regime to another.[27] Therefore, a transition from direct tunneling to F-N tunneling is a hallmark of low interfacial barrier [27] and has not been observed in the metal/OSC interface where the interface barrier is large.

5.3 Experimental Methods

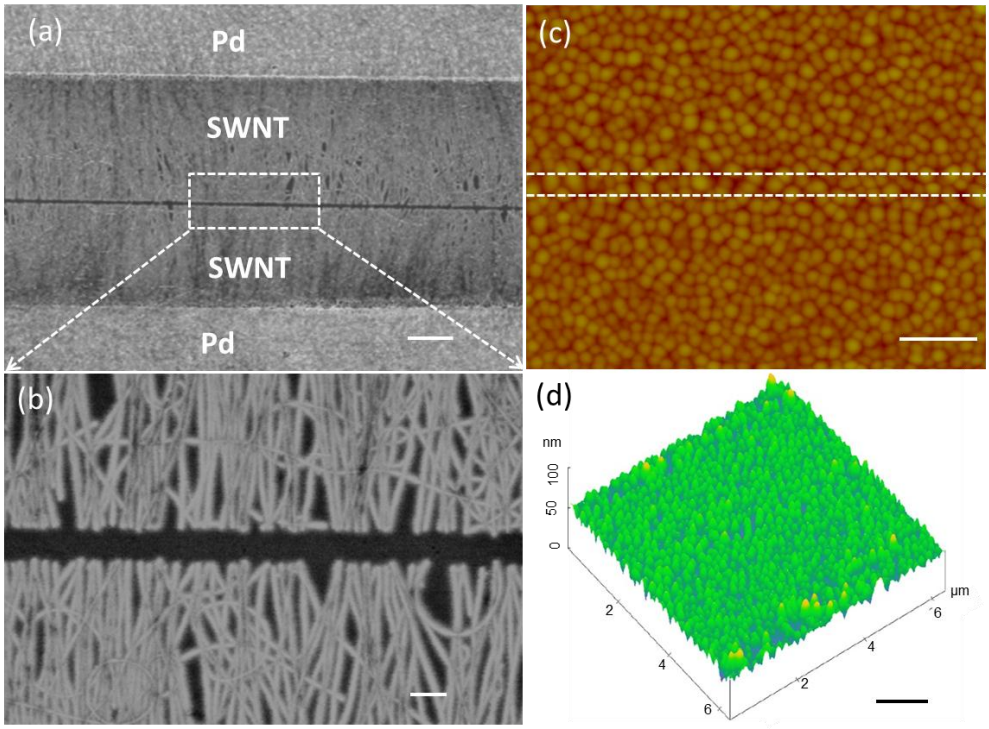

Figure 5.2: (a) SEM image of a part of densely aligned SWNT source and drain electrodes. The SWNTs were assembled versus dielectrophoresis. (b) High magnification SEM image of the Figure (a). Tapping mode AFM (c) height and (d) surface image of the deposited pentacene thin film. The white region marks the channel area defined by the SWNT electrodes where pentacene is deposited onto the SiO_2 substrate. The scale bars in the Figure s (a), (c) and (d) are 1 µm, and in Figure (b) is 200 nm .

To examine the charge injection mechanism at the CNT/OSC interface, we fabricated single walled carbon nanotube (SWNT) source and drain electrodes through dielectrophoretic

(DEP) assembly of SWNTs in a dense array and oxidative cutting of the SWNTs array by electron beam lithography (EBL) followed by precise oxygen plasma etching. The details of the SWNT assembly and electrode fabrication can be found in our recent publications [17-19, 28]. In brief, we used heavily doped silicon as substrates for fabricating our devices. The silicon substrate is coated with a thermally grown 250 nm thick SiO_2 layer which is used dielectric layer.. Palladium (Pd) patterns of 5 μm × 25 μm, fabricated by optical lithography, were used to align the nanotubes via ac dielectrophoresis (DEP) from a high quality, stable and surfactant free SWNT aqueous solution. For this study, we fabricated 5 samples with 25 - 30 SWNT/μm in the array. (See Chapter 3 for detailed fabrication). The resistances of the assembled SWNT arrays were in the range of 400 Ω - 800 Ω with corresponding sheet resistances of 1.5- 3 KΩ/□ making them suitable as an electrode material. After the assembly, SWNT source and drain electrodes of channel length L = 200 nm and width W = 25 μm were fabricated by defining a window using standard EBL process and oxygen plasma etching of the exposed nanotubes inside the window.

Figure 5.2a shows a scanning electron microscopy (SEM) image of a part of the SWNT source and drain electrodes. Figure 5.2b shows a high magnification image of the electrode. From this image, we calculate 68 SWNTs in 2.8 μm long image, giving a linear density of 24 SWNTs/μm. The nanotubes are swollen due to the low kV imaging. Figure 5.2b also shows that most of the nanotubes in the electrodes are well aligned with open-ended tips (see also AFM image in Chapter 4). Finally, we deposited pentacene thin film of 30 nm by thermal evaporation. Figure 5.2 c and 5.2 d show a part of the height and surface view of the AFM image of the deposited pentacene film morphology. The morphology of the pentacene film within the channel on SiO_2 substrate slightly differs than the morphology of pentacene on the nanotube electrodes. The pentacene grain size on nanotube electrodes is ~ 140 - 160 nm with a surface roughness of

~ 3 nm, whereas pentacene grain size within the channel on SiO_2 substrate is ~ 170 - 190 nm with a surface roughness of ~ 4.2 nm (see Figure 5.3).

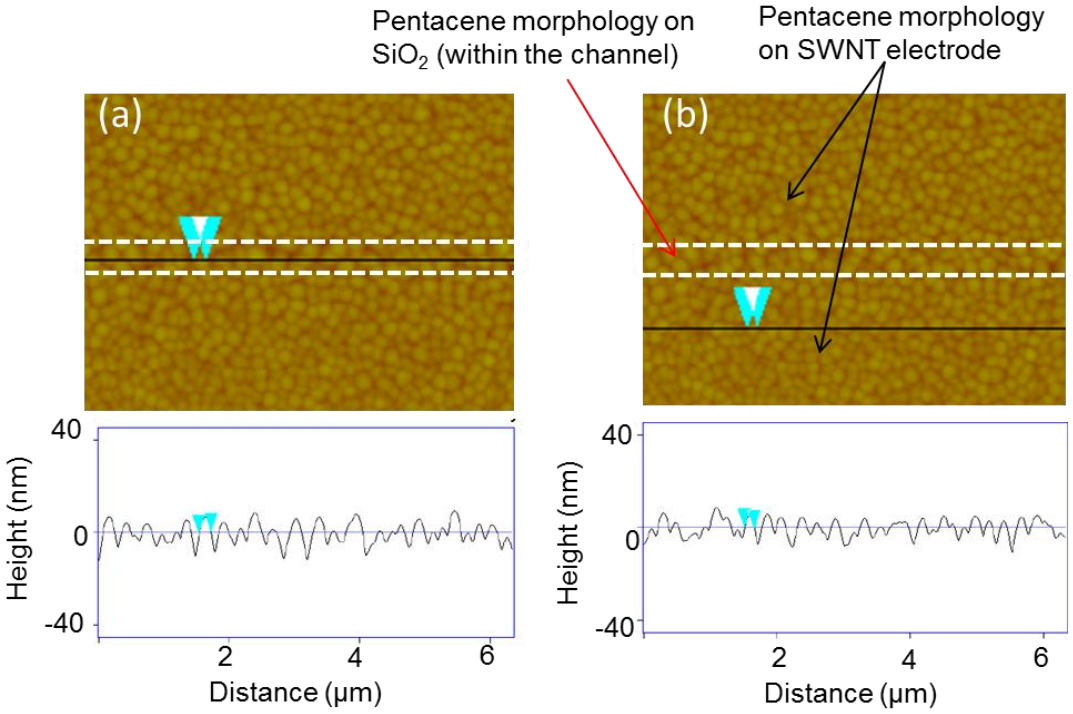

Figure 5.3: Atomic force microscopy (AFM) images and their height profiles of the pentacene film on (a) SiO_2 within the channel (b) SWNT electrodes. The height profiles show that the typical pentacene grain size within the channel is ~180 nm with rms surface roughness of ~ 4.2 nm. On the other hand, the typical pentacene grain size on SWNT electrode is ~150 nm with rms surface roughness of ~ 3 nm

In this study, we chose L = 200 nm because at this channel length the contact resistance is much more dominating over the channel resistance so that the charge transport characteristics will be dominated by contact. To determine the contact resistance, we have fabricated pentacene devices using SWNT electrodes of different channel lengths (L= 200 nm, 700 nm, 2, 3 and 4 μm) and measured the total resistance (R) of the devices at room temperature at V_g = -80 V. This is plotted in Figure 5.4. The total resistance of the devices is equal to the sum of the contact

resistance (R_c) and chancel resistance (R_{ch}); $R = R_c + R_{ch}$. The *R vs L* plot shows that *R* is increased linearly with increasing *L*. We calculated $R_c \sim 2$ MΩ of the SWNT/pentacene by extrapolating the linear line to $L = 0$ μm. For the device of $L = 200$ nm, the total resistance is 2.3 MΩ demonstrating that the contact resistance (2 MΩ) is much higher than the channel resistance (0.3 MΩ).

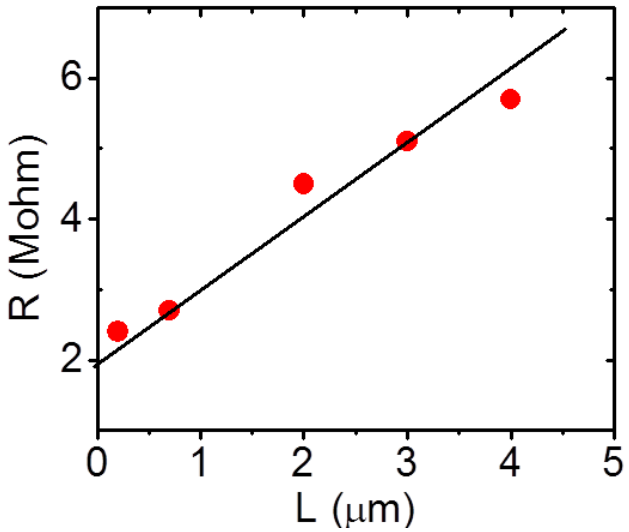

Figure 5.4: Plot of total resistance as a function of channel length of the SWNT/pentacene devices.

Another reason for choosing as small channel length as possible is to reduce the number of grain boundaries in the active material. It is well known that the conductivity of the OSC is limited by the grain boundaries, and the strong temperature dependence of the resistance and mobility of the OSC arise from the grain boundaries [29, 30] In larger channel length devices, there are many grain boundaries and the conductivity of the OSC is dominated by them. On the other hand, for very short channel length device, there are only a few grain boundaries and the conductivity is dominated by contact. Since the average grain size of the pentacene in our devices is about 180 nm, there will be only one grain boundary on an average along the channel

of our device (see Figure 5.2c) making these devices appropriate for studying interface effect. The devices were then bonded and loaded into a cryostat for the low temperature transport measurements. A total of 5 devices were measured. We measured *I-V* characteristics of our devices at different temperatures in the range of 300 K to 77 K. In order to take reproducible measurements at each temperature, we measured each *I-V* curve at least two times, and waited for 15 minutes in successive measurements. The temperature was controlled with a lakeshore temperature controller and we waited at least 10 minutes to stabilize the temperature before taking data.

5.4 Charge Injection Mechanism

5.4.1 Temperature Dependent Transport Characteristics

Before going to the low-temperature electronic transport measurement, the devices are characterized in room temperature (300 K). The current-voltage (*I-V*) characteristics at gate-source voltages (V_g) = 0 to -80 V, and *I*-V_g characteristics at fixed *V* = -20 and -40V of a typical SWNT/pentacene and a Pd/pentacene devices at temperature room temperature (300 K) are shown in Figure 5.5. The *I-V* curves of both the devices show a non-linear behavior at low bias, indicating that charge transport is limited by the contact. This is expected because channel length of our devices is only 200 nm. As we see from the Figure 5.5 (b and d) that the on-current of the SWNT/pentacene (13μA) is ~16 time higher the on-current of the Pd/pentacene device (0.8 μA) at same *V* = -40 V and V_g = - 80 V condition. In addition, the current on-off ratio of the SWNT/pentacene is 3.4×10^4 whereas it is only 5.1×10^1 for Pd/pentacene device at *V* = - 40V. Therefore, SWNT/pentacene device have better performance than Pd/pentacene devices. This

suggests that charge injection from the SWNT electrode is more efficient into pentacene due to low injection barrier at SWNT/pentacene interface.

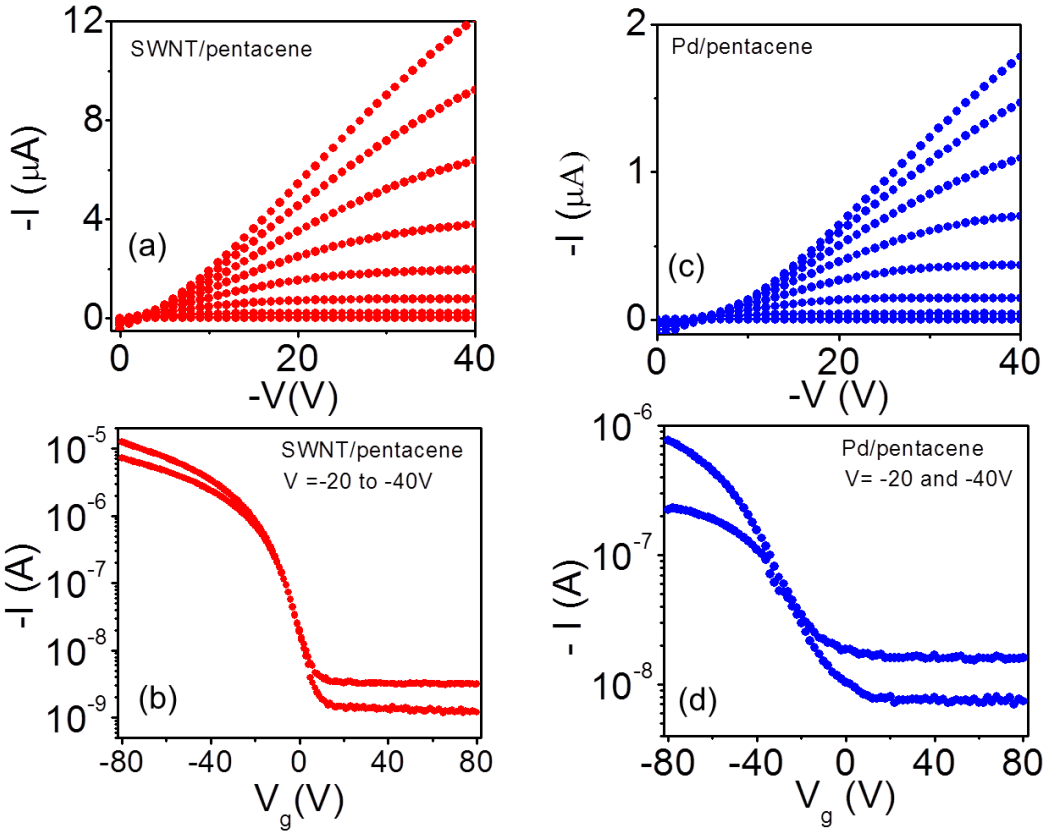

Figure 5.5: *I-V* characteristics at V_g = 0 to -80 V with -10 V steps of typical devices using (a) SWNT aligned array electrodes and (c) Pd electrodes. *I*-V_g characteristics at *V* = -20 V and -40V of the devices using (b) SWNT aligned array electrodes (d) Pd electrodes.

The higher current of the SWNT/pentacene device than that of the Pd/pentacene device also suggests that charge injection in the SWNT/pentacene devices coming from the SWNT electrodes, not from Pd used to anchor SWNTs. In addition, if the charge injection of the SWNT/pentacene devices were occurred from Pd patterns which are 5 μm apart, then the output current of the SWNT/pentacene device would be less than the Pd/pentacene devices (200 nm) at

the same bias voltage as the current is inversely proportional to the channel length for a fixed voltage. Therefore, the much higher current for the SWNT/pentacene devices show strong evidence that the charge injection mainly occurs from the SWNTs.

Figure 5.6 shows current-voltage (*I-V)* characteristics of a representative device at zero gate voltage plotted in a log-log scale measured at different temperatures from 300 K to 77 K (see Figure 5.5 for room temperature OFET characteristics). It can be seen from this Figure that the current strongly depends on both the temperature and voltage. Three interesting features can be seen in this Figure. At high temperature (above 200 K) and low bias voltage (regime I), the *I-V* curves strongly depend on the temperature, indicating thermally activated charge injection mechanism [13, 14] At low temperature (< 200 K), the *I-V* curves show weakly temperature-dependent phenomenon with current either weakly voltage dependent (regime II) or strongly voltage dependent phenomenon (regime III) that can be well described by the tunneling mechanism.[14, 25]

5.4.2 Thermionic Emission Mechanism

The strongly temperature-dependent *I-V* curves in regime I can be well described by the RS model for thermionic emission (Eq 5.1). This is shown in Figure 5.7(a) where we plot *lnJ* against $V^{1/2}$ for temperatures above 200 K. As expected from the RS model (*lnJ vs* $V^{1/2}$), all the curves show a straight line with positive slope. These data also allow us for the calculation of barrier height (Φ_B) at the SWNT/pentacene interface. In order to calculate the Φ_B, we first determined J_0 as function of the temperature by extrapolating the straight lines of Figure 5.7a to V = 0 V, and plotted $ln\ (J_0/T^2)$ as a function of $1/T$ in Figure 5.7b. This Figure clearly shows that the $ln(J_0/T^2)$ *versus* $1/T$ plot follows a linear relation with negative slope at higher temperature

range(above 200 K), denoted by the dot line. However, this plot deviates from the linear relation and becomes weakly temperature-dependent at lower temperature (below 200 K). This is consistent with Figure 5.6, region II and III where we saw weakly temperature-dependent *I-V* curves and signifies a transition from thermionic emission to tunneling mechanism. This transition phenomenon of our devices can be easily understood. At high temperature, a large number of charge carriers have energies large enough to cross the barrier height in a classical way [14]. However, when the temperature decreases, the energies of the charge carriers become low which may not be sufficient enough to overcome the barrier height and hence the thermionic emission stops. The charge injection only then occurs quantum mechanically by tunneling [14, 25].

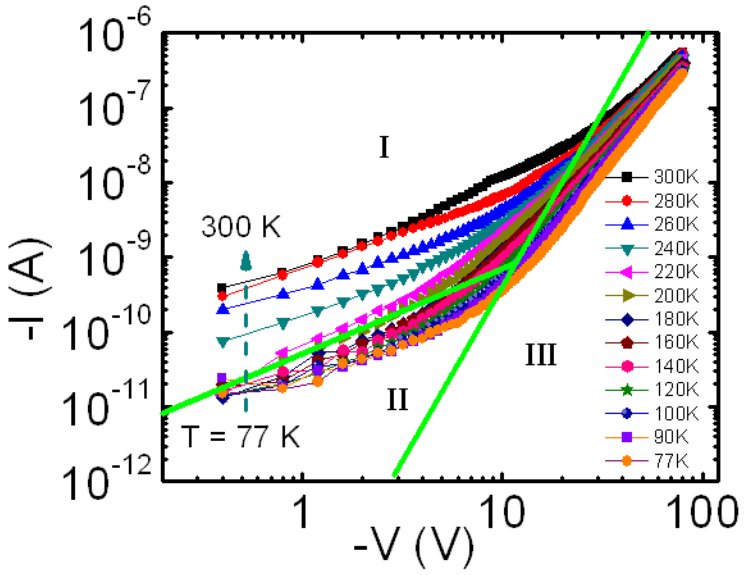

Figure 5.6: Log-log plot of the *I-V* characteristics of the SWNT/pentacene device in the temperature range of 300 - 77 K at V_g = 0V. I, II and III indicate the three different charge transport regimes depending on the *T* and *V* (marked by solid green lines). I, II and III corresponds to the regimes described in Figure 5.1.

5.4.3 Barrier Height at CNT/Organic Semiconductor Interface

We calculated a barrier height of 0.16 eV at the SWNT/pentacene interface from the slope of *ln* (J_0/T^2) *versus 1/T* plot in Figure 5.7b. We have measured and analyzed 5 SWNT/pentacene devices in this study and all the devices have shown similar transport characteristics. The calculated barrier height of the SWNT/pentacene interface is significantly lower than that of the reported barrier height of 0.5-0.85 eV at gold/pentacene interface measured by different groups[6, 31, 32], as well as our control Pd/pentacene device where we obtained a barrier height of 0.35 eV (Figure 5.8).

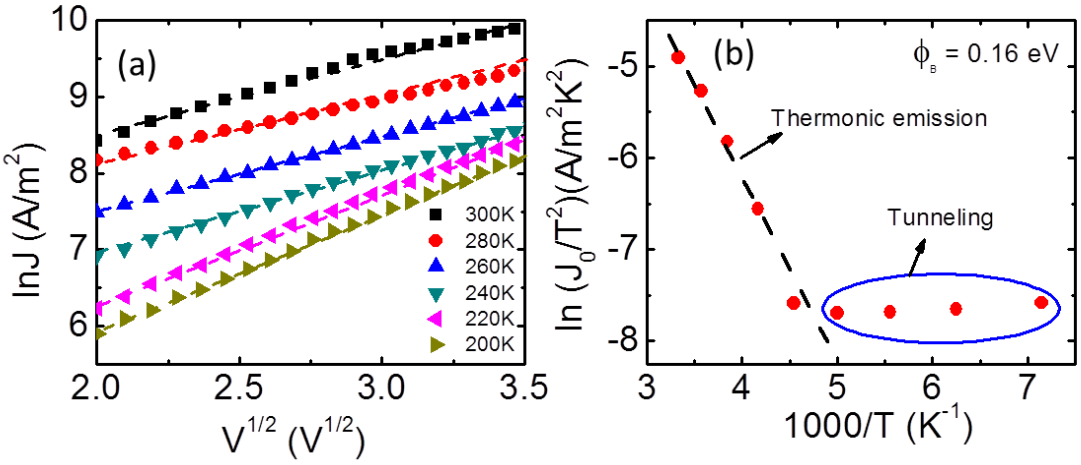

Figure 5.7: (a) *ln*(J/T^2) *versus* $V^{1/2}$ plot of the *I-V* data at temperature 300 to 200 K (regime I in Figure 5.6). The current densities at zero bias voltage (J_0) were obtained by extrapolating of the *ln* (J/T^2) curve at V = 0 V. (b) The relation between *ln* (J_0/T^2) and *1/T*. From the slope of the dotted line the interfacial energy barrier height at the SWNT/pentacene interface is determined to be 0.16 eV.

Interestingly, our measured barrier height at SWNT/pentacene is also similar to the barrier height reported for graphene/pentacene interface [33]. We note that we did not apply any V_g in the temperature-dependent *I-V* characteristics of our devices to extract the true barrier

height at the SWNT/OSC interface [12, 14]. It has been reported that Schottky barrier can be significantly reduced by applying V_g, and a barrier height measured at V_g other than 0 V is not a true barrier height [12, 14]. In addition, a finite V_g also reduces the tunnel barrier width in the tunneling regime enhancing the tunnel current [14].

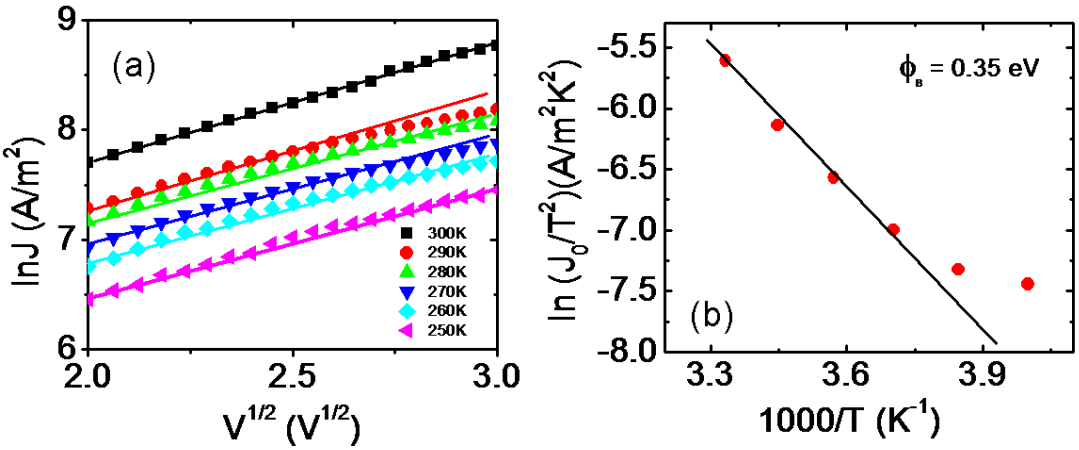

Figure 5.8: (a) $ln(J/T^2)$ versus $V^{1/2}$ plot of a representative Pd/pentacene device. The plot shows a linear relation in between lnJ and $V^{1/2}$, which is consistent with Richardson-Schottky (RS) model for thermionic emission. (b) Plot of $ln\ (J_0/T^2)$ as a function of $1/T$. The current densities at zero bias voltage (J_0) were obtained by extrapolating of the $ln\ (J/T^2)$ curves to V = 0 V. From the slope of the $ln\ (J_0/T^2)$ versus $1/T$, we calculated barrier height of 0.35 eV at Pd/pentacene interface.

In previous room temperature transport studies of the SWNT contacted OFET devices, better charge mobility and higher on-current were reported compared to the metal contacted devices [17-22]. It was speculated that the better performance was due to improved charge injection at the SWNT/OSC. However, no direct evidence of the barrier height at the SWNT/OSC was reported. Our study shows for the first time that a low charge injection barrier indeed exists at the SWNT/OSC interface. The work-functions for Pd, Au are 5.1 eV and it is 5.0 eV for SWNT [19, 34] while the highest occupied molecular orbital (HOMO) level of the pentacene is 5.1 eV [32]. Although the work-function of the metal (Pd, Au) and SWNT matches

with the HOMO level of the pentacene, however, significant barrier exist between the metal and pentacene interface. It has been reported that when pentacene is contacted with gold electrode, pentacene is physisorped onto the gold surface leading to the formation of dipole barriers at Au/pentacene interfaces [6-9]. This gives rise to a "push back" effect, a decrease of surface dipole potential energy of the gold surface in contact with the OSC [8, 9, 35]. As a result, the effective work function of gold electrodes reduces to 4.5 eV, giving rise to a large Schottky barrier for hole injection. Similar work function lowering may also occur for Pd/pentacene devices. In contrast, strong π-π interaction exists between the SWNT and pentacene [23]. Therefore, significant dipole formation may not occur and work-function of the SWNT may not be modified in contact with OSC causing the barrier to remain low.

5.4.4 Tunneling Mechanism

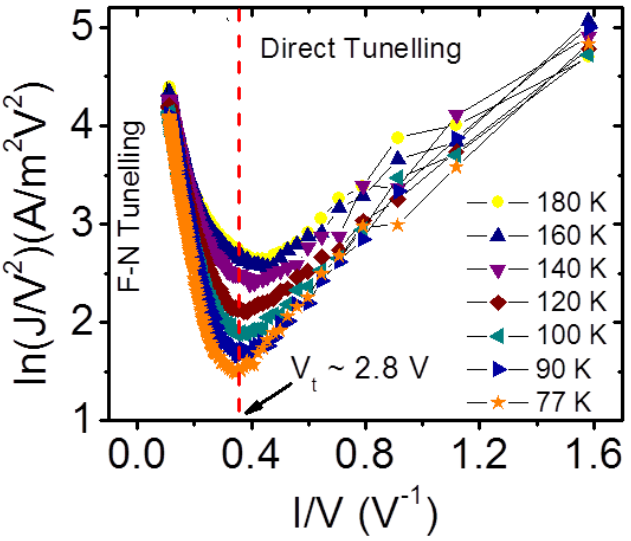

Figure 5.9: *ln* (J/V^2) versus *1/V* plot of the data for weakly temperature-dependent *I-V* data at temperature 180 - 77 K (regime II and III in Figure 5.6). The curves show a transition from direct tunneling to F-N tunneling with a voltage inflection point.

In Figure 5.7, we observed a deviation from RS model at temperatures below 200 K, possibly due to a transition from thermionic emission to tunneling. In order to confirm that

tunneling is indeed the injection mechanism, we analyzed our low temperature data using both the direct tunneling and F-N tunneling models. We mentioned earlier that a plot of *ln* (J/V^2) *versus 1/V* will show logarithmic dependence in direct tunneling (low bias) regime and linear dependence with a negative slope in F-N tunneling (high bias) regime with an inflection point, describing the transition from direct to F-N tunneling regime. Such a transition from direct to F-N tunneling is a hallmark of low interfacial barrier [27]. Figure 5.9 shows a plot of the *ln* (J/V^2) *versus 1/V* in the temperatures range of 180 K - 77 K. The most important feature of this Figure is that all the curves shows two distinct transport regimes with a voltage inflection points (V_t). The V_t of this devices is 2.8 V ($1/V \sim 0.35V^{-1}$). When V > 2.8 V, we observed a linear relationship of the *ln* (J/V^2) *versus 1/V* curves with negative slope for all the temperatures. This is more clearly shown in Figure 5.10a and is consistent with F-N tunneling model (Eq 5.5). From the slope of the *ln* (J/V^2) *versus 1/V* curves and using a barrier height of 0.16 eV, we have calculated a barrier width $d \sim 20$ nm of the SWNT/pentacene interface. However when V < 2.8 V, the transport characteristics changes and the curves cross over to a logarithmic dependence in *1/V* in agreement with direct tunneling . This is more clearly shown in supplementary Figure 5.10b. Therefore, from these results we confirm that the charge carrier injection of our device is dominated by direct tunneling at voltage less than transition voltage, and by F-N tunneling at the voltage higher than the transition voltage. In addition, the exhibition of the inflection point in the *ln*(J/V^2) *versus (1/V)* plots in Figure 5.10a provides a signature of a transition from direct tunneling to F-N tunneling in our devices. This confirms a change of the barrier shape at the SWNT/pentacene interface from trapezoidal to triangular with increasing bias voltage, as illustrated by band energy diagram in Figure 5.1.

The transition from the direct tunneling to F-N tunneling was not observed in the devices which have sustainable interfacial barrier height and width [27].Although F-N tunnelling has been reported in organic devices fabricated with metal electrodes [29, 36-38], the direct tunnelling as well as the transition from direct to F-N tunneling has not been observed in these devices. This is due to the existence of high barrier width at the metal/OSC interfaces. In contrast, we observed a transition from direct tunneling to F-N tunneling of our devices fabricated with SWNT electrode along with a low barrier height, which confirms that interfacial barrier height and width of SWNT/pentacene interface is very small

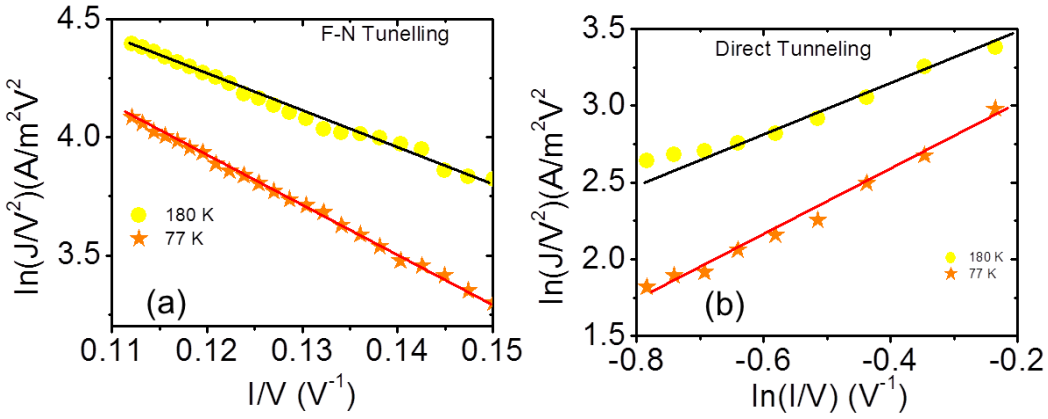

Figure 5.10: *ln* (J/V^2) versus *1/V* plot of the data for weakly temperature-dependent *I-V* data at temperature 180 - 77 K (regime II and III in Figure 5.6). The curves show a transition from direct tunneling to F-N tunneling with a voltage inflection point.

In this section I discussed charge injection mechanism at from the SWNT electrode to pentacene semiconductor. In this study a very short channel length SWNT electrodes L = 200 nm is used to confirm that the charge transport is dominated by the contact. It is found that charge injection barrier at SWNT/pentacene interfaces is smaller than barrier height at metal/pentacene interfaces. As we found that CNT forms better interfacial contact with pentacene, now we are

interested to investigate charge transport mechanisms in the pentacene device with SWNT electrodes.

5.4.5 Gate-Voltage Dependent Barrier Height at CNT/Organic Interface

In the last section, we discussed the charge injection mechanism of our devices at gate-voltage (V_g) at zero voltage, and determined the barrier height at the SWNT/pentacene interface. It is well known that the barrier height strongly depends on the gate voltage. In order to investigate how the barrier height changes with the gate-voltage in our devices, we performed gate-voltage dependent and temperature-dependent transport measurement of our SWNT/pentacene device fabricated with channel length of 700 nm.

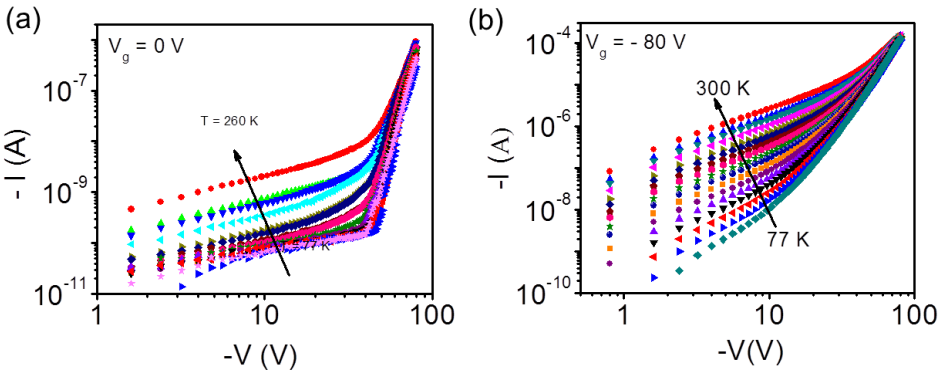

Figure 5.11: Log-log plot of the *I-V* characteristics of the SWNT/pentacene device in the temperature range of 300 - 77 K at (a) V_g = 0V and (b) V_g = -80 V.

In this study we did not use our device with channel length of 200 nm (which is used to investigate the charge injection at zero gate voltage), because this device did not show any gate-dependent transport due to short channel effect. We did not also use the larger channel length devices (larger than 700 nm), because in that case device will be dominated by the channel, not contact dominated. As we are investigating the interface, the contact dominating devices are

required for this study. The fabrication of devices, electronic transport measurement and analysis for calculating barrier height is similar to what we discussed in the previous section. Only difference in this study is that here we measured our devices at different gate voltages.

Figure 5.11 (a) and 5.11 (b) shows the *I-V* characteristics of a representative SWNT/pentacene device plotted in a log-log scale measured at different temperatures from 260 K to 77 K at V_g= 0 and V_g = -80 V, respectively. It can be easily seen from this figures that current strongly depends on both the temperature and voltage, and the magnitude of the current at V_g = - 80 V is higher than the current at V_g = 0V.

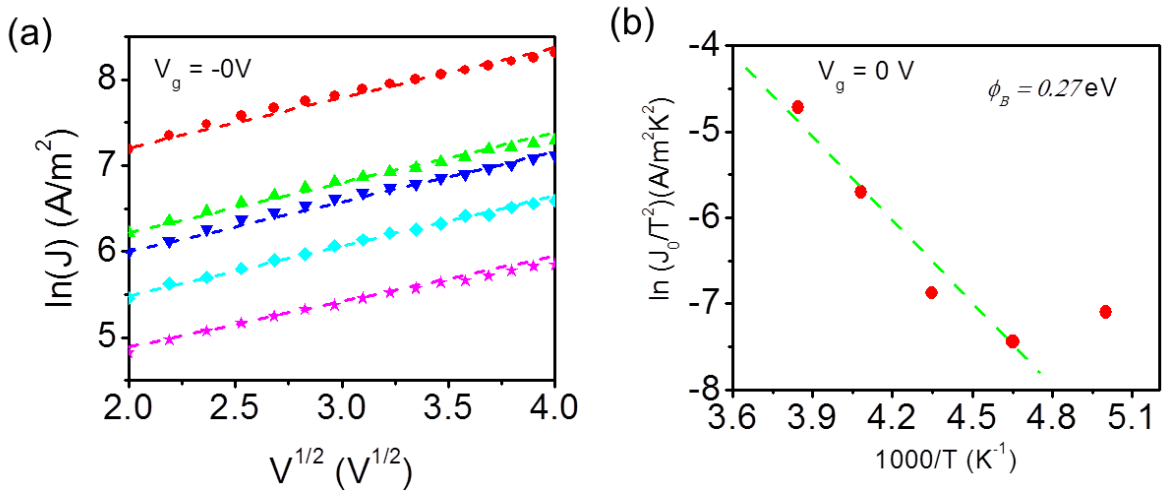

Figure 5.12: (a) ln(J/T2) versus V1/2 plot of a representative SWNT/pentacene device at Vg = 0V in the temperature 280-200 K. (b) Plot of ln (J0/T2) as a function of 1/T. The barrier height of 0.27 eV at Pd/pentacene interface.

The strongly temperature-dependent *I-V* curves are analyzed with the RS model. Figure 5.12a is a plot of the *lnJ* against $V^{1/2}$ for temperatures above 260-200 K at V_g = 0V. By the similar analysis, what are explained in details in the last section, we calculated a barrier height of

0.27 eV at the SWNT/pentacene interface at V_g = 0V from the slope of $ln\ (J_0/T^2)$ versus $1/T$ plot is shown Figure 5.12b.

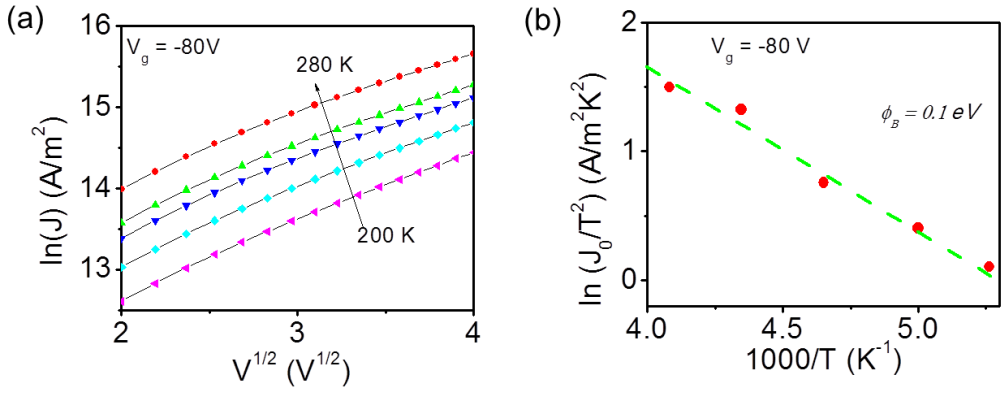

Figure 5.13: (a) $ln(J/T^2)$ versus $V^{1/2}$ plot of a representative SWNT/pentacene device at V_g = -80V. (b) Plot of $ln\ (J_0/T^2)$ as a function of $1/T$. The barrier height of 0.1 eV at Pd/pentacene interface.

The $ln(J/T^2)$ versus $V^{1/2}$ plot of a the SWNT/pentacene device at V_g = -80V is shown in Figure 5.13(a). From the slope of the of $ln\ (J_0/T^2)$ versus $1/T$ (Figure 5.13b) the barrier height is calculated and it is found to be 0.27 eV at Pd/pentacene interface at V_g = 0 V, which is higher than the barrier height of our devices at V_g = - 80V. Therefore, we conclude that barrier height of the SWNT/pentacene interface is decreased with increasing the gate voltage. This is because Fermi level of the pentacene is changed with the gate-voltage which reduced the barrier height at SWNT/pentacene interface.

5.5 Charge Transport Mechanism

Because of significant advancement of organic semiconductor materials synthesis and device engineering, the performance of organic field effect transistors (OFETs) has improved continuously over the last few decades. The performance of the OFETs strongly depends on the

efficient injection of charge carriers from the metal electrodes into organic semiconductors and their transport through the active channel organic semiconductors. However, the charge injection and transport in the OFETs fabricated by polycrystalline organic semiconductors are limited several factors including a large interfacial barriers at the metal/organic semiconductor interface due to Schottky barrier and dipole barriers, trapping states due to grain boundaries at the organic-organic interfaces in the channel, and trapping states in the dielectric/organic semiconductor interfaces[39-50]. In order to improve charge injection in the OFETs recently carbon nanotubes are considering promising electrodes material due to their due extraordinary electronics properties and their pi-pi interaction with the organic semiconductors. Several research groups including our group have shown that performance of the OFETs fabricated with CNT electrodes are improved than that of the device fabricated with conventional metal electrodes.

In the previous section, we have found that the interfacial charge injection barrier at CNT/OSC interface is significantly lower than of the metal/OSC interface. From these studies although it is clear that CNT forms a better interfacial contact is form in between the CNT and organic semiconductors and devices performance is improved with CNT electrodes, the charge transport mechanism in the devices with CNT electrodes is not explored. In order to realize the overall goal of CNT electrode in the OFETs, it is very important to investigate transport in the devices with CNT electrodes.

In this section, we investigate the temperature and gate bias dependent electronic charge transport of the pentacene OFETs with carbon nanotube electrodes with channel length of 2 μm and channel width of 25 μm. We found that mobility of the devices is decreased with decreasing the temperature and the thermally activated mobility can be well explained by multiple trapping and thermal released (MTR) model. The activation energy are decreased with increasing gate-

voltage and the minimum activation energy for pentacene device with CNT electrodes (~ 19 meV) is lower than the activation energy for our control device (~ 41 meV) as well as reported devices with metal electrodes. The low activation energy of the devices with CNT electrodes suggest that trapping state is lower at SWNT/pentacene interface.

5.5.1 Temperature and Voltage Dependent Transport Properties

We measured temperature dependent I-V_g characteristics of our SWNT/pentacene and gold/pentacene devices at different bias voltages. Figure 5.14a and 5.14b show current I -V_g characteristics at bias-voltage (V) = -80V in the temperature range of 300 K to 77 K for of a SWNT/pentacene device and gold/pentacene devices.

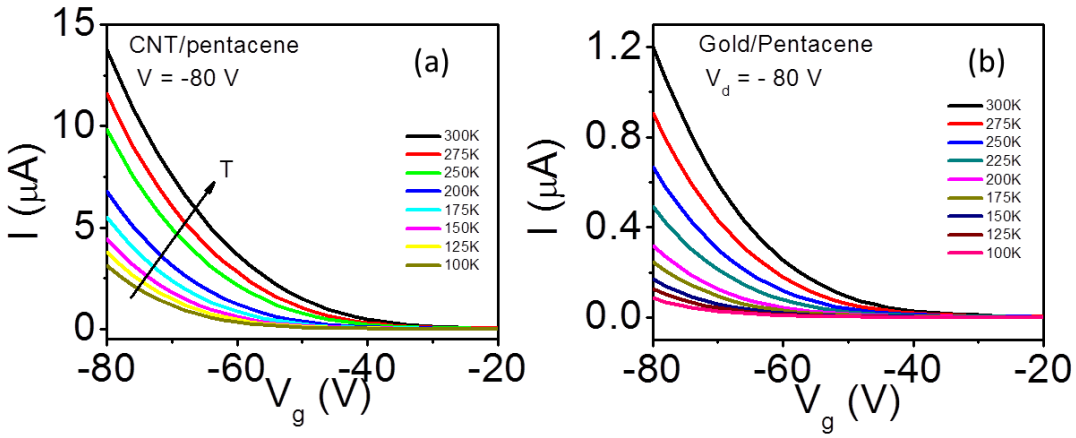

Figure 5.14: Temperature dependent I-V_g characteristics at V = -80V for (a) for SWNT/pentacene OFETs and (b) gold/pentacene OFET.

The I-V_g curves show that they are strongly temperature dependent and the on-current is decreased with decreasing temperature. However, it clearly shows that the on-current of the SWNT/pentacene device is significantly higher than the on current of the gold/pentacene device. The on-current measured at V= -80V and V_g = -80V) for the SWNT/pentacene device 13 µA, whereas it is only 1.2 µA for the gold/pentacene device. The linear mobility of the devices is

calculated using the formula: $\mu = (L/WC_iV)(dI/dV_g)$,where, C_i is the capacitance per unit area of the gate insulator (13.8 nF/cm^2) and dI/dV_g is the slope of the I-V_g curve.

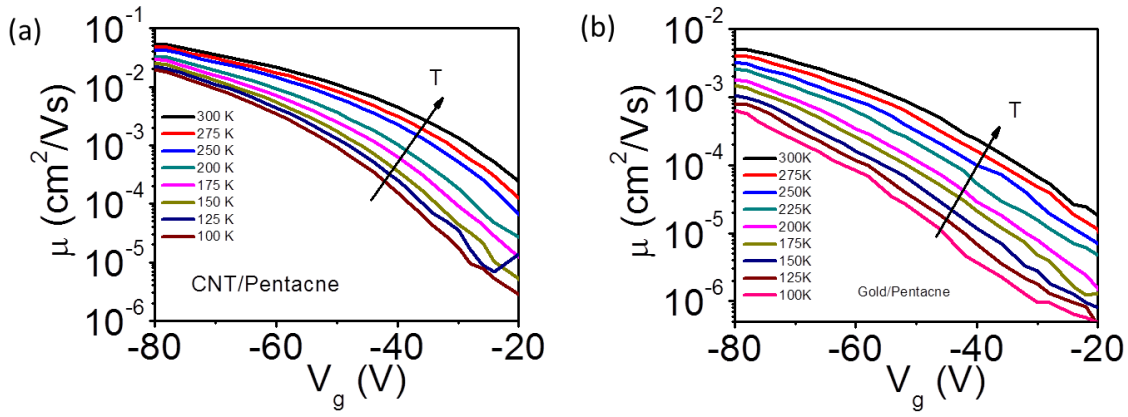

Figure 5.15: Mobility versus gate-voltage at V= -80V in the temperature range of 300K to 77K for (a) SWNT/pentacene and (b) gold/pentacene device.

Figure 5.15a and 5.15b show a plot of the mobility as a function of gate-voltage for a SWNT/pentacene device and gold/pentacene device. These plots show that mobility of the SWNT contacted devices is one order magnitude higher than the gold contacted device. One can easily see from these plots is that as mobility is increased with gate-voltage and mobility can be increased by 5 orders of magnitude by changing the gate-voltage. Similar, the gate-voltage dependent mobility has been observed for amorphous silicon, polycrystalline silicon and organic semiconductors [47, 48, 51]. One possible reason for increasing of the mobility with gate voltage could be due to increase the charge carrier in the channel with increasing gate-voltage. When a larger gate-voltage is applied in the devices, the concentration of the charge carriers in the channel is increased which results in an increase of mobility [45]. Another possible reason could be related to the modulation of the contact resistance of the device with gate-voltage. At lower gate voltage, contact resistance is higher and linear mobility is limited by the contact resistance.

However, the contact resistance of the device is decreased with increasing the gate-voltage [52] and overall device performance is no longer dominated by contact and hence mobility becomes independent of gate-voltage.

5.5.2 Activation Energy of OFETs

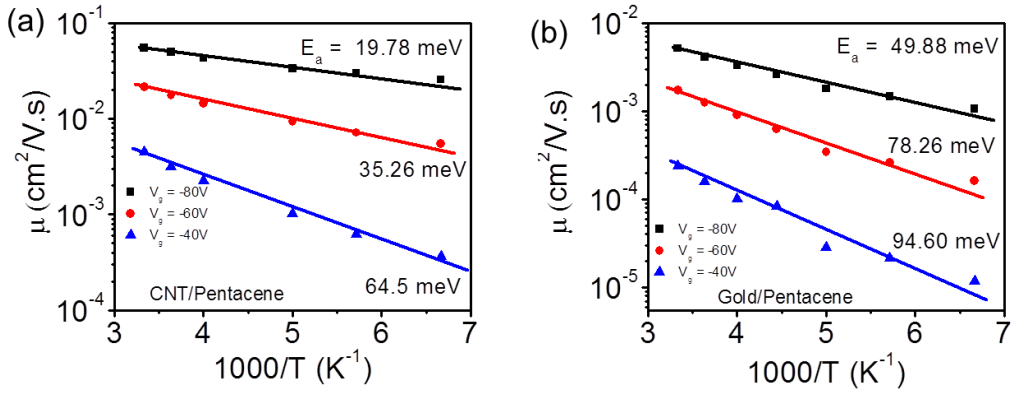

Figure 5.16: Logarithm plot of field effect mobility versus temperature for different gate-voltages for (a) SWNT/pentacene OFETs and (b) gold/pentacene OFETs**.**

We extracted mobility as function of the temperature for fixed gate-voltages. Figure 5.16 (a) and 5.16 (b) show the plots of the extracted mobility versus inverse of temperature at different gate-voltage of the SWNT/pentacene and gold/pentacene devices. As we see from the both of these Figure that mobility is thermally activated over a wide range of temperature for all gate-voltage. The decrease in the mobility with decreasing temperature is an indication of a thermally activated charge transport mechanism in the pentacene devices, and shows that trapping state are in near the band edges and Fermi level does not reach the mobile states. The temperature dependent mobility of our device can be explained using multiple trapping and thermal released (MTR) model [44, 53, 54].

In MTR model, it is assume that the charge carriers are trapped by the shallow or deep traps in the organic semiconductors, and they are released due to thermal activation and contribute to the conduction. We fit the data (solid lines) to the form [44, 53, 54]

$$\mu = \mu_0 exp[-E_a/K_bT] \quad (5.7)$$

where, μ_0 is free carrier mobility, E_a is active energy. Activation energy is the energy difference between the Fermi level and transport level at which charges are able to hop to the next site and kb is Boltzmann constant. By fitting the data with the MTR model we found that activation energy for the SWNT/pentacene devices are 19.78, 35.25 and 64.5meV at V_g of -80, -60 and -40 V respectively. A similar temperature dependent mobility plot for the gold/pentacene devices is shown in Figure 5.16b. The mobility value of the gold/pentacene device is lower than that of the SWNT/pentacene device. In addition, activation energies for the SWNT/pentacene device are 41.28, 61.92 and 79.12, meV at V_g of -80, -60 and -40 V respectively. Therefore activation energy of the SWNT/pentacene device is lower than that of the gold/pentacene device.

In order to further confirm that the activation energy is lower for the devices with SWNT electrodes, we also calculated the activation energy from temperature dependent current data. Figure 5.17(a) and 5.17(b) show logarithm plot of current as function of temperature SWNT/pentacene and gold/pentacene for different gate-voltage. From here we also found that the lnI versus T^{-1} plot are fitted with MTR model and activation energy (E_I) for the SWNT/pentacene device (18.92 meV) is lower than activation energy (E_I) for the CNT/pentacene device (49.88 meV).

Table 5.1 shows a summary of activation energy of our devices which are calculated from mobility data as well as from the current data. In order to understand the effect of gate-voltages on the activation energy as well as to compare the activation energies for the

SWNT/pentacene and gold/pentacene devices, activation energy is plotted as function of gate-voltage (Figure 5.18). This plot clearly shows that activation energy for the SWNT/pentacene devices is lower than that of the activation energy of the gold/pentacene devices for all gate-voltages. It is clearly seen from this table that (i) for a fixed gate-voltage the both E_I and E_μ for the SWNT/pentacene device are lower than that of the gold/pentacene device and (ii) both E_I and E_μ for both the devices are decreasing with increasing gate-voltage. The similar behavior has been reported for the organic transistors with metal electrodes [42, 47].

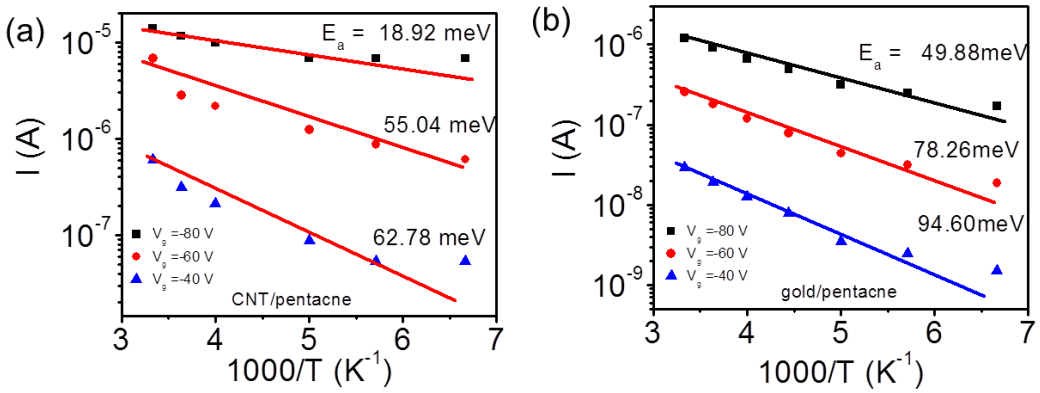

Figure 5.17: Logarithm plot of current versus temperature for different gate-voltages for (a) SWNT/pentacene OFETs and (b) gold/pentacene OFETs.

Table 5.1: Summary of activation energy for CNT/pentacene and gold/pentacene device at different gate-voltages. E_μ and E_I are activation energy calculated from temperature dependent mobility and temperature dependent current. Pn denotes here as pentacene**.**

V_g	-80V		-60V		-40V	
	CNT/Pn	Gold/Pn	CNT/Pn	Gold/Pn	CNT/Pn	Gold/Pn
E_μ(meV)	19.78	41.28	35.26	61.92	64.5	79.12
E_I(meV)	18.92	49.88	55.04	78.26	62.78	94.60

It is worth mentioning that activation energy of our pentacene device with SWNT electrodes is smaller than the reported for pentacene device with standard metal electrodes [43,

46, 55, 56] The activation energy is correlated with trapping state density in the devices. In the polycrystalline organic semiconductors trapping states are originated from disorder of electrode/organic interfaces, dielectric/organic interface, and disorder of grain boundaries in between the crystalline regions in the channel. We used same substrate, dielectric materials, identical electrodes geometry to fabricate the SWNT/pentacene and gold/pentacene devices. In addition, the devices were fabricated in the same deposition and the morphology of the deposited films is found to be similar. Therefore it can be easily assumed that the traps density due to grain boundaries and dielectric/organic interface for both of the SWNT/pentacene and gold/pentacene devices are the same. More importantly, we believe that compared to traps in the channel and dielectric/organic interface, the traps at the electrode/organic interface are larger and they are dominating in our devices. This is because the active channel length of our devices is very small which reduces the number of gain boundaries in the channel. The activation energy of our devices provides insight information of the contact rather than channel material, and low activation energy our SWNT/pentacene device suggests that traps state at the SWNT/pentacene interface is low.

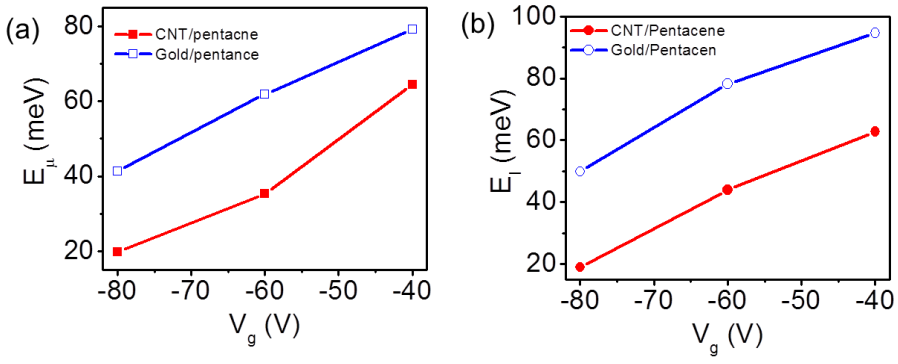

Figure 5.18: Activation energy for the mobility as function of gate voltages for both SWNT/pentacene and gold/pentacene devices. (b) Activation energy for the current as function of gate- voltage for both SWNT/pentacene and gold/pentacene devices.

The large activation energy in the gold contact pentacene device infers that the trapping state at the gold/pentacene is higher. The larger trapping state obtained in the metal/pentacene device are not unexpected. Because the interfacial trap strongly depends on the surface of the electrodes. The electrode roughness has also effect on the morphology of the deposited organic semiconductor. In the case gold electrodes, small and rough- nanocrystalline domain are formed on its surface. The increase of the roughness of the gold electrode surface induces the disoriented growth of organic semiconductor, which leads to large interface disorders [56]. On the other hand, the roughness of SWNT can provides the sites for the nucleation growth of organic material and provides the appropriate energy levels for charge injection. In the previous studies, lower activation energy of ultrathin bismuth selenite field effect transistors is attributed to a small Schottky barrier between metal and bismuth selenite interface. [57]. We also recently showed that Schottky barrier height between pentacene and SWNT interface is lower than the Schottky barrier height at the pentacene and metal. Therefore, a lower barrier height in between SWNT/pentacene interface also supports lower activation energy in our devices.

5.6 Conclusion

The charge injection and transport mechanisms of the SWNT/pentacene devices were investigated by temperature dependent electronic transport measurement. The contact dominated devices (fabricated with 200 nm SWNT electrode) were used to study charge injection mechanism, whereas channel dominated devices (fabricated with 2 μm SWNT electrode) were used to study charge transport mechanism.

From the charge injection study, we found that in the temperature range 300-200 K, the charge injection mechanism is dominated by thermal emission which is well explained by

Richardson Schottky (RS) model. The calculated barrier height at SWNT/pentacene interfaces is smaller than barrier height at metal/pentacene interfaces. We observed a transition from thermal emission to the tunneling mechanism at temperature below 200 K. In addition, at low temperature the current-voltage characteristics show a transition from direct tunneling to Fowler-Nordheim tunneling, which suggests that barrier width at the SWNT/pentacene interface is very low.

From the charge transport study, we found that the thermally activated mobility and charge transport conduction in our device can be explained by multiple trapping and thermal released (MTR) model. The activating energy of the devices are decreased with increasing gate-voltage dependent, and the minimum activation energy for pentacene device with CNT electrodes (~19 meV) is lower than the minimum activation energy for the devices with metal electrodes (~ 41 meV). From the both of transport and charge injection mechanism studies we conclude that CNT electrodes can enhance performance of organic electronic devices due to efficient charge injection and better charge transport in the organic semiconductors.

5.7 References

1. Z. Liu, M. Kobayashi, B. C. Paul, Z. Bao, Y. Nishi, Contact Engineering For Organic Semiconductor Devices Via Fermi Level Depinning At The Metal-Organic Interface. *Phys. Rev. B* **82**, 035311 (2010).

2. L. Burgi, T. J. Richards, R. H. Friend, H. Sirringhaus, Close Look At Charge Carrier Injection In Polymer Field-Effect Transistors. *J. Appl. Phys.* **94**, 6129 (2003).

3. A. K. Thakur, A. K. Mukherjee, D. M. G. Preethichandra, W. Takashima, K. Kaneto, Charge Injection Mechanism Across The Au-Poly(3-Hexylthiophene-2,5-Diyl) Interface. *J. Appl. Phys.* **101**, 104508 (2007).

4. D. J. Gundlach *et al.*, An Experimental Study Of Contact Effects In Organic Thin Film Transistors. *J. Appl. Phys.* **100**, 024509 (2006).

5. J. C. Scott, Metal-Organic Interface And Charge Injection In Organic Electronic Devices. *J. Vac. Sci.Tech. A* **21**, 521 (2003).

6. N. Koch, A. Kahn, J. Ghijsen, J. J. Pireaux, J. Schwartz, R. L. Johnson and A. Elschner, Conjugated Organic Molecules On Metal Versus Polymer Electrodes: Demonstration Of A Key Energy Level Alignment Mechanism. *Appl.Phys. Lett.* **82**, 70 (2003).

7. I. G. Hill, A. Rajagopal, A. Kahn, Y. Hu, Molecular Level Alignment At Organic Semiconductor-Metal Interfaces. *Appl.Phys. Lett.* **73**, 662 (1998).

8. S. Braun, W. R. Salaneck, M. Fahlman, Energy-Level Alignment At Organic/Metal And Organic/Organic Interfaces. *Adv. Mater.* **21**, 1450 (2009).

9. H. Ishii, K. Sugiyama, E. Ito, K. Seki, Energy Level Alignment and Interfacial Electronic Structures at Organic/Metal and Organic/Organic Interfaces. *Adv. Mater.* **11**, 605 (1999).

10. Z. Chiguvare, J. Parisi, V. Dyakonov, Current Limiting Mechanisms In Indium-Tin-Oxide/Poly3-Hexylthiophene/Aluminum Thin Film Devices. *J. Appl. Phys.* **94**, 2440 (2003).

11. S. Barth, U. Wolf, auml, H. ssler, uuml, P. ller, H. Riel, H. Vestweber, P. F. Seidler, Rie, szlig and W., Current Injection From A Metal To A Disordered Hopping System: Comparison Between Experiment And Monte Carlo Simulation. *Phys. Rev. B* **60**, 8791 (1999).

12. J. Appenzeller, M. Radosavljević, J. Knoch, P. Avouris, Tunneling Versus Thermionic Emission in One-Dimensional Semiconductors. *Phys. Rev.Lett.* **92**, 048301 (2004).

13. W. Wang, T. Lee, M. A. Reed, Mechanism Of Electron Conduction In Self-Assembled Alkanethiol Monolayer Devices. *Phys. Rev. B* **68**, 035416 (2003).

14. J. Svensson, E. E. B. Campbell, Schottky Barriers In Carbon Nanotube-Metal Contacts. *J.Appl. Phys.* **110**, 111101 (2011).

15. X. Guo, J. P. Small, J. E. Klare, Y. Wang, M. S. Purewal, I. W. Tam, B. H. Hong, R. Caldwell, L. Huang, S. O'Brien, J. Yan, R. Breslow, S. J. Wind, J. Hone, P. Kim and C. Nuckolls., Covalently Bridging Gaps in Single-Walled Carbon Nanotubes with Conducting Molecules. *Science* **311**, 356 (2006).

16. P. F. Qi, A. Javey, M. Rolandi, Q. Wang, E. Yenilmez and H. J. Dai. Miniature Organic Transistors With Carbon Nanotubes As Quasi-One-Dimensional Electrodes. *J.Am.Chem. Soc.* **126**, 11774 (2004).

17. B. K. Sarker, S. I. Khondaker, High-Performance Short Channel Organic Transistors Using Densely Aligned Carbon Nanotube Array Electrodes. *Appl.Phys. Lett.* **100**, 023301 (2012).

18. B. K. Sarker, J. Liu, L. Zhai, S. I. Khondaker, Fabrication of Organic Field Effect Transistor by Directly Grown Poly(3 Hexylthiophene) Crystalline Nanowires on Carbon Nanotube Aligned Array Electrode. *ACS Appl.Mater.Interfaces.* **3**, 1180 (2011).

19. B.K. Sarker, B. K.; M.R. Islam, F. Alzubi, F.S.I. Khondaker, Fabrication of Carbon Nanotube Electrode for Organic Electronics Devices. *Mater. Express* **1**, 80 (2011).

20. S. L. Hellstrom, R. Z. Jin, R. M. Stoltenberg, Z. Bao, Driving High-Performance n- and p-type Organic Transistors with Carbon Nanotube/Conjugated Polymer Composite Electrodes Patterned Directly from Solution. *Adv. Mater.* **22**, 4204 (2010)

21. C. M. Aguirre, C. Ternon, M. Paillet, P. Desjardins, R. Martel, Carbon Nanotubes as Injection Electrodes for Organic Thin Film Transistors. *Nano Letters* **9**, 1457 (2009).

22. F. Cicoira, C. M. Aguirre, R. Martel, Making Contacts to n-Type Organic Transistors Using Carbon Nanotube Arrays. *ACS Nano* **5**, 283 (2010).

23. C. Chia-Hao, C. Chao-Hsin, Y. Jung-Yen, Pentacene-Based Thin-Film Transistors With Multiwalled Carbon Nanotube Source And Drain Electrodes. *Appl.Phys. Lett.* **91**, 083502 (2007).

24. M. O. Aboelfotoh, C. Fröjdh, C. S. Petersson, Schottky-Barrier Behavior Of Metals On N- And P-Type 6h-Sic. *Phys. Rev. B* **67**, 075312 (2003).

25. J. H. Worne, J. E. Anthony, D. Natelson, Transport In Organic Semiconductors In Large Electric Fields: From Thermal Activation To Field Emission. *Appl.Phys. Lett.* **96**, 053308 (2010).

26. M. Araidai, M. Tsukada, Theoretical Calculations Of Electron Transport In Molecular Junctions: Inflection Behavior In Fowler-Nordheim Plot And Its Origin. *Phys. Rev. B* **81**, 235114 (2010).

27. J. M. Beebe, B. Kim, J. W. Gadzuk, C. Daniel Frisbie, J. G. Kushmerick, Transition From Direct Tunneling To Field Emission In Metal-Molecule-Metal Junctions. *Phys. Rev.Lett.* **97**, 026801 (2006).

28. S. Shekhar, P. Stokes, S. I. Khondaker, Ultrahigh Density Alignment of Carbon Nanotube Arrays by Dielectrophoresis. *ACS Nano* **5**, 1739 (2011).

29. G. Horowitz, Tunneling Current in Polycrystalline Organic Thin-Film Transistors. *Adv. Funct. Mater.* **13**, 53 (2003).

30. G. Horowitz, M. E. Hajlaoui, Mobility In Polycrystalline Oligothiophene Field-Effect Transistors Dependent On Grain Size. *Adv. Mater.* **12**, 1046 (2000).

31. P. G. Schroeder, C. B. France, J. B. Park, B. A. Parkinson, Orbital Alignment and Morphology of Pentacene Deposited on Au(111) and SnS2 Studied Using Photoemission Spectroscopy. *The Journal of Physical Chemistry B* **107**, 2253 (2003).

32. L. Diao, C. D. Frisbie, D. D. Schroepfer, P. P. Ruden, Electrical Characterization Of Metal/Pentacene Contacts. *J.Appl. Phys.* **101**, 014510 (2007).

33. S. Lee, G. Jo, S.-J. Kang, G. Wang, M. Choe, W. Park, D.-Y. Kim, Y. H. Kahng and T. Lee, Enhanced Charge Injection in Pentacene Field-Effect Transistors with Graphene Electrodes. *Adv. Mater.* **23**, 100 (2011).

34. A. Javey, J. Guo, Q. Wang, M. Lundstrom, H. J. Dai, Ballistic Carbon Nanotube Field-Effect Transistors. *Nature* **424**, 654 (2003).

35. W. Osikowicz, M. P. d. Jong, S. Braun, C. Tengstedt, M. Fahlman and W. R. Salaneck, Energetics At Au Top And Bottom Contacts On Conjugated Polymers. *Appl.Phys. Lett.* **88**, 193504 (2006).

36. I. A. Hummelgen, L. S. Roman, F. C. Nart, L. O. Peres, E. L. d. Sa, Polymer And Polymer/Metal Interface Characterization Via Fowler-Nordheim Tunneling Measurements. *Appl.Phys. Lett.* **68**, 3194 (1996).

37. J. J. Chiu, C. C. Kei, T. P. Perng, W. S. Wang, Organic Semiconductor Nanowires for Field Emission. *Adv. Mater.* **15**, 1361 (2003).

38. M. Koehler, I. A. Hummelgen, Temperature Dependent Tunnelling Current At Metal/Polymer Interfaces-Potential Barrier Height Determination. *Appl.Phys. Lett.* **70**, 3254 (1997).

39. I. I. Fishchuk, A. K. Kadashchuk, J. Genoe, M. Ullah, H. Sitter, T. B. Singh, N. S. Sariciftci, auml and H. ssler, Temperature Dependence Of The Charge Carrier Mobility In Disordered Organic Semiconductors At Large Carrier Concentrations. *Phys. Rev. B* **81**, 045202 (2010).

40. L. Pan, Z. Sun, Temperature Dependent Conductive Behavior Of Pentacene In Organic Field-Effect Transistor. *Current Appl. Phys.* **9**, 1351 (2009).

41. B. H. Hamadani, D. Natelson, Temperature-Dependent Contact Resistances In High-Quality Polymer Field-Effect Transistors. *Appl.Phys. Lett.* **84**, 443 (2004).

42. D. Guo, T. Miyadera, S. Ikeda, T. Shimada, K. Saiki, Analysis Of Charge Transport In A Polycrystalline Pentacene Thin Film Transistor By Temperature And Gate Bias Dependent Mobility And Conductance. *J. Appl. Phys.* **102**, 023706 (2007).

43. S. F. Nelson, Y.-Y. Lin, D. J. Gundlach, T. N. Jackson, Temperature-Independent Transport In High-Mobility Pentacene Transistors. *Appl.Phys. Lett.* **72**, 1854 (1998).

44. L. Dunn, A. Dodabalapur, Temperature Dependent Transient Velocity And Mobility Studies In An Organic Field Effect Transistor. *J. Appl. Phys.* **107**, 113714 (2010).

45. D. Natali, M. Caironi, Charge Injection in Solution-Processed Organic Field-Effect Transistors: Physics, Models and Characterization Methods. *Adv. Mater.* **24**, 1357 (Mar, 2012).

46. F. Yan, Y. Hong, P. Migliorato, Temperature Dependent Characteristics Of All Polymer Thin-Film Transistors Based On Poly(9,9-Dioctylfluorene-Co-Bithiophene). *J. Appl. Phys.* **101**, 064501 (2007).

47. D. Knipp, R. A. Street, A. R. Volkel, Morphology And Electronic Transport Of Polycrystalline Pentacene Thin-Film Transistors. *Appl.Phys. Lett.* **82**, 3907 (2003).

48. G. Horowitz, M. E. Hajlaoui, R. Hajlaoui, Temperature And Gate Voltage Dependence Of Hole Mobility In Polycrystalline Oligothiophene Thin Film Transistors. *J. Appl. Phys.* **87**, 4456 (2000).

49. T. Minari, T. Nemoto, S. Isoda, Temperature And Electric-Field Dependence Of The Mobility Of A Single-Grain Pentacene Field-Effect Transistor. *J. Appl. Phys.* **99**, 034506 (2006).

50. D. Knipp, R. A. Street, A. Volkel, J. Ho, Pentacene Thin Film Transistors On Inorganic Dielectrics: Morphology, Structural Properties, And Electronic Transport. *J. Appl. Phys.* **93**, 347 (2003).

51. M. Shur, M. Hack, J. G. Shaw, A New Analytic Model For Amorphous Silicon Thin-Film Transistors. *J. Appl. Phys.* **66**, 3371 (1989).

52. G. Horowitz, R. Hajlaoui, D. Fichou, A. E. Kassmi, Gate Voltage Dependent Mobility Of Oligothiophene Field-Effect Transistors *J. Appl. Phys.* **85**, 3202 (1999).

53. C. Tanase, E. J. Meijer, P. W. M. Blom, D. M. de Leeuw, Unification of the Hole Transport in Polymeric Field-Effect Transistors and Light-Emitting Diodes. *Phy. Rev.Lett.* **91**, 216601 (2003).

54. H. S. Kang *et al.*, Electrical characteristics of pentacene-based thin film transistor with conducting poly(3,4-ethylenedioxythiophene) electrodes. *J. Appl. Phys.* **100**, 064508 (2006).

55. V. Y. Butko, X. Chi, D. V. Lang, A. P. Ramirez, Field-effect transistor on pentacene single crystal. *Appl.Phys. Lett.* **83**, 4773 (2003).

56. A. A. Virkar, S. Mannsfeld, Z. Bao, N. Stingelin, Organic Semiconductor Growth and Morphology Considerations for Organic Thin-Film Transistors. *Adv.Mater.* **22**, 3857 (2010).

57. S. Cho, N. P. Butch, J. Paglione, M. S. Fuhrer, Insulating Behavior in Ultrathin Bismuth Selenide Field Effect Transistors. *Nano Lett.* **11**, 1925 (2011)

CHAPTER 6: FABRICATION OF ORGANIC NANOWIRE TRANSISTORS WITH CARBON NANOTUBE ELECTRODES BY INTERFACE ENGINEERING*

6.1 Introduction

The device performance of organic field effect transistors (OFET) is currently limited by the contact resistance between metal electrodes and organic semiconductors as well as the morphology of the semiconducting channel materials because of their highly anisotropic charge transport characteristics [1-4]. Contact resistance depends on the morphology of the interface, electrode work function, and dipole formation between electrodes and organic materials [3, 5-7]. On the other hand, the nano-scale morphology of the organic semiconductors such as conjugated polymers is extremely sensitive to the polymer's molecular weights, the solvent to dissolve the polymer and cast films from, and the substrate treatments [8, 9]. For example, the typical field effect charge mobility value for the most common solution processed conjugated polymer, poly(3-hexylthiophne) (P3HT), varies by several orders of magnitude depending upon the applied processing parameters [4, 5]. Therefore, high performance OFETs can be fabricated by designing new device architecture to improve the electrode/semiconductor contact for better charge injection and the morphology of the semiconductor for enhance charge mobility, where appropriate source and drain (S/D) electrode materials with excellent contact and highly ordered crystalline organic semiconducting materials hold the key.

Single walled carbon nanotubes (SWNTs) are a promising candidate for electrode materials in OFETs due to their unique electrical properties [10, 11]. The work function of SWNT thin films is in the range of 4.7-5.2 eV [12] which is well aligned with the HOMO

* Portions of this chapter have been published in the following journals: ***ACS Appl. Mater. Interfaces*** *3, 1180 (2011).*

(highest occupied molecular orbital) level of many conjugated polymers including P3HT (1). In addition, the π-π interaction between SWNTs and the conjugated polymers is expected to result in better charge injection. A few research groups have reported the fabrication of OFETs using individual SWNT [13, 14] randomly oriented SWNT network [15-17], and SWNT/polymer composite film [18, 19] as electrodes. In all of these studies, the organic materials were deposited by spin coating, drop casting or by thermal evaporation which resulted in poor morphology. Despite the conceptual advantages and attractive features of SWNTs as an electrode material, so far the performance of the OFET using SWNT electrodes did not demonstrate any improvement compared to that of conventional OFET fabricated with standard metal electrodes probably because of poorly defined crystalline structure of semiconductor materials.

One potential key step of improving the OFET device performance could be the direct growth of crystalline conjugated polymer such as P3HT nanowires on the SWNT electrodes to improve the electrode/semiconductor interface and the morphology of semiconductor. Compared to the OFETs from solution cast P3HT films, OFETs from crystalline P3HT nanostructures is expected to show improved mobility attributed to their increased interchain stacking with overlapped π-π orbital and unique crystalline structure and morphology [20-24]. In addition, the surface treatments or other processing parameters will not have significant impact on the crystalline structures of P3HT since the ordered nano-scale morphology is developed during the growth process. In such devices, the strong π-π interaction between SWNTs and the polymer nanowires will enhance the charge carrier injection from SWNT electrode to crystalline nanowires. In addition, the polymer nanowires will eliminate the crystal domain boundaries in thin films and improve the charge carrier transport through the channel along the one dimensional supramolecular self-organized structures [20].

In this chapter, we demonstrate a bottom up approach to fabricate OFETs by growing P3HT crystalline nanowires on solution processed aligned array SWNT interdigitated electrodes which exploit strong π-π interaction for both efficient charge injection and transport. Ultra-high density SWNTs were aligned from their aqueous solutions via dielectrophoresis (DEP), while electron beam lithography (EBL) and oxygen plasma etching technique was used to define the SWNT electrode pattern. The P3HT crystalline nanowires were directly grown from SWNT surface to connect the SWNT electrodes. For comparison of device properties, control OFETs of P3HT nanowires deposited on gold electrodes were also fabricated. Electron transport measurements on 28 devices showed that, compared to the OFETs with gold electrodes, the OFETs with SWNT electrodes have shown better mobility and better current on-off ratio with a maximum of 0.13 cm^2/Vs and 3.1×10^5 respectively. The improved device characteristics with SWNT electrodes were also demonstrated by the improved charge injection and the absence of short channel effect which was dominant in gold electrode OFETs. Such remarkable enhancement of the device performance as high mobility, high current on-off ratio, absence of short channel effect and better charge carrier injection can be attributed to the improved contact via strong π-π interaction between SWNT electrodes and the crystalline P3HT nanowires as well as the improved morphology of P3HT due to one dimensional crystalline structure.

6.2 Experimental Methods

6.2.1 Fabrication of CNT Interdigitated Electrodes

The fabrication of interdigitated nanotube electrodes is the same procedure for fabrication of the CNT electrodes (except the design of the electrode itself). The interdigitated nanotube electrodes fabrication procedures are illustrated in Figure 6.1a. The details of the CNT electrodes fabrication are explained in the Chapter 4. At first, SWNT were aligned between the Pd patterns

using DEP[25-29]. Highly purified, stable and surfactant free SWNT aqueous solution was obtained from Brewer Science Inc (30) and used for the CNT electrode fabrication. Details of the SWNT alignment and characterization can be found in our recent report [31]. After SWNT alignment, PMMA was spin coated on the samples and interdigitated CNT electrodes are fabricated using the electron beam lithography (EBL) and followed by plasma etching. The scanning electron microscopy (SEM) image of a part of the integrated electrodes is shown in Figure 6.1b. For control experiment, gold interdigitated electrodes were also fabricated with the same geometry of SWNT electrodes by EBL and thermal deposition of gold and standard lift off. All of the OFET devices in this experiment had channel length (*L)* of 1 µm and total channel width (*W)* of 40 µm.

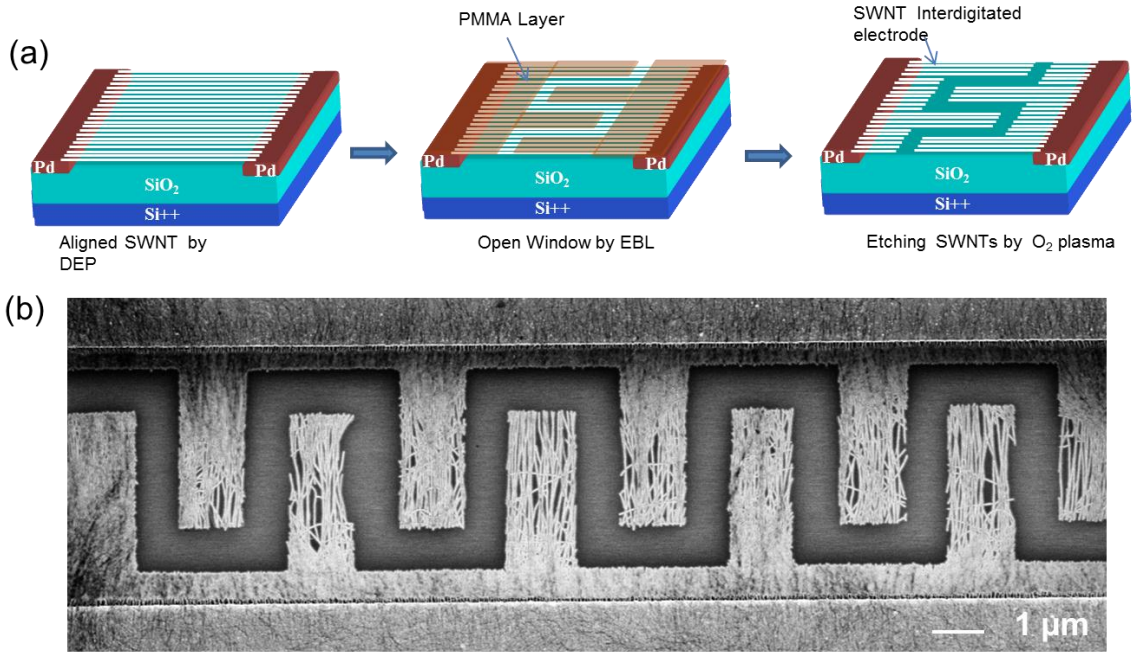

Figure 6.1: (a) Schematics of SWNT aligned array interdigitated electrode fabrication. (b) SEM image of a part of SWNT interdigitated electrode.

6.2.2 Growth of Organic Nanowire on CNT Interdigitated Electrodes

P3HT and anisole were purchased from Rieke Metals, Inc and Acros Organics (New Jersey, USA) respectively and used as received. In this experiment, no additional surface treatment such as octadecyltrichlorosilane (OTS) or hexamethyldisilazane (HMDS) was performed on SiO_2 surface. P3HT powder was dissolved in anisole with a concentration of 0.25 mg/mL at 90 ^{o}C in a glass vial. One chip of SWNT electrode was then immersed inside the P3HT solution, which was cooled down to room temperature at a rate ~ 20 ^{0}C/hour and kept 12 hours for P3HT crystallization.

6.2.3 Characterization of Devices

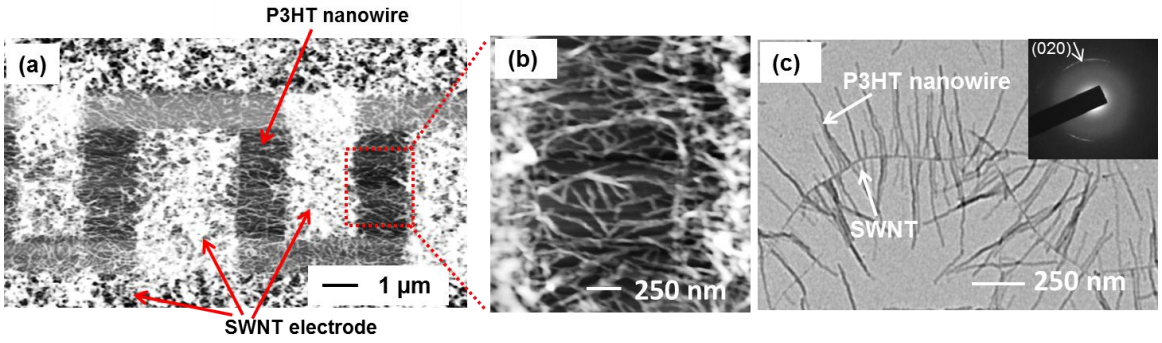

Figure 6.2: (a) AFM image of P3HT nanowire growth on SWNT interdigitated electrodes (This image represents only a part of the device). (b) High magnification image of Figure (a). (c) TEM images of P3HT nanowires growth on SWNT surface. Inset in (c): Selected area electron diffraction (SAED) pattern of the nanowires.

Tapping mode atomic force microscopy (AFM) images were acquired by Dimension 3100 AFM (Veeco). The scanning electron microscopy (SEM) images were taken using Zeiss Ultra -55 SEM with an accelerating voltage 1 kV. Raman spectroscopy was performed using a Renishaw InVia Raman microscope comprised of a laser (532 nm line of solid Si laser), a single spectrograph fitted with holographic notch filters, and an optical microscope (a Leica microscope

with a motorized XYZ stage) rigidly mounted and optically coupled to the spectrograph. The spectrometer was calibrated with a Si standard using a Si band position at 520.3 cm^{-1}. The electrical transport measurements of SWNT array were carried out by DL instruments 1211 current preamplifier and a Keithley 2400 source meter interfaced with LabView program. The OFET characteristics were measured using Hewlett-Packed (HP) 4145B semiconductor parametric analyzer connected to a probe station inside an enclosed glove box system filled with nitrogen gas.

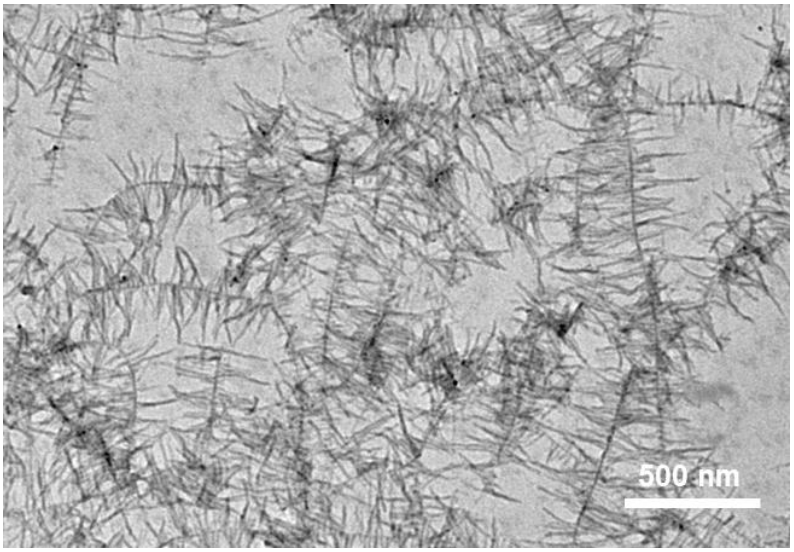

Figure 6.3: TEM images of P3HT supramolecular structures on SWNT. This shows that P3HT nanowires crystallize on the SWNT surface.

Figure 6.1b shows a SEM image of a part of the fabricated SWNT electrode with well-defined channel length L = 1 μm. For channel width, we considered all contributions including channel between parallel SWNT fingers as well as channel between the SWNT fingers and SWNT base. The total channel width were W = 40 μm giving a W/L ratio of 40. After the oxygen plasma etching, we measured the I_d - V_d again and found the current to be in the pico-ampere range suggesting that no SWNT was left in the channel. The interdigitated electrode

patterns were chosen in this work because the interdigitated patterns provide maximum surface area for the growth of P3HT nanowires. In addition, the interdigitated electrodes can increase the output current by increasing the channel width while keeping the device size small.

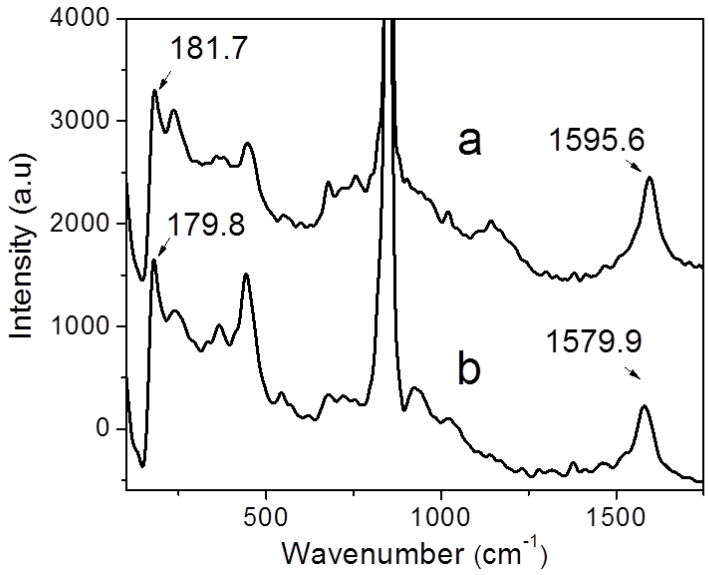

Figure 6.4: Raman scattering spectra of (a) SWNTs with P3HT nanowires, and (b) pristine SWNTs

The unique feature of our OFET fabrication using SWNT electrodes is the direct growth of crystalline P3HT nanowires in between SWNT interdigitated electrodes by a bottom up approach [23]. When the chip containing SWNT electrodes was immersed into the hot P3HT solution and allowed to cool down to room temperature, it induced the crystallization of P3HT in the solution to form 1D nanowire-like crystals [24]. Since SWNTs function as the nucleation cores for P3HT through the π-π interactions, P3HT nanowires grow from the surface of SWNTs [23], generating the interconnections (P3HT nanowire network) among the SWNTs in the electrodes. The AFM images (Figure 6.2a and 6.2b) clearly show that the P3HT nanowires connect SWNT source and drain interdigitated electrodes. Since P3HT nucleates on all the

SWNTs, the brighter part represents SWNT electrodes while the relatively darker part represents the channel. For a control experiment, individually dispersed SWNTs (not in the electrode form) were also placed in the P3HT solution under the same condition.

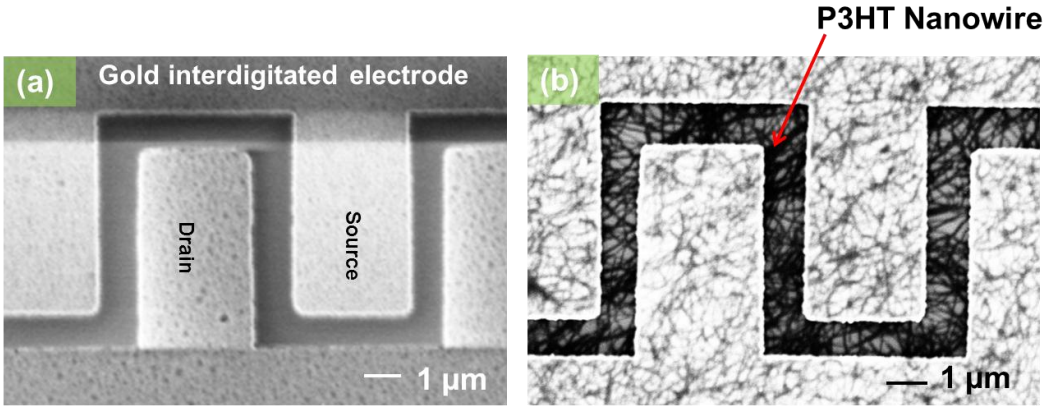

Figure 6.5: (a) SEM image of a representative gold interdigitated electrode (control electrode).The geometry and dimension of this electrode are the same as that of SWNT interdigitated electrode, i.e: channel length L=1 µm and channel width W = 40 µm. (b) SEM image of the P3HT nanowire OFET with gold interdigitated electrode. Unlike SWNT electrode, here the nanowires get deposited on the gold electrode.

The transmission electron microscopy (TEM) images of this growth (Figure 6.2c and Figure 6.3) show that the P3HT nanowires grow from nanotube surfaces and no free P3HT nanowires were observed in the solution. The obtained selected area electron diffraction (SAED) patterns of these nanowires (inset in Figure 6.2c) show the (020) reflection (d = 0.38±0.01 nm), confirming that the polymer chains were well-stacked perpendicularly to the nanowire long axis (direction of π-π interaction). In addition, Raman spectra of SWNTs and SWNTs with P3HT nanowires (see Figure 6.4) indicates the molecular level interaction between SWNT and P3HT, suggesting good contact between two materials. Gold interdigitated electrodes (Figure 6.5) with the same architecture as SWNT electrodes were also immersed into the P3HT hot anisole solutions to check the growth of P3HT nanowires on the gold electrodes. Since there is no

interaction between gold electrodes and P3HT, it is not surprising to find out that P3HT form nanowires in the cooled solution and deposit randomly on the gold electrodes (Figure 6.5). The gold electrode OFET with similar P3HT coverage density as the SWNT electrode OFET was fabricated for comparison of device characteristics. A total of 14 OFET devices with SWNT electrodes and 14 OFET devices with gold electrodes were studied.

6.3 Transport Properties of Organic Nanowire Transistors

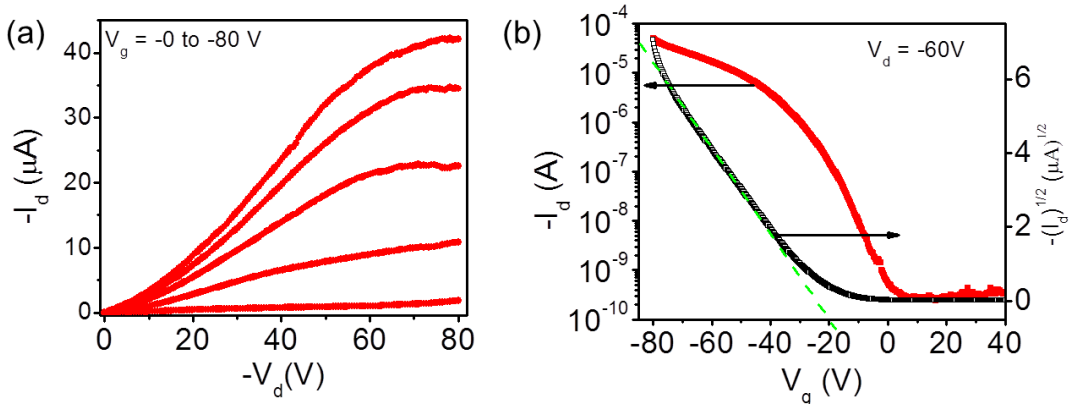

Figure 6.6: (a) Output characteristics of a representative P3HT-nanowire OFET with SWNT interdigitated electrodes with dimension of L =1 μm and W= 40 μm, fabricated on a Si/SiO_2 substrate with an oxide thickness of 250 nm. (b) Transfer curve of the same OFET showing the current on-off ratio (I_{on}/I_{off}) of 3.1×10^5.

The output characteristics (I_d - $V_{d)}$ of a representative OFET device with SWNT electrodes shows excellent gate modulation along with current saturation (Figure 6.6a). The transfer characteristic (I_d - V_g) of the same device at a fixed V_d= - 60 V (Figure 6.6b) shows the current varies over five orders of magnitude (I_{on}/I_{off} = 3.1×10^5) with a threshold voltage (V_T) of -20V. The saturation mobility (μ_{sat}) and linear mobility (μ_{lin}) of the OFET devices were calculated using the following standard formulas

$$\mu_{sat}=I_{d,sat}(2L/WC_i)(1/(V_g-V_T)^2) \quad (6.1)$$

$$\mu_{lin}= (L/WC_iV_d)(dI_d/dV_g) \quad (6.2)$$

where, C_i is the capacitance per unit area of the gate insulator (13.8 nF/cm^2) [1]. The μ_{sat} and μ_{lin} of this device were 0.065 cm^2/Vs and 0.04 cm^2/Vs respectively. From the AFM images, it is estimated that the OFET channel is ~50% covered by P3HT nanowires, giving an effective channel width of 20 µm. Using this effective channel width, the calculated effective saturation and linear mobility were 0.13 and 0.08 cm^2/Vs, respectively. All 14 studied SWNT electrode OFET devices have shown similar saturation behavior with effective μ_{sat} varying from 0.03 to 0.13 cm^2/Vs (average μ_{sat} = 0.07±0.03 cm^2/Vs), with corresponding I_{on}/I_{off} varying from 7.1× 10^3 to 3.1× 10^5. The maximum mobility (0.13 cm^2/Vs) of the fabricated devices is one order of magnitude higher than the previous reported values of P3HT film OFET spin coated on the carbon nanotube electrode [16]. This is rather impressive considering the fact that no surface treatment was performed on our devices. The reason for the improved mobility of our P3HT nanowire OFETs with SWNT electrode is due to highly ordered crystalline nanowire form of the P3HT which provide better charge transport pathways, as well as direct growth of these nanowires on the surface of nanotube electrode which provides better interface.

6.4 Comparison of Device Performances

We have also measured control P3HT nanowire OFETs with gold interdigitated electrodes. Output characteristics of one of our best P3HT-nanowire OFET with gold interdigitated electrode is shown in Figure 6.7a. The output current shows parabolic behavior with voltage without showing any saturation, typical of space charge limited conduction and has been commonly observed in short channel metal electrode OFETs [32-34]. The parabolic

behavior indicates the presence of an interfacial barrier at P3HT/gold interface. The transfer characteristics of the same device is presented in Figure 6.7b measured in the linear regime (V_d = - 40V) which show a current on-off ratio 2.6×10^4. Since the output curve is not saturated, we only calculated effective linear mobility μ_{lin} = 0.045 cm^2/Vs for this device by considering ~50% coverage (Figure 6.5). Of the 14 devices that we measured using gold electrodes, majority of them showed short channel behavior with μ_{lin} varying from 0.001 to 0.045 cm^2/Vs (average μ_{lin} = 0.02±0.01 cm^2/Vs). The corresponding I_{on}/I_{off} of the devices varies from 10 to 3×10^4. Figure 6.8 shows a summary of the device characteristics for all SWNT electrode OFETs and gold electrode OFETs. From here, we see that while SWNT electrode OFETs have shown an improved and more consistent device performance, gold electrode OFETs show a larger variation in performance. This again shows that how short channel effect dominates gold electrode OFETs.

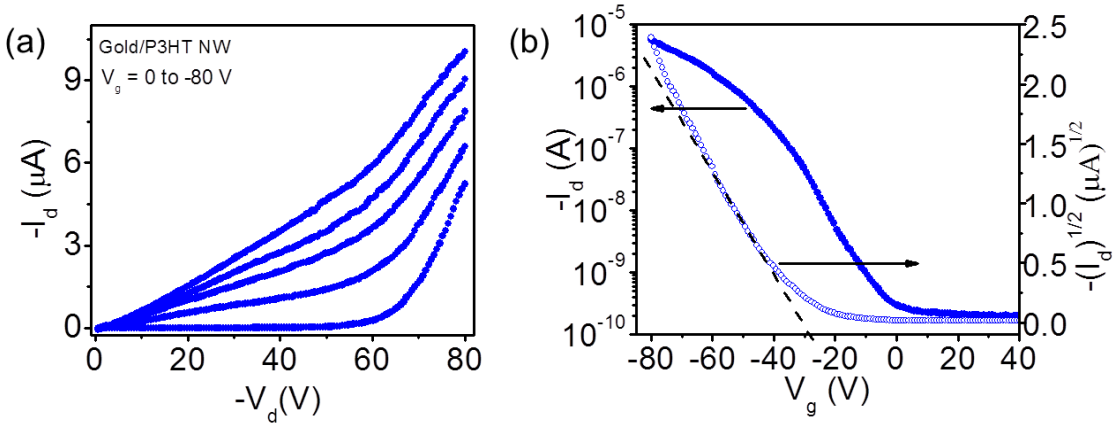

Figure 6.7: (a) Output characteristics of the best P3HT-nanowire OFET device with gold interdigitated electrodes (b) Transfer curve of the same device.

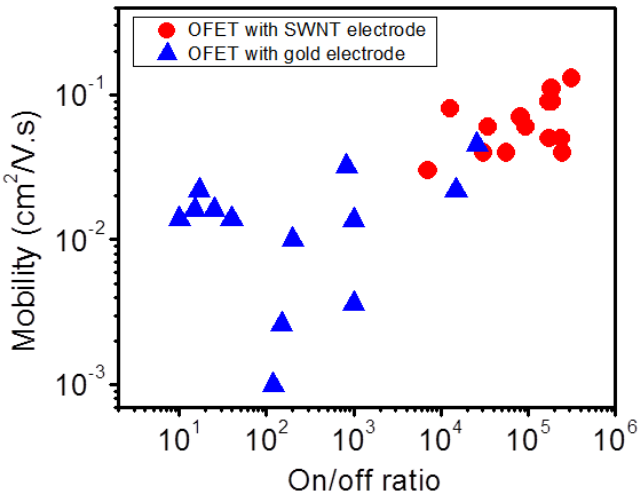

Figure 6.8: Mobility as function of corresponding current on-off ratio of 14 SWNT/P3HT nanowire OFETs as well as 14 gold/P3HT nanowire OFETs. Mobility values and their corresponding current on-off ratios of the OFETs with SWNT electrode are more consistence and higher than the OFETs with gold electrodes.

It is well known that when L is less than 10 times the oxide thickness (t_{ox}), the device performance is dominated by the short channel effect [1, 3, 32-34] which manifests as parabolic behavior of output current without saturation and high off current. Therefore, the observed short channel effect in the gold electrode OFET (t_{ox} = 250 nm, L=*1* µm) is as-expected. Since I_{on}/I_{off} depends on L according to

$$I_{on}/I_{off} = (4C_i/9t_{ox}\varepsilon\varepsilon_0)L^2 \quad (6.3)$$

where, ε_0 is the vacuum permittivity and ε is the dielectric constant of channel insulator [35], it is very difficult to achieve perfect transistor behavior and high I_{on}/I_{off} in a short channel OFET. It is, however, interesting to observe that the OFET with SWNT electrodes (same L and t_{ox}) did not show any short channel effect, instead it showed perfect saturation with high I_{on}/I_{off} (Figure 6.6a and 6.6b*)*. Such observation is significant because the short channel effect is a major bottleneck in reducing the device size for high performance OFETs. It is believed that the better contact

between P3HT nanowires and SWNT electrodes as well as the improved morphology of the channel material due to their crystalline nanowire structures eliminated the short channel effect. To investigate the role of P3HT/SWNT electrode contact in the charge injection into the P3HT nanowires, low bias output characteristics with zero and -60V gate voltage was plotted for both SWNT and gold electrodes (Figure 6.9a and 6.9b). From these curves, it is clear that the OFET with SWNT electrodes provides more output current than that with gold electrode under the same applied voltage.

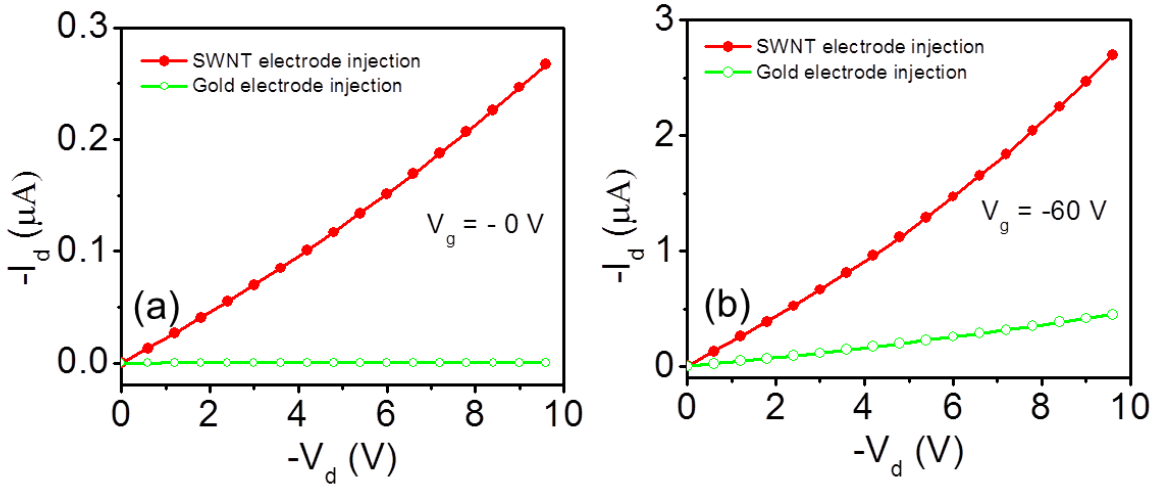

Figure 6.9: Comparison of charge injection from SWNT electrode and gold electrode into the P3HT nanowires at low bias (V_d = -10V) and with a gate voltage (a) V_g = 0 V and (b) V_g = - 60 V. The both curves shows that compare to gold electrode, SWNT electrodes provides a higher drain current due to a better charge injection.

The remarkable improvement of the device performance including high mobility, high current on-off ratio, the absence of short channel effect and better charge carrier injection can be attributed to the improved contact between aligned array SWNT electrodes with the crystalline P3HT nanowires as well as improved morphology of P3HT. The SWNTs and P3HTs share the same conjugated carbon hexagonal ring structure, and strong π-π interaction exists between P3HT nanowires and SWNTs. This makes excellent interfacial contact between P3HT nanowires

and SWNTs and leads to efficient charge carrier injection from SWNT electrodes to P3HT nanowires. The highly ordered P3HT nanowires reduce the gain boundaries in the channel, provide the high current conducting path between nanotube S/D electrodes, and enhanced the hole mobility in the device [4, 5, 20-22].

6.5 Conclusion

We demonstrated new device architecture for high performance OFET fabrication using the direct growth of crystalline P3HT nanowires on SWNT interdigitated electrodes. Compared to the OFETs with metal electrodes, the devices with SWNT electrodes have shown consistently high mobility and high current on-off ratio with a maximum of 0.13 cm^2/Vs and 3.1×10^5, respectively. The improved device characteristics were also demonstrated by the absence of short channel effect which was dominant in gold electrode OFETs. Such remarkable improvement of the device performance as high mobility, high current on-off ratio, absence of short channel effect and better charge carrier injection can be attributed to the improved contact via strong π-π interaction SWNT electrodes with the crystalline P3HT nanowires as well as the improved morphology of P3HT due to one dimensional crystalline structure. Our results presented here will have significant impact on the development of high performance organic electronic devices.

6.6 References

1. J. Zaumseil, H. Sirringhaus, Electron and Ambipolar Transport in Organic Field-Effect Transistors. *Chem. Rev.* **107**, 1296 (2007).

2. A. A. Virkar, S. Mannsfeld, Z. Bao, N. Stingelin, Organic Semiconductor Growth and Morphology Considerations for Organic Thin-Film Transistors. *Adv. Mater.* **22**, 3857 (2010)

3. L. Burgi, T. J. Richards, R. H. Friend, H. Sirringhaus, Close Look At Charge Carrier Injection In Polymer Field-Effect Transistors. *J. Appl. Phys.* **94**, 6129 (2003).

4. M. Surin, L. Ph, R. Lazzaroni, J. D. Yuen, G. Wang, D. Moses, A. J. Heeger, S. Cho and K. Lee, Relationship Between The Microscopic Morphology And The Charge Transport Properties In Poly(3-Hexylthiophene) Field-Effect Transistors. *J. Appl. Phys.* **100**, 033712 (2006).

5. K. A. Singh, G. Sauve, R. Zhang, T. Kowalewski, R. D. McCullough and L. M. Porter, Dependence Of Field-Effect Mobility And Contact Resistance On Nanostructure In Regioregular Poly(3-Hexylthiophene) Thin Film Transistors. *App. Phys. Lett.* **92**, 263303 (2008).

6. N. Koch, A. Kahn, J. Ghijsen, J. J. Pireaux, J. Schwartz, R. L. Johnson and A. Elschner Conjugated Organic Molecules On Metal Versus Polymer Electrodes: Demonstration Of A Key Energy Level Alignment Mechanism. *App. Phys. Lett.* **82**, 70 (2003).

7. I. G. Hill, A. Rajagopal, A. Kahn, Y. Hu, Molecular Level Alignment At Organic Semiconductor-Metal Interfaces. *App. Phys. Lett.* **73**, 662 (1998).

8. R. J. Kline, M. D. McGehee, E. N. Kadnikova, J. Liu, J. M. J. Fréchet and M. F. Toney., Dependence of Regioregular Poly(3-hexylthiophene) Film Morphology and Field-Effect Mobility on Molecular Weight. *Macromolecules* **38**, 3312 (2005)

9. S. Kobayashi, T. Nishikawa, T. Takenobu, S. Mori, T. Shimoda, T. Mitani, H. Shimotani, N. Yoshimoto, S. Ogawa and Y. Iwasa, Control Of Carrier Density By Self-Assembled Monolayers In Organic Field-Effect Transistors. *Nature Mater.* **3**, 317 (2004)

10. X. Guo, J. P. Small, J. E. Klare, Y. Wang, M. S. Purewal, I. W. Tam, B. H. Hong, R. Caldwell, L. Huang, S. O'Brien, J. Yan, R. Breslow, S. J. Wind, J. Hone, P. Kim and C. Nuckolls., Covalently Bridging Gaps in Single-Walled Carbon Nanotubes with Conducting Molecules. *Science* **311**, 356 (2006).

11. P. F. Qi, A. Javey, M. Rolandi, Q. Wang, E. Yenilmez and H. J. Dai, Miniature Organic Transistors With Carbon Nanotubes As Quasi-One-Dimensional Electrodes. *J.Am.Chem. Soc.* **126**, 11774 (2004).

12. L. Hu, D. S. Hecht, G. Gruener, Carbon Nanotube Thin Films: Fabrication, Properties, and Applications. *Chem. Rev*. **110**, 5790 (2010).

13. C. M. Aguirre, C. Ternon, M. Paillet, P. Desjardins, R. Martel, Carbon Nanotubes as Injection Electrodes for Organic Thin Film Transistors. *Nano Lett.* **9**, 1457 (2009).

14. K. Tsukagoshi, I. Yagi, Y. Aoyagi, Pentacene Nanotransistor With Carbon Nanotube Electrodes. *App. Phys. Lett.* **85**, 1021 (2004).

15. C.-H. Chang, C.-H. Chien, J.-Y. Yang, Pentacene-Based Thin-Film Transistors With Multiwalled Carbon Nanotube Source And Drain Electrodes. *App. Phys. Lett.* **91**, 1021 (, 2007).

16. A. Southard, V. Sangwan, J. Cheng, E. D. Williams, M. S. Fuhrer, Solution-Processed Single Walled Carbon Nanotube Electrodes For Organic Thin-Film Transistors. *Org. Electron.* **10**, 1556 (2009).

17. Y. Y. Zhang, Y. M. Shi, F. M. Chen, S. G. Mhaisalkar, L. J. Li, B. S. Ong and Y. L. Wu, Poly(3,3 '"-Didodecylquarterthiophene) Field Effect Transistors With Single-Walled Carbon Nanotube Based Source And Drain Electrodes. *App. Phys. Lett.* **91**, 223512 (2007).

18. S. L. Hellstrom, R. Z. Jin, R. M. Stoltenberg, Z. Bao, Driving High-Performance n- and p-type Organic Transistors with Carbon Nanotube/Conjugated Polymer Composite Electrodes Patterned Directly from Solution. *Adv.Mater.* **22**, 4204 (2010).

19. Lefenfeld, M., G. Blanchet, and J.A. Rogers, High-Performance Contacts in Plastic Transistors and Logic Gates That Use Printed Electrodes of DNNSA-PANI Doped with Single-Walled Carbon Nanotubes. *Adv. Mater.***15**, 1188,(2003)

20. D. H. Kim, Y. Jang, Y. D. Park, K. Cho, Controlled One-Dimensional Nanostructures In Poly(3-Hexylthiophene) Thin Film For High-Performance Organic Field-Effect Transistors. *J. of Phy. Chem.* B **110,** 15763 (2006).

21. Y.-K. Lan, C.-I. Huang, Charge Mobility and Transport Behavior in the Ordered and Disordered States of the Regioregular Poly(3-hexylthiophene). *J. Phy. Chem.* B **113**, 14555 (2009).

22. M. Arif, J. Liu, L. Zhai, S. I. Khondaker, Poly(3-Hexylthiophene) Crystalline Nanoribbon Network For Organic Field Effect Transistors. *Appl.Phy. Lett*. **96**, 243304 (2010).

23. J. Liu, J. Zou, L. Zhai, Bottom-up Assembly of Poly(3-hexylthiophene) on Carbon Nanotubes: 2D Building Blocks for Nanoscale Circuits. *Macromol. Rapid Commun*. **30**, 1387 (2009).

24. J. Liu, M. Arif, J. Zou, S. I. Khondaker, L. Zhai, Controlling Poly(3-hexylthiophene) Crystal Dimension: Nanowhiskers and Nanoribbons. Macromolecules **42**, 9390 (2009).

25. D. Joung, A. Chunder, L. Zhai, S. I. Khondaker, High Yield Fabrication Of Chemically Reduced Graphene Oxide Field Effect Transistors By Dielectrophoresis. *Nanotechnology* **21**, 165202 (2010).

26. P. Stokes, S. I. Khondaker, Local-Gated Single-Walled Carbon Nanotube Field Effect Transistors Assembled By Ac Dielectrophoresis. *Nanotechnology* **19**, 175202 (2008).

27. P. Stokes, S. I. Khondaker, High Quality Solution Processed Carbon Nanotube Transistors Assembled By Dielectrophoresis. *App. Phy. Lett.* **96**, 083110 (2010).

28. S. I. Khondaker, Fabrication Of Nanoscale Device Using Individual Colloidal Gold Nanoparticles. *IEE Proc.Circuits, Devices, and Syst*.**151**, 457 (2004).

29. S. I. Khondaker, K. Luo, Z. Yao, The Fabrication Of Single-Electron Transistors Using Dielectrophoretic Trapping Of Individual Gold Nanoparticles. *Nanotechnology* **21**, 095204 (2010).

30. Brewer Science Inc. http://www.brewerscience.com/carbon-nanotube.

31. S. Shekhar, P. Stokes, S. I. Khondaker, Ultrahigh Density Alignment of Carbon Nanotube Arrays by Dielectrophoresis. *ACS Nano* **5**, 1739 (2011).

32. J. Collet, O. Tharaud, A. Chapoton, D. Vuillaume, Low-Voltage, 30 Nm Channel Length, Organic Transistors With A Self-Assembled Monolayer As Gate Insulating Films. *App. Phys. Lett.* **76**, 1941 (2000).

33. J. Z. Wang, Z. H. Zheng, H. Sirringhaus, Suppression Of Short-Channel Effects In Organic Thin-Film Transistors. *App. Phys. Lett.* **89**, 083513 (2006).

34. K. Tsukagoshi, I. Yagi, Y. Aoyagi, Pentacene Nanotransistor With Carbon Nanotube Electrodes. *App. Phys. Lett.* **85**, 1021 (2004).

35. M. Koehler, I. Biaggio, Space-charge and trap-filling effects in organic thin film field-effect transistors. *Phy.Rev.B* **70**, 045314, (2004).

CHAPTER 7: OPTOELCTRONIC TRANSPORT PROPERTIES OF CARBON NANOTUBE/ORGANIC SEMICONDUCTOR THIN FILM DEVICES*

7.1 Introduction

Carbon nanotubes (CNTs) have attracted a lot of attentions for their potential applications in nanoelectronics and optical devices due to their extraordinary electrical, optical and mechanical properties [1]. The CNTs have shown both the electroluminescence and as well as photoconductivity (Figure 7.1). In particular, photoresponse studies of pure CNT films and CNT/polymer composites have attracted tremendous attention because of their easy processability at macroscopic dimensions and promising applications in optoelectronic devices [1-4]. However, these studies also generated considerable debate about the origin of photoconductions in CNT films.

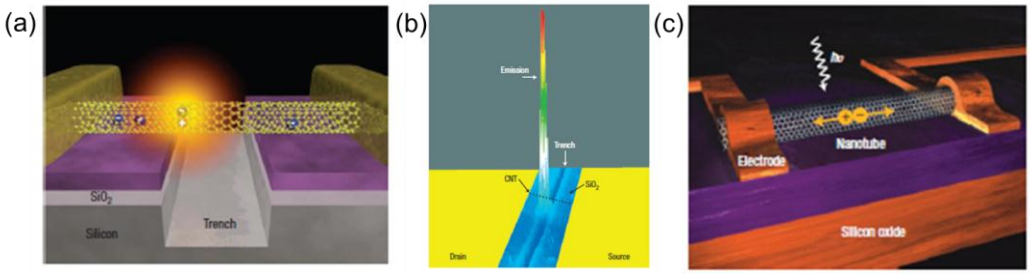

Figure 7.1: Light emission from a nanotube. (a) Schematic of a modified ('trenched'),back-gated nanotube transistor used to produce a sudden change in the potential along the nanotube. (b) Optical image of the trench and of the light emitted at its edge. (c) Photoconductivity with a nanotube. Schematic of a photoconductivity in a carbon nanotube. Adapted from reference [1].

In individual semiconducting single walled carbon nanotube (SWNT) field effect transistor (FET) devices, photoresponse in the near-infrared (NIR) regime was explained using

* Portions of this chapter have been published in the following journals: ***Carbon,*** *48, 1539 (2009);* ***J. Appl. Phys.*** *106, 074307(2009)*

an exciton model (Figure 7.2a) [5, 6]. In another study that involved individual SWNT FET device, the photoresponse under UV illumination was explained by the desorption of molecular oxygen from the SWNT surface which caused a reduction in hole carriers [7]. In contrast, for a large area SWNT film, it was argued that the NIR photoresponse was caused by either the thermal effect [8, 9], or excitonic [10-13]. Itkis *et al.* found that in single walled carbon nanotube (SWNT) film, the photoresponse was due to a bolometric effect, a change in conductivity due to heating of the SWNT network (Figure 7.2b) [8], while Levitsky *et al* showed that in SWNT film, molecular photodesorption to be responsible for change in conductivity upon near infrared (NIR) source illumination [14]. Pradhan et al. [9] in SWNT/polymer composite also found that the photoresponse is bolometric.

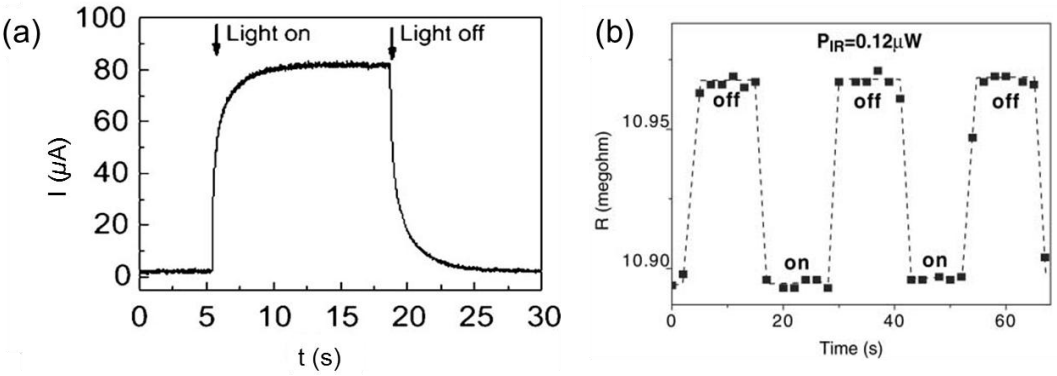

Figure 7.2: (a) The photoelectric response of the device illuminated by the 780 nm laser with 450 mW. (b) Modulation of resistance of SWNT film at 50 K under square-wave pulses of power P 0 0.12 mW IR radiation. Adapted from reference [9, 12].

However, in these measurements, the size of the electrodes was either smaller than the laser spot size or the laser was positioned in the middle and authors did not check the effect of contacts. Further investigations of photoresponse in macroscopic SWNT films [10, 11, 13, 14-16] with large electrode separation have shown that the photocurrent generation depends upon

the position of the laser spot and maximum photoresponse occurs at the metal-SWNT film interface which can be explained by the Schottky barrier modulation model [11].The ongoing debate about the origin of photoconductivity calls for further experimental and theoretical investigations not only in pure CNTs but also in materials where CNTs are used as filler such as CNT/polymer composite.

Incorporation of SWNTs in the polymer matrix has led to a new class of composite materials with multiple functionality and tailored properties [4,17, 18]. For example, optical absorption of SWNTs are dominated by the singularities of their 1D band structure and absorb beyond the visible range into the NIR regime, while poly(3-hexylthiophene)-block-polystyrene polymer (P3HT-b-PS) does not show photo sensitivity beyond 700 nm. Therefore, SWNT/P3HT composite can absorb both in the visible and NIR regimes. In addition, their ease of processability in solution, mechanical flexibility, and low cost of device fabrication at macroscopic dimension make them attractive candidate for large area optoelectronic devices such as fast optical switches, photo detectors and solar cells. Despite their obvious advantages in optoelectronic applications, the optoelectronic transport investigation of large area pure CNT and CNT/polymer composites did not receive much attention.

In this chapter, we discuss photoresponse study of multi-walled carbon nanotube (MWNT) film, SWNT film and SWNT/polymer composite thin films to investigate the photoconduction mechanism. We found that the photocurrent in all of our films is position dependent with maximum photocurrent occurring when illuminated at the metal/CNT film interface and can be explained by excitonic model. While the photocurrent generation can be explained by a Schottky type barrier modulation at the metal/CNT film interface, the slow time response can be described by a model of the diffusion mediated conduction of charge carriers

through many interconnected CNTs. We show that the photoresponse of the CNT/organic semiconductor nanocomposite can be tuned by concentration of SWNTs into the organic semiconductors.

7.2 Experimental Methods

The SWNT, multi-walled carbon nanotube (MWNT) and SWNT/polymer composite films were prepared by drop casting and spin coating method. At first, 3 mg of SWNT was added into 1 ml chloroform in a vial followed by sonication for 1 hour in an ice water bath. Appropriate amount of solution was then drop cast onto a glass slide to make a thin film of SWNT. The slide was kept on a hot plate at around 40-50 ^{0}C for 10-15 minutes to evaporate the residual solvent. The resulting film had a thickness of ~ 60 μm. MWNT films were made by the same method as SWNT films. Figure 7.3 (a) shows the scanning electron microscopy (SEM) images of MWNT thin films.

For SWNT/polymer composites film, the appropriate amount of SWNT/P3HT-b-PS mixture was added to the appropriate amount of PS solution. In order to create a good dispersion of SWNTs in the electrically and thermally insulting polystyrene (PS) matrix, first SWNTs were dispersed into P3HT-b-PS in a 1:1 ratio. This is done by adding 5 mg of SWNTs with 5 mg P3HT-b-PS into 5 ml chloroform in a vial followed by sonication for 1 hour in an ice water bath while the temperature was maintained at 18 -20 ^{0}C. The SWNTs were well dispersed and the solution was very uniform and stable. A 10 wt% PS solution was then made by adding 1.5 gm PS into 10 ml chloroform in a vial and placing it on a rotating stirrer for about 45 minutes. In order to make the composite solution, the appropriate amount of SWNT/P3HT-b-PS mixture was added to the appropriate amount of PS solution. For example, 0.25% composite was made by

mixing 0.25 ml solution of SWNT/P3HT-b-PS with l ml solution of PS in a vial and placed on a shaker for about 7-8 minutes for fine mixing. To prepare the film, the resulting composite solution was spin coated at 300 rpm onto a cleaned glass substrate. Similarly, composite films were made with SWNT weight percentage of 0.5%, 0.75%, 1%, 1.5%, 2%, 5%, 10%, in the polymer matrix. The average thickness of each film was about 60 μm. In addition, a pure P3HT-b-PS film and a pure SWNT film were also prepared for control experiments.Composite films were made on a glass slide with different SWNT weight percentage in the polymer matrix by spin coating. The degree of dispersion and orientation of SWNTs in the polymer matrix were examined by high resolution Scanning Electron Microscopy (HRSEM, Zeiss ULTRA-55 FEG) at an accelerating voltage of 1 KV. Finally, conducting silver paste was used to make a pair of electrodes with channel length 10 mm and channel width 25 mm. In addition, MWNT sample were also prepared with different electrode separations d = 2, 3, 5, 10, 20, 25, 40, 50 mm with a fixed width of 25 mm (Figure 7.3b). The device was then left at room temperature for few hours to dry.

Figure 7.3(c) shows a schematic diagram of a final device and the electrical transport measurement setup. The dc transport measurements were carried out using a standard two-probe technique, both in the dark and under illumination by a laser spot, positioned at three different locations. L corresponds to illumination on the left electrode/film interface, M is between the electrodes in the middle of the sample, and R is the right electrode/film interface. The near IR (NIR) photo source consists of a semiconductor laser diode with peak wavelength of 808 nm (1.54 eV) driven by a Keithley 2400. The laser spot size was approximately 10 mm long and 1 mm wide. The power intensity of the laser was ~ 4 mW/mm^2 .Photocurrent was measured under small V_{bias} (1mV). Data was collected by means of LabView program interfaced with the data

acquisition card and current preamplifier (DL instruments: Model 1211) capable of measuring sub pA signal.The dark current (I_{dark}) and current upon laser illumination (I_{light}) were measured under small bias voltage of 1mV. Photocurrent (I_{photo}) was calculated by subtracting the I_{dark} from the I_{light}.

7.3 Photoresponse of Multi-walled CNT Thin Films

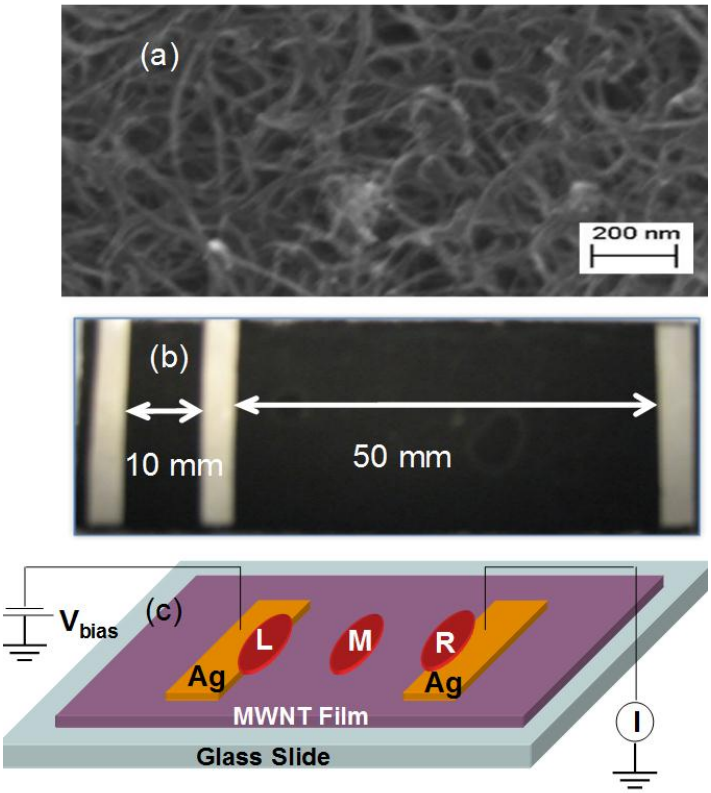

Figure 7.3: (a) Scanning electron micrograph of a MWNTs film (b) An optical micrograph of one of the samples showing two pairs of electrodes. (c) Schematic diagram of the device and electric transport measurement set up. The spacing between the electrode varied from 2 – 50 mm, and wavelength of NIR source is 808 nm. *L*, *M* and *R* mark the position of the laser.

Although there are several studies of photoresponse in SWNT films, there are only a few experimental reports on the photoresponse of multi-walled carbon nanotube (MWNT) films [4,

19]. It should be noted that unlike SWNT, the band structure of MWNT is very complex and difficult to model and the transport properties of MWNTs is usually diffusive [20]. The mechanism for photoresponse in MWNT is not well understood and calls for further experimental and theoretical studies. In particular, experiments of MWNT films with different electrodes separation can be useful in understanding the photoconduction mechanisms in these films. Moreover, MWNT films can be advantageous for practical applications over SWNT films as they can be mass produced, cheaper than SWNT (~$500/g of SWNT vs. < $10/g of MWNT) [21]

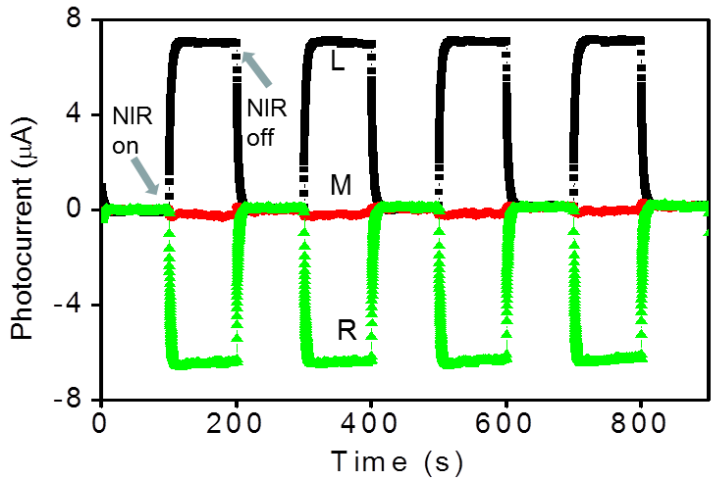

Figure 7.4: Representative photocurrent, as a function of time for a film with 10 mm electrode separation under NIR source illumination at positions *L*, *M*, and *R* (V_{bias} = 1mV). The NIR laser is turned on and off at every 100 s interval.

In this section, we present a near-infrared photoresponse study of MWNT film with different electrodes separation to investigate the photoconduction mechanism in MWNT film. We observed strong dependence of photocurrent on the position of laser spot with maximum photoresponse occurring at the metal MWNT interface. We also show that the time constant of

dynamic photoresponse at metal-film interface depends upon the electrode separation and that the time constant increases from 0.35 to 5.3 seconds as the electrode separation increases from 2 mm to 50 mm. While the photocurrent generation can be explained by a Schottky type barrier modulation at the metal-MWNT film interface, the slow time response can be described by a model of the diffusion mediated conduction of charge carriers through many interconnected MWNTs.

Figure 7.4 shows a typical photoresponse curve for one of our MWNT films with electrode separation d = 10mm, where we plot photocurrent as a function of time (*t*) when the laser spot was positioned at *L*, *M*, and *R* and was turned on and off every 100 s interval. It can be seen that the photocurrent strongly depends on the position of the laser spot. When illuminated at position *L* there is an increase in photocurrent. When shined at position *M*, there was almost no photocurrent generation, whereas position *R* shows a decrease in photocurrent when illuminated by the NIR source. It can be seen that the on and off current is completely reproducible over several cycles. Similar position dependent behaviour of the photocurrent has been observed in all our samples with electrode separations ranging from 2 mm to 50 mm. The large enhancement of photocurrent at the metal – carbon nanotubes interface can be described by Schottky barrier model [11]. When the laser is shined at the left metal-nanotube interface, photons are absorbed by carbon nanotubes which in turn create excitons (bound electron-hole pair). Some of these electrons have enough energy to overcome the barrier potential by tunnelling or thermal emission and fall into metal electrode leaving holes in the nanotube film. This induces a separation of electrons and holes at the interfaces and creates a local electric field. Therefore, a positive photocurrent generates at this interface. On the other hand, when the laser shines at right interface, the separation of electrons and holes also generates a local electric field, however, in

the opposite direction than that of left interface. Therefore the photocurrent is negative with almost same magnitude as of left electrode. However, when the laser light shines at the middle part of the sample *M*, electron-hole pairs are also generated but because of the absence of interface they do not get separated and no local electric field is created at this point. So, compare to the photocurrent at left or right metal-nanotube interface, a much smaller photocurrent is seen at the middle position.The reason for a very small positive photocurrent at *M* can be explained as follows: the spot size of our near infrared (NIR) source is approximately 10 mm long and 1 mm wide and the positioning was done manually. Because of the finite width (10 mm long and 1 mm wide) of the NIR source and manual positioning, there is always a small error in positioning. Therefore although the laser was positioned in the middle, there might be small imbalance in positioning towards the left electrode which in turn can create charge carrier imbalance giving a very small photocurrent.

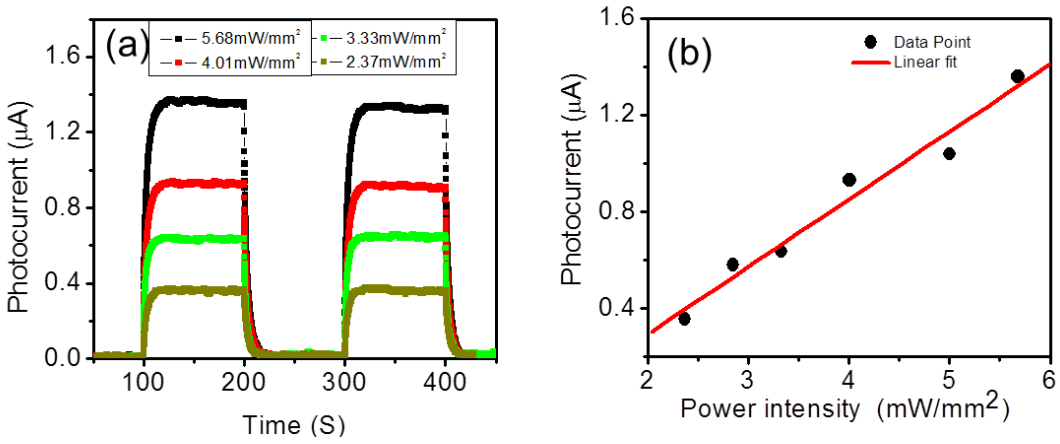

Figure 7.5: (a) Photocurrent versus time for a few different laser intensities. (b) Dependence of photocurrent of the MWNT film on the laser intensity.

Figure 7.5a shows a representative plot of photocurrent vs. time when illuminated at position L for another sample with electrode separation 25 mm for a few laser intensities (2.37,

3.33, 4.01, and 5.68 mW/mm^2 from bottom to top). The intensity of laser light was changed by changing the height between the sample and laser source. The plot is shown for two cycles of the laser being turned on and off at every 100 s intervals. In Figure 7.5b we plot the photocurrent versus laser power intensity for the same sample shown in Figure 7.5a for all the laser intensities. The solid line is a linear fit of the data which shows that the photocurrent increases linearly with intensity. Similar observation was reported for SWNT films [13]. When the intensity of the laser light is higher, more photons are absorbed by the carbon nanotubes and generate more excitons. So a greater number of electrons have the probability to overcome the Schottky barrier, generating a larger photovoltage. On the other hand, when intensity of laser light is low, a smaller photovoltage is generated.

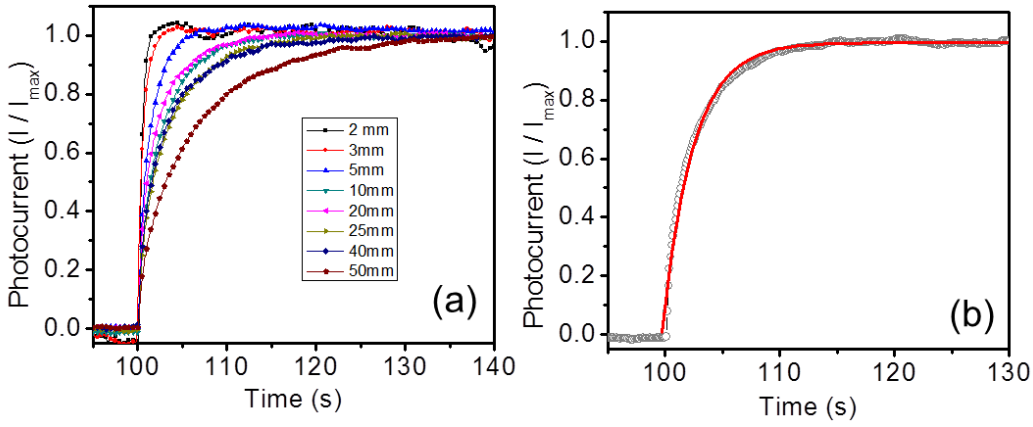

Figure 7.6: Time response of the photocurrent. (a) Raising part of normalized photocurrent as a function of time for all film with electrode separations of 2-50 mm. The laser light was positioned at left MWNTs/electrode interface. (b) Sample with electrode separation 10 mm. The open circles are data and the solid line is the exponential fit with a time constant $\tau = 2.65$ s.

We now investigate the time response of the photocurrent. Figure 7.6a shows a plot of the rising part (first 40 s) of the normalized photo-current (I/I_{max}) versus time for all of our MWNT films with electrode separations of 2, 3, 5, 10, 20, 25, 40 and 50mm when illuminated at left

electrode. The top curve is for d = 2 mm and the bottom is for d = 50 mm. Two features can be noticed from this data: (i) the response time, also known as time constant, time takes to reach maximum photocurrent is rather slow and (ii) the response time increases with increasing separation. The dynamic response to the NIR source can be well described by $I = I_0[1-\exp(-(t-t_0)/\tau)]$, where τ is time constant, t_0 is the time when NIR is switched on, and I_0 is the steady state photo current. Figure 7.6b shows a fit of this equation for one of the sample with electrode separation of 10 mm. Open circles are the experimental points and the solid line is a fit to the above equation. From this fit we obtain τ =2.65 s. Similar fits were done for all the samples and the measured time constants were 0.35, 0.62, 1.50, 2.65, 3.39, 4.13 and 5.27 seconds for 2, 3, 5, 10, 20, 25, 40 and 50 mm electrode separations respectively. From here, we conclude that the time constant increases with increasing electrode separations. Similar increases in time constants were also obtained for the decaying part when the laser was switched off and for the right electrode-CNT film interface.

There is a lot of debate about the origin of slow time response of photocurrent in CNT films. Previous studies in SWNT films have shown that bolometric effect [8], molecular photodesorption [7] and charge carrier diffusion [10] can explain the photoresponse and slow time response in photocurrent. In bolometric mechanism, the temperature of carbon nanotube raises upon NIR source illumination which causes a decrease in resistance of nanotube film and hence generates only a positive photoresponse. However, in our experiment, we find both positive and negative photoresponse at two different interfaces *L* and *R* respectively. On the other hand, in photodesorption effect, there is an increasing drift current over time. But our data is highly reproducible and we did not find any drift current over time for several cycles (Figure 7.4). So, we rule out both bolometric and photodesorption in our film.

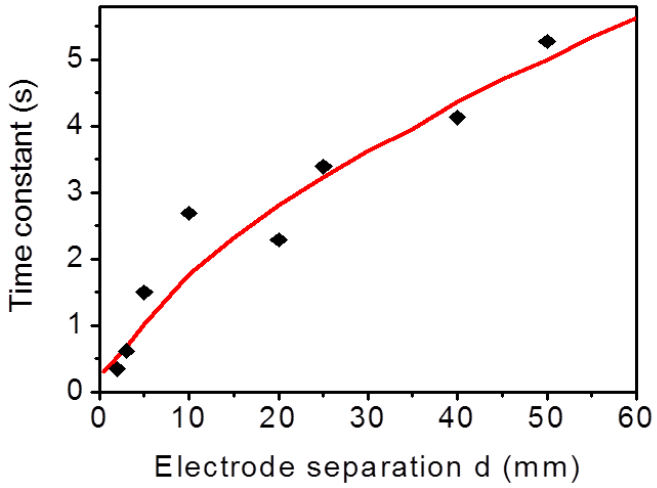

Figure 7.7: Variation of time constant with electrode separation. The black squares are the measured time constant and the solid line is a fit to the diffusion model.

We now examine whether carrier diffusion model can explain our data. According to the diffusion model, considering a parabolic impurity density distribution, the time constant can be described as [10, 22]

$$\tau = \frac{d^2}{2D_p(r+1)}\left[1 - \frac{I_{(1/2)(r+3)}(d/L_p)}{I_{(1/2)(r-1)}(d/L_p)}\right] \tag{7.1}$$

where d is the electrode separation, L_p is diffusion length, D_p is diffusion coefficient of hole, I_n is modified Bessel of the first kind of order n and $r \sim d^{\alpha}$ is a real constant for a parabolic impurity density distribution function. According to this model, the time constant should increase with increasing electrode separations. In order to see whether the diffusion model can describe the slow time response in our MWNT networks, we plotted the time constant as a function of electrodes separation in Figure 7.7 and fitted the data with the above equation. The black squares are the measured time constants while the solid curve is a fit to the diffusion equation for charge carrier using L_p=1 mm, D_p=0.01cm^2/Vs and α=1.4 as fitting parameters. These parameters are

similar to what was obtained for SWNT networks. It can be seen from Figure 7.7 that the experimental data can be fitted reasonably well with the diffusion model. Therefore, we conclude that the slow time response in our film is due to the diffusion of free charge carriers that was created at the metal-MWNT film interface. In other words, the slow response is due to the diffusion mediated charge transport through many interconnected individual MWNTs.

7.4 Photoresponse of Single-Walled CNT Films

In this section, we investigate the excitonic and thermal effect on the photoresponse of SWNT films using photocurrent-time and current-voltage characteristics under NIR laser illumination at different positions of the sample. We show that the photocurrent is position dependent with maximum photoresponse [(light current-dark current)/dark current] of ~40% occurring at the SWNT/electrode interface. By examining the *I-V* characteristics in the dark and under NIR laser illumination, we found that (i) a photovoltage is generated while laser is illuminated at the interface, and (ii) the resistance change due to laser illumination is only 0.4%. By comparing the two sets of measurements, we show that the thermal contribution in the photoresponse is only 0.4% while excitonic contribution is more than 39%. Our study clearly suggests that the dominant photoresponse mechanism in SWNT film is due to exciton generation and dissociation into electron and holes at the SWNT/electrode interface.

Photocurrents of the nanotube film as a function of time (t) in the dark and under laser source illuminated at *L*, *M*, and *R* of the device are shown in Figure 7.8 (a)-(c). The laser was turned on at t = 50 s and was switched on and off every 50 s intervals. The two cycles of photocurrent demonstrate the reproducibility and stability of on and off current. When laser source is illuminated at position *L, M and R*, we observed an increased in photocurrent at

position *L* (Figure 7.8a), decrease of photocurrent at position *R* (Figure 7.8b) and almost no change of photocurrent at *M* (Figure 7.8c). These Figures clearly show that photocurrent is positional dependent and a large enhancement of photocurrent at the electrode/nanotube interfaces. At position *L*, the I_{dark} and I_{light} of the device are ~9.95 µA and ~13.93 µA respectively and the calculated photoresponse is 40.2%. Similarly, the photoresponse under laser illumination at *R* is 40.5%. However, we observed a negligible photoresponse at position *M* due to almost zero photocurrent generation in the middle of the device.

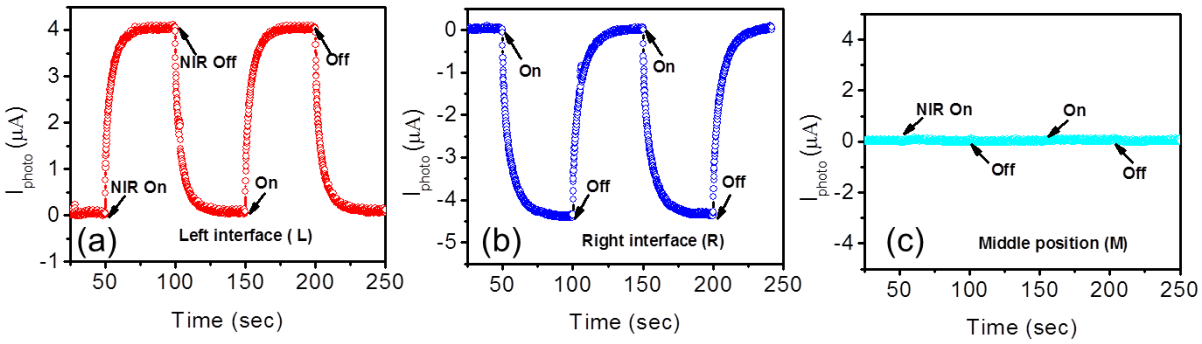

Figure 7.8: Photocurrent as a function of time under NIR laser illumination at positions *L*, *M* and *R*. Under laser illumination photocurrent is (a) increased, (b) decreased and (c) no change. The laser is turned on and off at every 50 s interval.

In order to examine the photoresponse mechanism of nanotubes, we measured *I-V* characteristics of the device both in the dark and under laser source illumination at positions *L*, *M* and *R*. This is shown in Figure 7.9. We note that all the *I-V* curves are linear, and while the *I-V* curves in the dark and *M* pass through the origin, there is an offset for *L* and *R*. This offset will be discussed in a later section. To investigate possible thermal contribution in the photoresponse, we first calculated the resistance of the devices from these *I-V* curves which is 238.8 KΩ in dark, while it is 237.9, 238.3 and 238.1 KΩ under laser illumination at *M*, *L* and *R* respectively. The

main characteristic of the photoresponse in the thermal model is resistance change (*ΔR/R)* of the film due to increase of temperature under laser illumination [23, 24]. The *ΔR/R* of our device is very small, and the maximum calculated *ΔR/R* is only ~0.4%. This indicates that the maximum thermal contribution upon laser illumination is no more than 0.4% while the total photoresponse is ~40%.

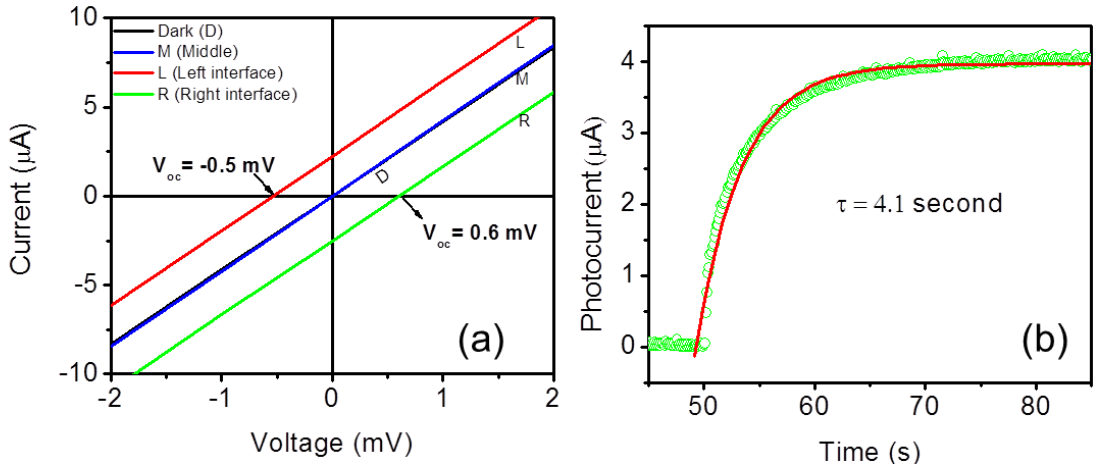

Figure 7.9: (a) *I-V* characteristics of the device in dark and under laser illumination at positions *L*, *M* and *R* .The I-V curves in dark and for position M pass though the origin. *I-V* curves for position *L* and *R* are shifted above or below the origin respectively and generating an offset voltage -0.53 and +0.62 mV respectively. (b) Time response of photocurrent of the SWNT film. The open circles are data and the solid line are the exponential fit with a time constant τ = 4.1 s for rising for the laser illumination at left electrode/nanotube interface

We now examine the excitonic contribution to the photoresponse. As we see in Figure 7.9a that *I-V* curves under laser source illumination at position *M* pass though the origin which indicates that photovoltage generation under laser illuminated at *M* was zero. This is consistent with Figure 7.8c where no photocurrent was observed at position *M*. On the other hand, the *I-V* curves for position *L* and *R* are shifted above or below the origin respectively and generating a negative photovoltage of -0.5 mV and a positive photovoltage of +0.6 mV respectively. In

addition, we also observed offset current of +2.2 µA and -2.5 µA at position *L* and *R* respectively. The opposite signs of the offset current and photovoltage are consistent with the result shown in Figure 7.8a and 7.8b. A large position dependent photoresponse as well as opposite sign of the photovoltage maxima at the interfaces indicate the existence of a locally generated electric field at the electrode/nanotube interface [25, 26].

Table 7.1: Comparison of thermal and exciton photoresponse of SWNT thin film

Laser illumination position	Total Photoresponse (%)	R (KΩ)	$\Delta R = R_{light} - R_{dark}$ (KΩ)	ΔR/R (%)	Thermal Photoresponse (%)	Excitonic Photoresponse (%)
Left interface	40.2	238.3	0.5	0.21	0.21	39.99
Right interface	40.5	238.1	0.7	0.29	0.29	40.21
Middle (only nanotubes)	0.84	237.9	0.37	0.37	0.37	0.47
Dark (laser off)	-	238.8	-	-	-	-

Now we discuss the contribution of the thermal effect and excitonic effect in the photoresponse of our device. From the current-voltage characteristics and photocurrent profiles (Figure 7.8 and 7.9a), we have already showed that the maximum thermal photoresponse of our device is only 0.4%, whereas total photoresponse are 40.2% and 40.5% at left and right interfaces respectively. If we consider the total photoresponse of our device is a combination of thermal and excitonic mechanisms, then the excitonic photoresponse at both left and right interfaces are more than 39% (Table 7.1). This clearly shows that the dominant contribution in the photoresponse of our nanotube film is excitonic. It has been reported that by illuminating with NIR source of intensity 30 mW/mm^2 on the nanotube bundle for 1h, the increases in temperature is about 0.5 K [27]. In our experiment, the intensity of the NIR laser was lower (4 mW/mm^2) and it was illuminated on the device only for 4-5 minutes. This also suggests that

increased of nanotubes temperature and hence the thermal photoresponse due to laser illumination in our device are very small.

Another important parameter to distinguish between the thermal and excitonic mechanisms of the photoresponse is the time constant. Figure 7.9b shows a plot of photocurrent as a function of time for nanotube film when the laser is turned on at t =50 s and turn off at position L. When the laser source turns on (off), current slowly increases (decreases) until it reaches its steady state. The dynamic response of our device to the laser source can be described well by simple kinetic model $I(t) = I_{dark} + D\{1- \exp(-(t-t_0)/\tau)\}$ and $I(t) = I_{dark} + D \exp(-(t-t_0)/\tau)$ for growth and decay respectively, where τ is the time constant, and t_0 is the time when laser was switched on or off and D is the scaling constant [25, 26, 28]. In the Figure, open circles are the experimental data points and the solid lines are the fits to the above equations. From these fits, we calculated time constants, and found to be 4.1 and 5.4 seconds for growth and decay of the photocurrent respectively. In order to determine whether this slow time response indeed comes from the laser illumination on the device or not a delay due to an *R-C* like circuit existing in the entire setup, we also measured the time response of this film with a step function voltage (not shown here). We found that unlike laser source, the current increases almost instantaneously to a bias voltage switch. Therefore, the slow time response indeed comes from the laser illumination and not a delay due to an *R-C* like circuit existing in the entire setup.

The time constant measured in our study is much larger than what has been measured for thermal response (typically in the order of millisecond) [8], and is similar to other studies of excitonic photoresponse in nanotube films [10, 11, 25, 26]. All the results presented here show that the dominant photoresponse mechanism is consistent with the excitonic model [10, 14, 25, 26, 29]. When NIR laser is illuminated on the nanotube film, excitons are generated and

dissociated into free charge carriers at electrode/nanotube interface. Some energetic electrons overcome the barrier at the interface and enter into the metal electrode leaving the hole in the film. Once the barrier is crossed, the electrons cannot return into the film due to the Schottky barrier asymmetric profiles. This causes a hole-electron separation and generates a positive photovoltage at right contact. Similarly, a negative photovoltage is generated at the left contact because the right contact is a mirror image of the left contact. Therefore, opposite sign of photocurrent has been observed due to sign inversion of the photovoltage maxima between the contacts. The generated charges then diffuse through the percolating inter-nanotube junctions causing a large response time [25].

7.5 Photoresponse of CNT/Organic Semiconductor Composite Films

In this section, we present a photoresponse study of SWNT/P3HT-b-PS polymer composite films with different SWNTs loading ratios in the polymer matrix under NIR illumination. Figure 7.10 (a) and (b) show the scanning electron microscopy (SEM) images of pure SWNT film and 1% wt SWNT / P3HT-b-PS composite film respectively. The schematic diagram of the device and electric transport measurement set up is shown in Figure 7.10c. Figure 7.10d shows a typical photoresponse curve for one of the composite films with 1% SWNTs, where the photocurrent (I_{photo}) was plotted as a function of time (t) when the laser spot was positioned at L, M and R. The laser was turned on at t = 50 s and was switched off and on at 50 s intervals. Two cycles are shown to demonstrate the reproducibility of the on-off current. Similar to MWNT and SWNT films photoresponse, when illuminated at position L there is an increase in photocurrent, while at position M there is a very small photocurrent generation, whereas position

R shows a decrease in photocurrent. The dark current for this sample was 0.245 nA and the current under illumination at position *L* was 0.499 nA, giving an enhancement of 104%.

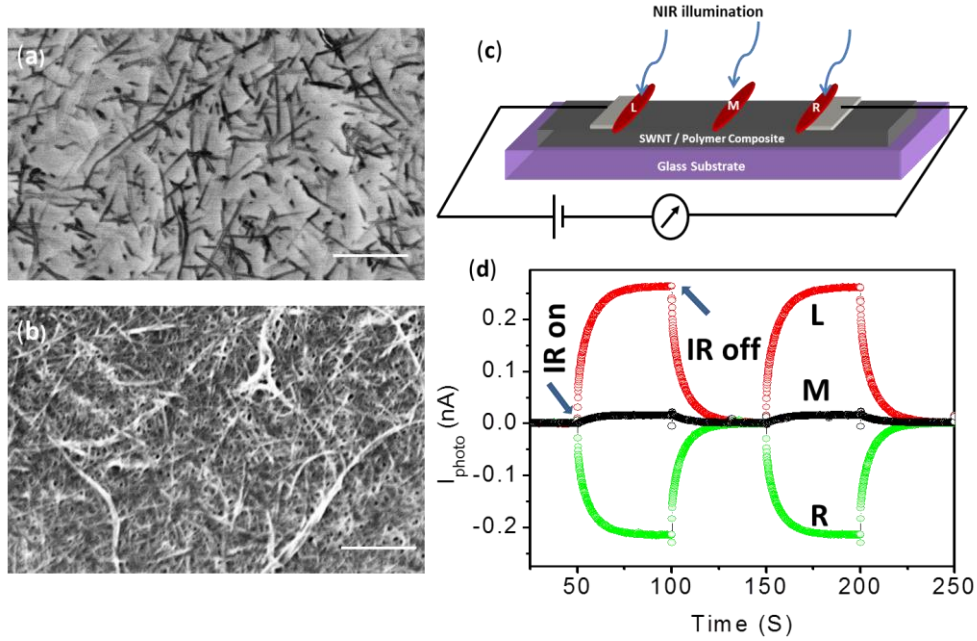

Figure 7.10: SEM image of the (a) 1% wt SWNT / P3HT-b-PS composite film (b) 100% SWNT film (scale bar : 1 µm). (c) Schematic diagram of the device and electric transport measurement set up. NIR laser wavelength was 808 nm and laser intensity was 4 mW/mm^2. *L*, *M* and *R* mark the positions of the laser with respect to the electrode. (d) Photocurrent as a function of time for 1% SWNT/P3HT-b-PS composite film under NIR illumination at positions *L*, *M* and *R*. The IR laser is turned on t = 50 s and turned off and on at every 50 s interval. V_{bias} = 1 mV.

Figure 7.10d shows a typical photoresponse curve for one of the composite films with 1% SWNTs, where the photocurrent (I_{photo}) was plotted as a function of time (t) when the laser spot was positioned at *L*, *M* and *R*. The laser was turned on at t = 50 s and was switched off and on at 50 s intervals. Two cycles are shown to demonstrate the reproducibility of the on-off current. Similar to MWNT and SWNT films photoresponse, when illuminated at position L there is an increase in photocurrent, while at position *M* there is a very small photocurrent generation, whereas position *R* shows a decrease in photocurrent. The dark current for this sample was 0.245

nA and the current under illumination at position *L* was 0.499 nA, giving an enhancement of 104%.

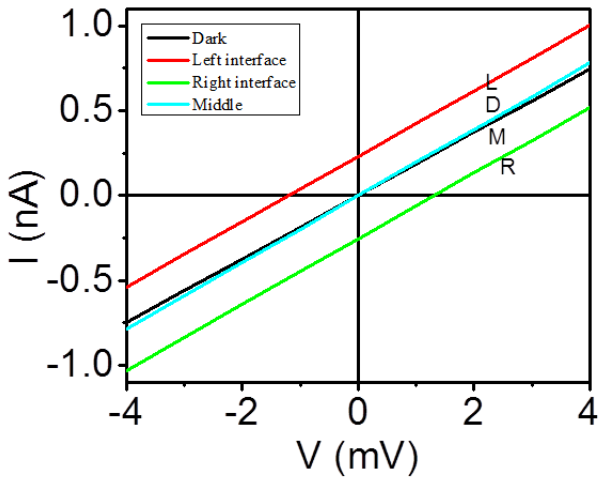

Figure 7.11: *I-V* characteristics of a 1% SWNT composite film in the dark and illuminated at *L*, *M* and *R* on the sample.

In order to inspect the position dependent photocurrent further, we measured current–voltage (*I –V*) characteristics of the composite films in dark and under laser light illumination at positions *L*, *M* and *R*. Figure 7.11 shows a representative *I-V* curve for the 1% composite film. It can be seen that the *I-V* curves in the dark and at position *M* go directly though the origin, whereas when illuminated at position *L* and *R*, the *I-V* curve is slightly shifted above or below the origin, respectively. At zero applied bias, there is about +0.23 nA current at *L* and -0.26 nA at R. All the *I-V* curves show Ohmic behaviour from which we can calculate the resistances of the sample under different illumination condition. The resistances of the sample in the dark are 5.35 GΩ, while it is 5.11, 5.20 and 5.15 GΩ for NIR illumination at *M*, *L* and *R* respectively. So, the resistance slightly decreases under illumination with a maximum decrease of ~4.5%.

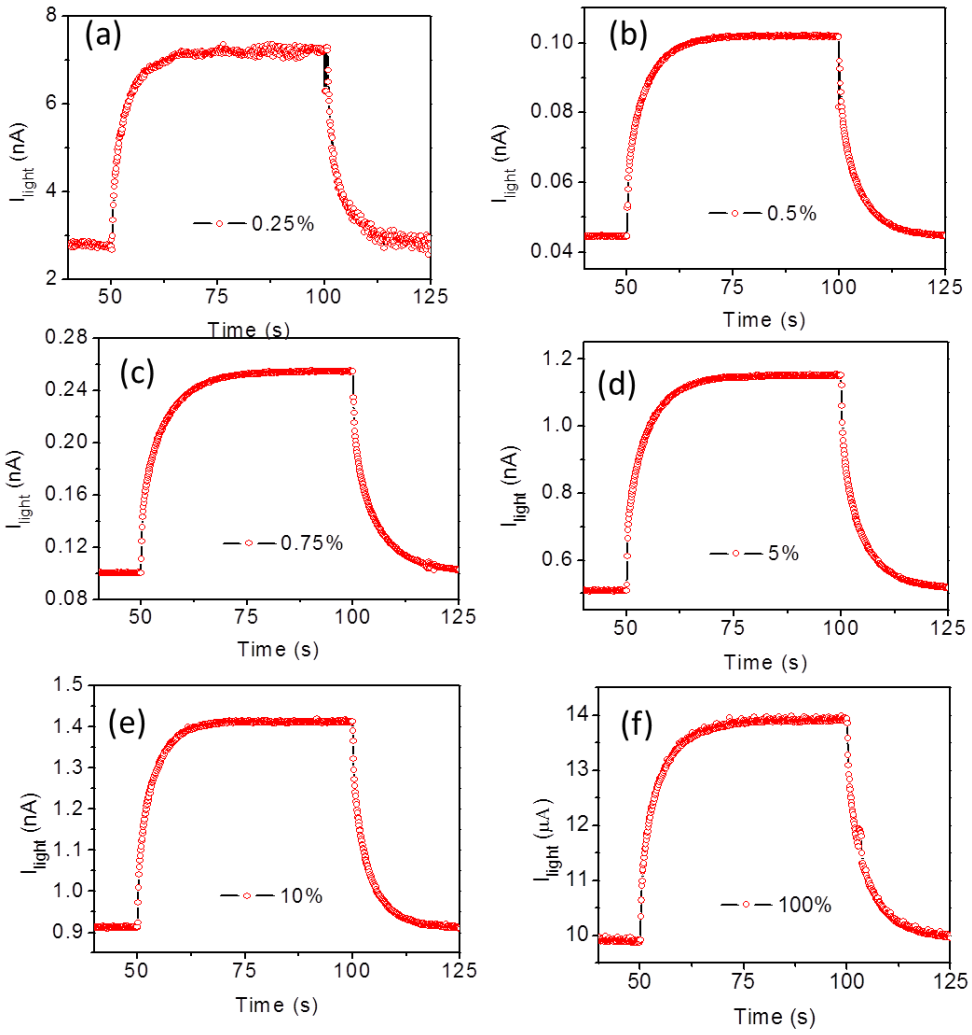

Figure 7.12: Photocurrent of (a) 0.25%, (b) 0.5%, (c) 0.75%, (d) 5%, (e) 10% SWNT composite films and (f) pure SWNT film. The NIR was turned on at t = 50 s and turned off at t = 100 s.

A small change (less than 2%) in conductivity upon NIR illumination in SWNT film was found in previous studies and was explained by a thermal effect. [7, 8] If thermal effect was responsible for photocurrent generation in our sample, it would have only generated a 4.5% change in photocurrent. Therefore, a photocurrent enhancement of 104% in our sample at the electrode-metal interface cannot be described using thermal effect. In addition, the resistance decreases under illumination at all positions which can cause an increase in photocurrent only.

Whereas, in position R we observed a decrease in photocurrent providing further evidence that thermal effect is not responsible for photoresponse in our sample. Furthermore, a finite current at zero bias at position *L* and *R* suggests that a photovoltage is generated upon NIR illumination at the SWNT-metal interface.

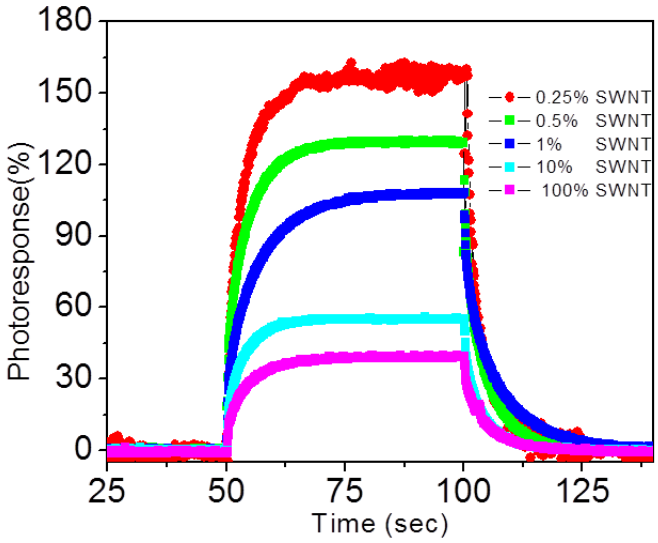

Figure 7.13: Variation of the photoresponse in the SWNT/polymer composite film with different loading ratios of the SWNT.

Similar behaviour of the photocurrent has been observed in all our samples with different SWNT loading ratios excluding the pure P3HT-b-PS film. For this sample, under 1 mV bias, signal to noise (S/N) ratio was extremely low, therefore the photocurrent was not very reproducible. The S/N ratios for all other composite films were more than 50 making the photocurrent easier to detection. Figure 7.12 shows I_{light} for 0.25 %, 0.5%, 0.75%, 5%, 10% weight percentage of SWNT in the polymer matrix and pure SWNT film when illuminated at position *L*. The laser was switched on at t = 50 s and off at t = 100 s. Table 7.2 summarizes the experimental data from all of the samples, where dark current, light current, photoresponse, and

external quantum efficiency (EQE) are shown for the different loading ratios of SWNT composite films at position L. The EQE at λ = 808 nm at a fixed power of 4 mW/mm^2 was calculated using $EQE = (R_\lambda / \lambda) \cdot 1240 \quad W \cdot nm/A$, where R_λ is the responsivity defined by the photocurrent per watt of input power.

Table 7.2: Dark current, light current, photoresponse and external quantum efficiency (EQE) for SWNT/P3HT-b-PS composite films under the NIR illumination at position *L*.

wt % of SWNT	I_{dark} (A)	I_{light} (A)	$\Delta I / I_{dark}$ (%)	EQE (%)
0.25	2.80×10^{-12}	7.19×10^{-12}	156.78	1.7×10^{-7}
0.5	4.44×10^{-11}	1.01×10^{-10}	127.47	2.2×10^{-6}
0.75	1.00×10^{-10}	2.52×10^{-10}	152.00	5.8×10^{-6}
1	2.45×10^{-10}	4.99×10^{-10}	103.67	9.7×10^{-6}
1.5	3.38×10^{-10}	6.05×10^{-10}	78.99	1.0×10^{-5}
2	8.60×10^{-10}	1.82×10^{-9}	111.63	3.7×10^{-5}
5	5.09×10^{-10}	1.14×10^{-10}	123.97	2.4×10^{-5}
10	9.11×10^{-10}	1.41×10^{-10}	54.77	1.9×10^{-5}
100	9.95×10^{-6}	13.93×10^{-6}	40.00	0.14

As can be seen from Table 7.2 and Figure 7.13, the amount of SWNTs in the polymer matrix has a strong influence on the photoresponse. The photoresponse is 157% for 0.25% SWNT/P3HT-b-PS composite film while it is only 40% for pure SWNT film. The stronger photoresponse in SWNT/P3HT-b-PS films could be caused by the fact that the off current of the composite films can be reduced by several orders of magnitude by reducing the SWNT content in the polymer matrix, which allows easy detection of the photocurrent when SWNTs are in an electrically and thermally insulating polymer host.

We note that in SWNT-polycarbonate composite films studied by Pradhan et al. [9] a photoresponse enhancement in composite film was also observed. However, the maximum

photoresponse in their study was only 5%. In our case, the maximum photoresponse is much higher (157%) which is 31 times larger than that of ref [9]. One possibility for the low enhancement in the study of Pradhan et al. [9], could be due to the fact that in their study, the illumination of NIR was around the middle part of the sample and that the authors did not check the effect of contact.

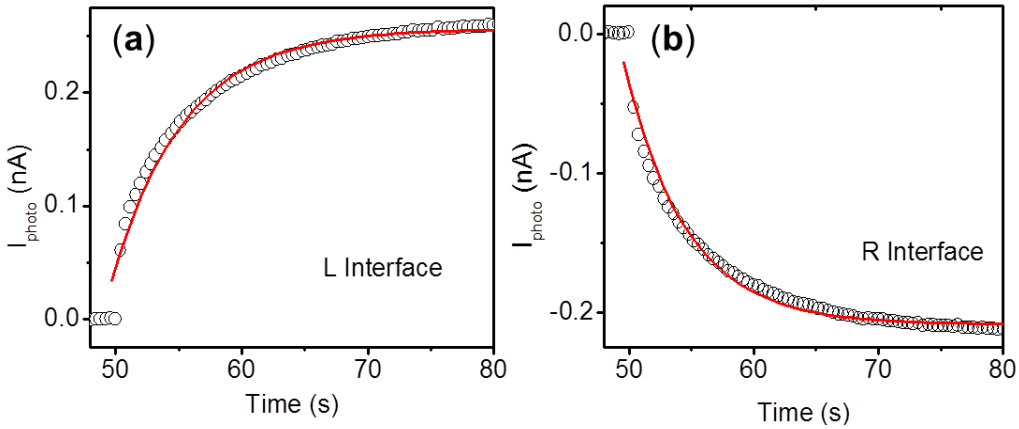

Figure 7.14: Time response of the photocurrent for 1% SWNT/P3HT-b-PS composite film with NIR illuminated at position *L* (a) and *R* (b). The open circles are the experimental points and the solid line is an exponential fit of the data.

We now examine the slow time response of photocurrent when NIR source is switched on. Figure 7.14 is a plot of photocurrent as a function of time for the 1% composite film when the NIR is turned on at t =50 s, at position L (Figure 7.14a) and at position R (Figure 7.14b). When illuminated by the NIR source the current slowly increased (decreased for R) until it reached its steady state.The dynamic response to the NIR source can be well described by $I = I_0\left[1-\exp\left(-(t-t_0)/\tau\right)\right]$, where τ is time constant, t_0 is the time when NIR is switched on, and I_0 is the steady state photo current. In both Figures, the open circles are the experimental data points and the solid lines are a fit to the above equation. From the fit in Figure 7.14 the time constant was calculated to be 5.7 and 4.9 seconds for position L and R respectively. Similar fits

were also done for all the samples and time constants were calculated. The time constant measured for all our sample ranged from 3.18 to 5.7 second.

What causes photoresponse in our SWCNT/P3HT-b-PS composite samples? In previous studies, the photoresponse in SWCNT film has been explained by either thermal or excitonic mechanisms. In thermal mechanism, the temperature of the carbon nanotube film raises upon NIR illumination causing a decrease in the resistance of the nanotube film, hence a positive photoresponse [8]. We rule out thermal mechanism because both the positive and negative photoresponse at two different positions cannot be explained by this model. In addition, the *I-V* curves at different positions show that even if thermal effect were present, it may account for a 5% change in current only, not the 157% seen in our sample. Our results presented here are consistent with the model of exciton generation upon NIR absorption and exciton dissociation at the metallic electrode -SWCNT interface due to a Schottky barrier [11]. In other words, when the laser light is illuminated at the interface, some energetic electrons overcome the asymmetric tunnel barrier at the interface and fall into the metal electrode leaving holes in the film. This causes an electron-hole separation at the interface and thereby creates a local electric field. Under the influence of this electric field, the carrier then diffuses to the other electrode through percolating SWCNT networks. Similar phenomenon occurs at the other electrode except that the right contact is a mirror image of the left contact and, therefore, the sign of photoresponse reverses. Whereas, when the laser is shined in the middle part of the sample electron hole pairs are created, however, the charge does not get separated so the overall photovoltage is almost zero. However, in our experiment, a very small photocurrent (5.7%) is seen at position M. The reason for a very small positive photocurrent at M can be explained as follows: the spot size of

our near infrared (NIR) source is approximately 10 mm long and 1 mm wide and the positioning was done manually. Because of the finite width (10 mm long and 1 mm wide) of the NIR source and manual positioning, there is always a small error in positioning. Therefore although the laser was positioned in the middle, there might be small imbalance in positioning towards the left electrode which in turn can create charge carrier imbalance giving a very small photocurrent. Another reason could be that, even if the laser was positioned accurately at M, the thermal effect could also account for about 4.7% photocurrent. The interface between the SWCNTs and polymer may also help dissociate the exciton [30-32] and could be responsible for the ~ 5% change in conductivity in the middle part of the sample.

7.6 Conclusion

In conclusion, we presented photoconduction mechanism of the CNT and CNT/organic semiconductor nanocomposite thin film devices. We found that the photoconduction is due to the exciton dissociations and charge carrier separation caused by a Schottky barrier at the metallic electrode/CNT interface. The time constant for dynamic photoresponse increases with increasing electrode separations and can be explained by the diffusion of charge carriers through percolating CNT interconnects. We found that the photoconduction mechanism in our devices was not caused by a thermal effect but by exciton dissociations at the metal/CNT interface. The photoresponse of the CNT/polymer composite film can be tuned by changing the weight percentage of CNT into the organic semiconductor composite. This study not only provides further evidence about the origin of photoresponse in SWNTs in favor of excitonic model but also offers opportunity to fabricate new classes of optoelectronic devices such as low cost infrared photo detectors and position sensitive detectors using CNT as well as CNT/organic semiconductor composites.

7.7 References

1. P. Avouris, Z. Chen, V. Perebeinos, Carbon-based electronics. *Nature Nanotech*. **2**, 605 (2007).

2. R. H. Baughman, A. A. Zakhidov, W. A. de Heer, Carbon Nanotubes - The Route Toward Applications. *Science* **297**, 787 (2002).

3. R. A. Hatton, A. J. Miller, S. R. P. Silva, Carbon Nanotubes: A Multi-Functional Material For Organic Optoelectronics. *J. Mater. Chem.* **18**, 1183 (2008).

4. P. M. Ajayan, J. M. Tour, Materials Science - Nanotube Composites. *Nature* **447**, 1066 (2007).

5. M. Freitag, Y. Martin, J. A. Misewich, R. Martel, P. H. Avouris, Photoconductivity Of Single Carbon Nanotubes. *Nano Lett.* **3**, 1067 (2003).

6. X. H. Qiu, M. Freitag, V. Perebeinos, P. Avouris, Photoconductivity Spectra Of Single-Carbon Nanotubes: Implications On The Nature Of Their Excited States. *Nano Lett.* **5**, 749 (2005).

7. R. J. Chen, N. R. Franklin, J. Kong, J. Cao, T. W. Tombler, Y. G. Zhang and H. J. Dai, Molecular Photodesorption From Single-Walled Carbon Nanotubes. *Appl. Phy. Lett.* **79**, 2258 (2001).

8. M. E. Itkis, F. Borondics, A. P. Yu, R. C. Haddon, Bolometric Infrared Photoresponse Of Suspended Single-Walled Carbon Nanotube Films. *Science* **312**, 413 (2006).

9. B. Pradhan, K. Setyowati, H. Liu, D. H. Waldeck, J. Chen, Carbon Nanotube - Polymer Nanocomposite Infrared Sensor. *Nano Lett.* **8**, 1142 (2008).

10. C. A. Merchant, N. Markovic, Effects Of Diffusion On Photocurrent Generation In Single-Walled Carbon Nanotube Films. *App. Phy. Lett.* **92**, (2008).

11. S. X. Lu, B. Panchapakesan, Photoconductivity In Single Wall Carbon Nanotube Sheets. *Nanotechnology* **17**, 1843 (2006)

12. J. L. Sun, J. Wei, J. L. Zhu, D. Xu, X. Liu, H. Sun, D. H. Wu and N. L. Wu,Photoinduced Currents In Carbon Nanotube/Metal Heterojunctions. *Appl. Phy. Lett.* **88**, 131107 (2006).

13. D. H. Lien, W. K. Hsu, H. W. Zan, N. H. Tai, C. H. Tsai. Photocurrent Amplification At Carbon Nanotube-Metal Contacts, *Adv. Mater.* **18**, 98, (2006).

14. I. A. Levitsky, W. B. Euler, Photoconductivity Of Single-Wall Carbon Nanotubes Under Continuous-Wave Near-Infrared Illumination. *Appl. Phy. Lett.* **83**, 1857 (2003).

15. Y. Liu, S. Lu, B. Panchapakesan, Alignment Enhanced Photoconductivity In Single Wall Carbon Nanotube Films. *Nanotechnology* **20**, 035203 (2009).

16. C. A. Merchant, N. Markovic, The Photoresponse Of Spray-Coated And Free-Standing Carbon Nanotube Films With Schottky Contacts. *Nanotechnology* **20**, 175202 (2009).

17. J. Zou, L. Liu, H. Chen, S. I. Khondaker, R. D. McCullough, Q. Huo and L. Zhai, Dispersion Of Pristine Carbon Nanotubes Using Conjugated Block Copolymers. *Adv. Mater.* **20**, 2055 (2008).

18. J. Zou, S. I. Khondaker, Q. Huo, L. Zhai, A General Strategy To Disperse And Functionalize Carbon Nanotubes Using Conjugated Block Copolymers. *Adv. Funct.Mater.* **19**, 479 (2009).

19. P. Castrucci, F. Tombolini, M. Scarselli, E. Speiser, S. Del Gobbo, W. Richter, M. De Crescenzi, M. Diociaiuti, E. Gatto and M. Venanzi, Large Photocurrent Generation In Multiwall Carbon Nanotubes. *App. Phy. Lett.* **89**, 253107 (2006).

20. M. Ahlskog, O. Herranen, A. Johansson, J. Leppaniemi, D. Mtsuko, Electronic Transport In Intermediate Sized Carbon Nanotubes. *Phys. Rev. B* **79**, 155408 (2009).

21. M. J. O'Connell, Carbon Nanotubes: Properties and Application, *CRC Press, London*, **22**, (2006).

22. A. E. Mostafa, W. A. Wassef, Transit Time In Base Region Of Drift Transistors Considering Diffusion, Recombination, And Variable Built-In Electric Field. *IEE Trans. Electron Device.* **17,** 53 (1970).

23. R. Lu, J. J. Shi, F. J. Baca, J. Z. Wu, High Performance Multiwall Carbon Nanotube Bolometers. *J. Appl. Phys.* **108**, 084305 (2010).

24. A. Gohier, A. Dhar, L. Gorintin, P. Bondavalli, Y. Bonnassieux and C. S. Cojocaru, All-Printed Infrared Sensor Based On Multiwalled Carbon Nanotubes. *Appl.Phys. Lett*. **98**, 063103 (2011).

25. B. K. Sarker, M. Arif, P. Stokes, S. I. Khondaker, Diffusion Mediated Photoconduction In Multiwalled Carbon Nanotube Films. *J.Appl. Phys.* **106**, 074307 (2009).

26. B. K. Sarker, M. Arif, S. I. Khondaker, Near-Infrared Photoresponse In Single-Walled Carbon Nanotube/Polymer Composite Films. *Carbon* **48**, 1539 (2010).

27. A. Serra, D. Manno, E. Filippo, A. Tepore, M. Letizia Terranova, S. Orlanducci and M. Rossi, Photoconductivity of Packed Homotype Bundles Formed by Aligned Single-Walled Carbon Nanotubes. *Nano Lett*. **8**, 968 (2008).

28. S. Ghosh, B. K. Sarker, A. Chunder, L. Zhai, S. I. Khondaker, Position dependent photodetector from large area reduced graphene oxide thin films. *Appl. Phys. Lett*. **96**, 163109 (2010).

29. P. Stokes, L. W. Liu, J. H. Zou, L. Zhai, Q. Huo and S. I. Khondaker, Photoresponse in large area multiwalled carbon nanotube/polymer nanocomposite films. *Appl. Phy. Lett.* **94**, (2009).

30. E. Kymakis, G. A. J. Amaratunga, Single-Wall Carbon Nanotube/Conjugated Polymer Photovoltaic Devices. *Appl.Phys.Lett.* **80**, 112 (2002).

31. Xu Z, Wu Y, and Hu B, Ivanov IN, Geohegan D B. Carbon Nanotube Effects On Electroluminescence And Photovoltaic Response In Conjugated Polymers. *Appl. Phys. Lett.* **87**, 263118 (2005)

32. Pradhan B, Batabyal SK, Pal AJ. Functionalized Carbon Nanotubes In Donor/Acceptor-Type Photovoltaic Devices. *Appl. Phys. Lett.* **88**, 093106 (2006)

CHAPTER 8: CONCLUSIONS

8.1 Summary

In this dissertation, we fabricated organic field effect transistors using aligned array carbon nanotube (CNT) electrodes, and investigated the charge injection and transport mechanisms of the fabricated devices. In addition, we also investigated the photoconduction mechanisms in the CNT and CNT/organic semiconductor nanocomposite thin film devices. The background of organic electronic devices, basic concept of charge injection in the organic field effect transistors, and summary of the previous work on carbon nanotube electrodes were discussed in chapter 1-2. The details of the fabrication of the organic field effect transistors with carbon nanotubes electrode as well metal electrodes, characterization of the process and experimental setup for electronic transport measurements were presented in chapter 3.

The room temperature electronic transport properties of the CNT contacted OFETs based various organic semiconductors such as pentacene, P3HT were discussed in chapter 4. All the OFETs fabricated with CNTs electrode have shown better performance than that of the OFETs with metal electrodes. Our short channel OFETs with CNT aligned array electrode showed a maximum mobility of 0.65 cm^2/Vs and a maximum on-off ratio of 1.7×10^6, which are higher than that of other reported short channel devices with metal electrode. In addition, the maximum cutoff frequency of our device is 211 MHz, which is the best reported so far for organic transistors. We also demonstrated fabrication of n-channel organic field effect transistors with aligned array carbon nanotube electrodes.

In chapter 5, the charge injection and transport mechanisms in the OFETs with aligned array were investigated by temperature dependent electronic transport measurements. We

showed that in the high temperature range (300 K-200 K), the charge injection mechanism is dominated by thermionic emission which is well explained by Richardson Schottky (RS) model. The calculated barrier height at CNT/pentacene interface (0.16 eV) is smaller than barrier height at metal/pentacene interfaces (0.35 eV). However, a transition from thermal emission to the tunneling mechanism is observed at temperature below 200 K. In addition, at low temperature the current-voltage characteristics show a transition from direct tunneling to Fowler-Nordheim tunneling, which further confirms a injection barrier at the CNT/pentacene interface. By analyzing thermally activated mobility and charge conduction mechanism, we showed that activation energy for pentacene device with CNT electrodes (~19 meV) is lower than the activation energy for the devices with metal electrodes (~ 41 meV). This confirms that the interfacial trap states at the CNT/pentacene interface are lower than that of at the metal/pentacene interface.

New device architecture for fabricating of high-performance OFET using the direct growth of crystalline nanowires on CNT electrodes was demonstrated in Chapter 6. We showed that compared to the organic nanowire OFETs with metal electrodes, the organic nanowires OFETs with CNT electrodes have shown consistently high mobility and high current on-off ratio with a maximum of 0.13 cm^2/Vs and 3.1×10^5, respectively. The improved device characteristics was attributed to the improved contact via strong π-π interaction CNT electrodes with the crystalline P3HT nanowires as well as the improved morphology of P3HT due to one dimensional crystalline structure.

In chapter 7, we investigated photoconduction mechanism of the CNTs and CNT/organic semiconductors composite thin films. Photoresponse of these films showed a position dependent with maximum photoresponse occurring at CNT/metal interface and is consistent with the model

of Schottky barrier modulation for photocurrent generation. We also showed that photoresponse of CNT/organic semiconductor thin film can be tuned by changing the weight percentage of CNT into the organic semiconductors.

8.2 Future Directions

The organic electronics is relative new and exciting area. It is my pleasure and honor to contribute in the area. In this thesis, we performed several experimental works to fabricate the high-performance electronic devices using aligned array carbon nanotubes and to understand the fundamental charge transport and injection mechanisms. More experimental and theoretical works are needed in realizing the overall goal of carbon nanotube electrodes in organic electronics devices. Based on our works presented here, we have few recommendations for future works in this direction.

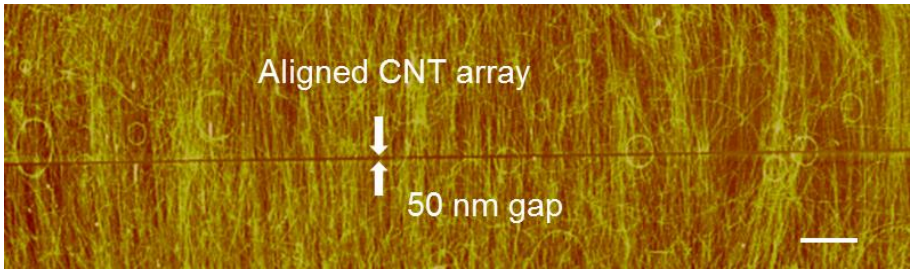

Figure 8.1: Atomic Force Microscopy image Aligned array carbon nanotube electrodes with high aspect ratio. This image is part of the whole electrode. Scale bar: 500 nm

First recommendation for the future work is to fabricate OFETs with high aspect ratio with very short channel length(less than 50 nm) CNT aligned array electrodes. We have some preliminary data on this project. Atomic force microscopy image of a high aspect ratio CNT aligned array electrode is shown in Figure 8.1. It is expected that the charge transport will be

enhanced in the OFETs with high aspect ratio CNT electrodes due to reduction of the grain boundaries of the organic semiconductor in the channel. These OFETs can be important tools to understand the physics of the charge transport and injection in the through the organic transistors

Our work can be extended to other conjugated polymers. For example, Poly(3,3’’’-didodecyl quarter thiophene) (PQT-12), a conjugated polymer with very similar molecular structure but different crystalline morphology in film state, was demonstrated to form similar centipede-like the structure with CNTs as P3HT. As shown in the TEM image (Figure 8.2), PQT-12 nanowires grow perpendicularly from the surface of SWNTs. Unlike P3HT, PQT-12 nanowires can have a much larger width (30-50 nm), offering the opportunity to investigate the influence of nanowire width on CNT electrode properties.

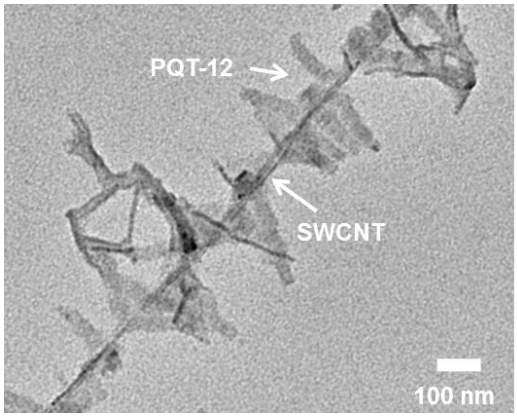

Figure 8.2: Transmission electron microscopy (TEM) images of perpendicular growth of PQT-12 nanowire on the surface of SWNTs.

We tested a few common organic semiconductors (pentacene, P3HT) in our study and we found the improved device performance with aligned array CNT electrodes. In order to fully understand the effectiveness of CNT electrode in the organic transistors, more organic semiconductors need to be tested. The fabrication and investigation of the OFETs with aligned

array CNT electrodes based on large number of organic semiconductors will be a significant contribution in this area. In addition, since the surface modification is increased the OFETs performance, it will be very interesting to investigate the effect of surface treatment in the devices with aligned array CNT electrodes.

In this work, we did not fabricate the OFETs with longer channel length (higher than 5 μm). This is because we were unable to assembly the CNTs in between the palladium pattern with larger channel length. It is well established that mobility of the OFETs is increased significantly with increasing channel length. As we shown that device performance is enhanced in the short channel OFET with aligned array CNT electrodes, it is expected that device performance can be further improved by using longer channel length CNT electrodes. Therefore, it will be also interesting to fabricate OFETs with longer channel length CNT aligned array electrodes. To fabricate of longer channel length CNT electrodes, CNT need to be aligned other than dielectrophoresis method such as chemical vapor deposition method.

In this dissertation, we have shown that charge injection, charge transport and the performance of the OFETs with aligned array CNT electrodes are improved. To better understand the charge injection and charge transport in the OFETs with aligned array CNT electrode, theoretical work are also required.

APPENDIX: COPYRIGHT PERMISSION AND PUBLICATIONS

COPYRIGHT PERMISSION

Copyright Clearance Center RightsLink®

Home | Account Info | Help

ACS Publications High quality High impact

Title: Thermionic Emission and Tunneling at Carbon Nanotube–Organic Semiconductor Interface

Logged in as: Biddut Sarker

LOGOUT

Author: Biddut K. Sarker and Saiful I. Khondaker

Publication: ACS Nano

Publisher: American Chemical Society

Date: Jun 1, 2012

Copyright © 2012, American Chemical Society

PERMISSION/LICENSE IS GRANTED FOR YOUR ORDER AT NO CHARGE

This type of permission/license, instead of the standard Terms & Conditions, is sent to you because no fee is being charged for your order. Please note the following:

- Permission is granted for your request in both print and electronic formats, and translations.
- If figures and/or tables were requested, they may be adapted or used in part.
- Please print this page for your records and send a copy of it to your publisher/graduate school.
- Appropriate credit for the requested material should be given as follows: "Reprinted (adapted) with permission from (COMPLETE REFERENCE CITATION). Copyright (YEAR) American Chemical Society." Insert appropriate information in place of the capitalized words.
- One-time permission is granted only for the use specified in your request. No additional uses are granted (such as derivative works or other editions). For any other uses, please submit a new request.

BACK | CLOSE WINDOW

RightsLink®

Home | Account Info | Help

Title: Fabrication of Organic Field Effect Transistor by Directly Grown Poly(3 Hexylthiophene) Crystalline Nanowires on Carbon Nanotube Aligned Array Electrode

Author: Biddut K. Sarker, Jianhua Liu, Lei Zhai, and Saiful I. Khondaker

Publication: Applied Materials

Publisher: American Chemical Society

Date: Apr 1, 2011

Logged in as:
Biddut Sarker

LOGOUT

PERMISSION/LICENSE IS GRANTED FOR YOUR ORDER AT NO CHARGE

This type of permission/license, instead of the standard Terms & Conditions, is sent to you because no fee is being charged for your order. Please note the following:

- Permission is granted for your request in both print and electronic formats, and translations.
- If figures and/or tables were requested, they may be adapted or used in part.
- Please print this page for your records and send a copy of it to your publisher/graduate school.
- Appropriate credit for the requested material should be given as follows: "Reprinted (adapted) with permission from (COMPLETE REFERENCE CITATION). Copyright (YEAR) American Chemical Society." Insert appropriate information in place of the capitalized words.
- One-time permission is granted only for the use specified in your request. No additional uses are granted (such as derivative works or other editions). For any other uses, please submit a new request.

BACK | CLOSE WINDOW

AMERICAN INSTITUTE OF PHYSICS LICENSE TERMS AND CONDITIONS

Oct 01, 2012

All payments must be made in full to CCC. For payment instructions, please see information listed at the bottom of this form.

License Number	3000380058152
Order Date	Oct 01, 2012
Publisher	American Institute of Physics
Publication	Applied Physics Letters
Article Title	High-performance short channel organic transistors using densely aligned carbon nanotube array electrodes
Author	Biddut K. Sarker, Saiful I. Khondaker
Online Publication Date	Jan 9, 2012
Volume number	100
Issue number	2
Type of Use	Thesis/Dissertation
Requestor type	Author (original article)
Format	Print and electronic
Portion	Figure/Table
Number of figures/tables	3
Title of your thesis / dissertation	Electronic and Optoelectronic Transport Properties of Carbon Nanotube/Organic Semiconductor Devices
Expected completion date	Dec 2012
Estimated size (number of pages)	170
Total	0.00 USD

Terms and Conditions

American Institute of Physics -- Terms and Conditions: Permissions Uses

American Institute of Physics ("AIP") hereby grants to you the non-exclusive right and license to use and/or distribute the Material according to the use specified in your order, on a one-time basis, for the specified term, with a maximum distribution equal to the number that you have ordered. Any links or other content accompanying the Material are not the subject of this license.

1. You agree to include the following copyright and permission notice with the reproduction of the Material: "Reprinted with permission from [FULL CITATION]. Copyright [PUBLICATION YEAR], American Institute of Physics." For an article, the copyright and permission notice must be printed on the first page of the article or book chapter. For photographs, covers, or tables, the copyright and permission notice may appear with the Material, in a footnote, or in the reference list.
2. If you have licensed reuse of a figure, photograph, cover, or table, it is your responsibility to ensure that the material is original to AIP and does not contain the copyright of another entity, and that the copyright notice of the figure, photograph, cover, or table does not indicate that it was reprinted by AIP, with permission, from another source. Under no circumstances does AIP, purport or intend to grant permission to reuse material to which it

ELSEVIER LICENSE
TERMS AND CONDITIONS

Oct 01, 2012

This is a License Agreement between Biddut K Sarker ("You") and Elsevier ("Elsevier") provided by Copyright Clearance Center ("CCC"). The license consists of your order details, the terms and conditions provided by Elsevier, and the payment terms and conditions.

All payments must be made in full to CCC. For payment instructions, please see information listed at the bottom of this form.

Supplier	Elsevier Limited The Boulevard,Langford Lane Kidlington,Oxford,OX5 1GB,UK
Registered Company Number	1982084
Customer name	Biddut K Sarker
Customer address	3408 Lariat Lane, Apt 25 Oralndo, FL 32826
License number	3000370802674
License date	Oct 01, 2012
Licensed content publisher	Elsevier
Licensed content publication	Carbon
Licensed content title	Near-infrared photoresponse in single-walled carbon nanotube/polymer composite films
Licensed content author	Biddut K. Sarker,M. Arif,Saiful I. Khondaker
Licensed content date	April 2010
Licensed content volume number	48
Licensed content issue number	5
Number of pages	6
Start Page	1539
End Page	1544
Type of Use	reuse in a thesis/dissertation
Portion	full article
Format	both print and electronic
Are you the author of this Elsevier article?	Yes
Will you be translating?	No
Order reference number	

AMERICAN INSTITUTE OF PHYSICS LICENSE TERMS AND CONDITIONS

Oct 01, 2012

All payments must be made in full to CCC. For payment instructions, please see information listed at the bottom of this form.

License Number	3000380438086
Order Date	Oct 01, 2012
Publisher	American Institute of Physics
Publication	Journal of Applied Physics
Article Title	Diffusion mediated photoconduction in multiwalled carbon nanotube films
Author	Biddut K. Sarker, M. Arif, Paul Stokes, Saiful I. Khondaker et al.
Online Publication Date	Oct 13, 2009
Volume number	106
Issue number	7
Type of Use	Thesis/Dissertation
Requestor type	Author (original article)
Format	Print and electronic
Portion	Figure/Table
Number of figures/tables	5
Title of your thesis / dissertation	Electronic and Optoelectronic Transport Properties of Carbon Nanotube/Organic Semiconductor Devices
Expected completion date	Dec 2012
Estimated size (number of pages)	170
Total	0.00 USD

Terms and Conditions

American Institute of Physics -- Terms and Conditions: Permissions Uses

American Institute of Physics ("AIP") hereby grants to you the non-exclusive right and license to use and/or distribute the Material according to the use specified in your order, on a one-time basis, for the specified term, with a maximum distribution equal to the number that you have ordered. Any links or other content accompanying the Material are not the subject of this license.

1. You agree to include the following copyright and permission notice with the reproduction of the Material: "Reprinted with permission from [FULL CITATION]. Copyright [PUBLICATION YEAR], American Institute of Physics." For an article, the copyright and permission notice must be printed on the first page of the article or book chapter. For photographs, covers, or tables, the copyright and permission notice may appear with the Material, in a footnote, or in the reference list.
2. If you have licensed reuse of a figure, photograph, cover, or table, it is your responsibility to ensure that the material is original to AIP and does not contain the copyright of another entity, and that the copyright notice of the figure, photograph, cover, or table does not indicate that it was reprinted by AIP, with permission, from another source. Under no circumstances does AIP, purport or intend to grant permission to reuse material to which it

NATURE PUBLISHING GROUP LICENSE
TERMS AND CONDITIONS

Nov 11, 2012

This is a License Agreement between Biddut K Sarker ("You") and Nature Publishing Group ("Nature Publishing Group") provided by Copyright Clearance Center ("CCC"). The license consists of your order details, the terms and conditions provided by Nature Publishing Group, and the payment terms and conditions.

All payments must be made in full to CCC. For payment instructions, please see information listed at the bottom of this form.

License Number	3026010977046
License date	Nov 11, 2012
Licensed content publisher	Nature Publishing Group
Licensed content publication	Nature
Licensed content title	The path to ubiquitous and low-cost organic electronic appliances on plastic
Licensed content author	Stephen R. Forrest
Licensed content date	Apr 29, 2004
Volume number	428
Issue number	6986
Type of Use	reuse in a thesis/dissertation
Requestor type	academic/educational
Format	print and electronic
Portion	figures/tables/illustrations
Number of figures/tables/illustrations	2
High-res required	no
Figures	Figure 3
Author of this NPG article	no
Your reference number	
Title of your thesis / dissertation	Electronic and Optoelectronic Transport Properties of Carbon Nanotube/Organic Semiconductor Devices
Expected completion date	Dec 2012

ELSEVIER LICENSE
TERMS AND CONDITIONS

Nov 11, 2012

This is a License Agreement between Biddut K Sarker ("You") and Elsevier ("Elsevier") provided by Copyright Clearance Center ("CCC"). The license consists of your order details, the terms and conditions provided by Elsevier, and the payment terms and conditions.

All payments must be made in full to CCC. For payment instructions, please see information listed at the bottom of this form.

Supplier	Elsevier Limited The Boulevard,Langford Lane Kidlington,Oxford,OX5 1GB,UK
Registered Company Number	1982084
Customer name	Biddut K Sarker
Customer address	3408 Lariat Lane, Apt 25 Orlando, FL 32826
License number	3026010278569
License date	Nov 11, 2012
Licensed content publisher	Elsevier
Licensed content publication	Materials Today
Licensed content title	Organic and polymer transistors for electronics
Licensed content author	Ananth Dodabalapur
Licensed content date	April 2006
Licensed content volume number	9
Licensed content issue number	4
Number of pages	7
Start Page	24
End Page	30
Type of Use	reuse in a thesis/dissertation
Intended publisher of new work	other
Portion	figures/tables/illustrations
Number of figures/tables/illustrations	2
Format	both print and electronic

RightsLink®

Home | Account Info | Help

Title: Electron and Ambipolar Transport in Organic Field-Effect Transistors

Author: Jana Zaumseil and and Henning Sirringhaus*

Publication: Chemical Reviews

Publisher: American Chemical Society

Date: Apr 1, 2007

Logged in as: Biddut Sarker

LOGOUT

PERMISSION/LICENSE IS GRANTED FOR YOUR ORDER AT NO CHARGE

This type of permission/license, instead of the standard Terms & Conditions, is sent to you because no fee is being charged for your order. Please note the following:

- Permission is granted for your request in both print and electronic formats, and translations.
- If figures and/or tables were requested, they may be adapted or used in part.
- Please print this page for your records and send a copy of it to your publisher/graduate school.
- Appropriate credit for the requested material should be given as follows: "Reprinted (adapted) with permission from (COMPLETE REFERENCE CITATION). Copyright (YEAR) American Chemical Society." Insert appropriate information in place of the capitalized words.
- One-time permission is granted only for the use specified in your request. No additional uses are granted (such as derivative works or other editions). For any other uses, please submit a new request.

If credit is given to another source for the material you requested, permission must be obtained from that source.

JOHN WILEY AND SONS LICENSE TERMS AND CONDITIONS

Oct 01, 2012

This is a License Agreement between Biddut K Sarker ("You") and John Wiley and Sons ("John Wiley and Sons") provided by Copyright Clearance Center ("CCC"). The license consists of your order details, the terms and conditions provided by John Wiley and Sons, and the payment terms and conditions.

All payments must be made in full to CCC. For payment instructions, please see information listed at the bottom of this form.

License Number	3000390858272
License date	Oct 01, 2012
Licensed content publisher	John Wiley and Sons
Licensed content publication	Advanced Materials
Book title	
Licensed content author	Marko Marinkovic,Dagmawi Belaineh,Veit Wagner,Dietmar Knipp
Licensed content date	Jun 22, 2012
Start page	4005
End page	4009
Type of use	Dissertation/Thesis
Requestor type	University/Academic
Format	Print and electronic
Portion	Figure/table
Number of figures/tables	1
Number of extracts	
Original Wiley figure/table number(s)	2
Will you be translating?	No
Order reference number	
Total	0.00 USD
Terms and Conditions	

JOHN WILEY AND SONS LICENSE
TERMS AND CONDITIONS

Nov 09, 2012

This is a License Agreement between Biddut K Sarker ("You") and John Wiley and Sons ("John Wiley and Sons") provided by Copyright Clearance Center ("CCC"). The license consists of your order details, the terms and conditions provided by John Wiley and Sons, and the payment terms and conditions.

All payments must be made in full to CCC. For payment instructions, please see information listed at the bottom of this form.

License Number	3024821166263
License date	Nov 09, 2012
Licensed content publisher	John Wiley and Sons
Licensed content publication	Macromolecular Rapid Communications
Book title	
Licensed content author	Jianhua Liu,Jianhua Zou,Lei Zhai
Licensed content date	Aug 12, 2009
Start page	n/a
End page	n/a
Type of use	Dissertation/Thesis
Requestor type	University/Academic
Format	Print and electronic
Portion	Figure/table
Number of figures/tables	2
Number of extracts	
Original Wiley figure/table number(s)	Cover Figure
Will you be translating?	No
Order reference number	
Total	0.00 USD
Terms and Conditions	

NATURE PUBLISHING GROUP LICENSE
TERMS AND CONDITIONS

Nov 11, 2012

This is a License Agreement between Biddut K Sarker ("You") and Nature Publishing Group ("Nature Publishing Group") provided by Copyright Clearance Center ("CCC"). The license consists of your order details, the terms and conditions provided by Nature Publishing Group, and the payment terms and conditions.

All payments must be made in full to CCC. For payment instructions, please see information listed at the bottom of this form.

License Number	3026270174239
License date	Nov 11, 2012
Licensed content publisher	Nature Publishing Group
Licensed content publication	Nature Nanotechnology
Licensed content title	Progress towards monodisperse single-walled carbon nanotubes
Licensed content author	Mark C. Hersam
Licensed content date	Jul 1, 2008
Volume number	3
Issue number	7
Type of Use	reuse in a thesis/dissertation
Requestor type	academic/educational
Format	print and electronic
Portion	figures/tables/illustrations
Number of figures/tables/illustrations	2
High-res required	no
Figures	Figure 2
Author of this NPG article	no
Your reference number	
Title of your thesis / dissertation	Electronic and Optoelectronic Transport Properties of Carbon Nanotube/Organic Semiconductor Devices
Expected completion date	Dec 2012
Estimated size (number of pages)	170
Total	0.00 USD

AMERICAN INSTITUTE OF PHYSICS LICENSE TERMS AND CONDITIONS

Nov 08, 2012

All payments must be made in full to CCC. For payment instructions, please see information listed at the bottom of this form.

License Number	3024570246575
Order Date	Nov 08, 2012
Publisher	American Institute of Physics
Publication	Applied Physics Letters
Article Title	Poly(3,3‴-didodecylquarterthiophene) field effect transistors with single-walled carbon nanotube based source and drain electrodes
Author	Yuan Yuan Zhang, Yumeng Shi, Fuming Chen, S. G. Mhaisalkar, et al.
Online Publication Date	Nov 30, 2007
Volume number	91
Issue number	22
Type of Use	Thesis/Dissertation
Requestor type	University or Educational Institution
Format	Print and electronic
Portion	Figure/Table
Number of figures/tables	3
Title of your thesis / dissertation	Electronic and Optoelectronic Transport Properties of Carbon Nanotube/Organic Semiconductor Devices
Expected completion date	Dec 2012
Estimated size (number of pages)	170
Total	0.00 USD
Terms and Conditions	

American Institute of Physics -- Terms and Conditions: Permissions Uses

American Institute of Physics ("AIP") hereby grants to you the non-exclusive right and license to use and/or distribute the Material according to the use specified in your order, on a one-

JOHN WILEY AND SONS LICENSE TERMS AND CONDITIONS

Nov 08, 2012

This is a License Agreement between Biddut K Sarker ("You") and John Wiley and Sons ("John Wiley and Sons") provided by Copyright Clearance Center ("CCC"). The license consists of your order details, the terms and conditions provided by John Wiley and Sons, and the payment terms and conditions.

All payments must be made in full to CCC. For payment instructions, please see information listed at the bottom of this form.

License Number	3024571147149
License date	Nov 08, 2012
Licensed content publisher	John Wiley and Sons
Licensed content publication	Advanced Materials
Book title	
Licensed content author	Sondra L. Hellstrom,Run Zhi Jin,Randall M. Stoltenberg,Zhenan Bao
Licensed content date	Jul 12, 2010
Start page	4204
End page	4208
Type of use	Dissertation/Thesis
Requestor type	University/Academic
Format	Print and electronic
Portion	Figure/table
Number of figures/tables	3
Number of extracts	
Original Wiley figure/table number(s)	Figure 2 and 3
Will you be translating?	No
Order reference number	
Total	0,00 USD

REFEREED PUBLICATIONS ARISING FROM THIS DISSERTATION

1. **Biddut K. Sarker** and Saiful I. Khondaker. Improved Charge Transport in Organic Transistors with Carbon Nanotube Electrodes. *In Preparation* (2012)

2. **Biddut K. Sarker**, and Saiful I. Khondaker. Thermionic Emission and Tunneling at Carbon Nanotube-Organic Semiconductor Interface. *ACS Nano, 6, 4993 (2012)*

3. **Biddut K. Sarker**, and Saiful I. Khondaker. High Performance Short Channel Organic Transistors using Densely Aligned Carbon Nanotube Array Electrodes. *Appl. Phys. Lett. 100, 023301 (2012)*

4. **Biddut K. Sarker**, Jianhua Liu, Lei Zhai, and Saiful I. Khondaker. Fabrication of Organic Field Effect Transistor by Directly Grown Poly(3 Hexylthiophene) Crystalline Nanowires on Carbon Nanotube Aligned Array Electrode. *ACS Appl. Mater. Interfaces, 3, 1180 (2011)*

5. **Biddut K. Sarker**, Muhammad R. Islam, Feras Alzubi, and Saiful I. Khondaker. Fabrication of Aligned Carbon Nanotube Array Electrodes for Organic Electronics Devices. *Mater. Express, 1,80 (2011)*

6. **Biddut K. Sarker**, M. Arif, and Saiful I. Khondaker. Near-Infrared Photoresponse in Single Walled Carbon Nanotube/Polymer Composite Films. *Carbon, 48, 1539 (2009)*

7. **Biddut K. Sarker**, M. Arif, Paul Stokes and Saiful I. Khondaker. Diffusion Mediated Photoconduction in Multi-Walled Carbon Nanotube Films*". J. Appl. Phys. 106, 074307(2009)*